Interpretation of Lunar Topography: Impact Cratering and Surface Roughness

Thesis by

Margaret A. Rosenburg

In Partial Fulfillment of the Requirements

for the Degree of

Doctor of Philosophy

California Institute of Technology

Pasadena, California

2014

(Defended May 23, 2014)

The impact theory applies a single process to the entire series,correlating size variation with form variation in a rational way... In fine, it unites and organizes as a rational and coherent whole the varied strange appearances whose assemblage on our neighbor's face cannot have been fortuitous.

—G. K. Gilbert, 1893

She died early, but thus saved upon herself the marks of youth. She is not an aged, decrepit world, since the dead do not age; she is an embalmed mummy, and by her outer appearance we can judge the appearance of other worlds at the beginning of Creation.

—E. J. Öpik, 1916

The origin of the principal morphological features on the lunar surface—the circular or subcircular craters ranging from centimeters to hundreds of kilometers in diameter—remains a controversial subject. On the one hand the countless number of craters attests to an intense bombardment of the moon by interplanetary debris over eons of time. But on the other hand there is ample evidence for extensive volcanic activity that many workers argue has been active either directly or indirectly as a major crater-forming process. Undoubtedly, both exogenic and endogenic processes have been in action and the controversy now revolves around the relative significance of the two agents for crater formation.

—D. E. Gault, 1970

Acknowledgements

I have been extraordinarily lucky during my time at Caltech to have had friends and mentors who support my broad range of interests and who have, at times relentlessly, insisted that I see them through. The last seven years have been a time of great professional and personal growth for me, as a scientist, an aspiring historian of science, and a communicator, and for that I have a great many people to acknowledge.

First, my advisor in GPS, Oded Aharonson, has been an excellent mentor to me and unfailing in his support, both of my work in planetary science and of my interest in the history of science. He has often gone out of his way to check in with me, never hesitating to let me know when I've met or even exceeded expectations, and I can't thank him enough for providing that occasional boost of confidence. Over the years we have developed a frank conversation style that I think has served us well, both in person and separated by many time zones. I am happy to count him as a friend as well as an an advisor, and delighted to have found a kindred spirit when it comes to proper grammar.

I have been very fortunate to work with Re'em Sari on many pieces of this dissertation. His clarity of vision and talent for getting to the heart of the matter at hand are both impressive and inspiring, and I have learned a great deal from the time I've spent working with him.

The grad students in Oded's group that have gone before me, Troy Hudson, Kevin Lewis, Margarita Marinova, and Alex Hayes, have provided invaluable advice along the way, both before and after their own respective thesis defenses. Thank you also to Aaron Wolf, Steve Chemtob, Michelle Selvans, Melanie Channon, Gretchen Keppel-Aleks, Sonja Graves, Colette Salyk, Dan Bower, June Wicks, Xi Zhang, Zane Selvans, and many other intelligent and talented GPS grad students who have helped me, both in and out of the office. In many ways, I judge the measure of my success in planetary science by the standards they have set, and I've never had far to look to find the best role models anyone could ask for.

I am indebted to Moti Feingold in HPS for helping me to take my fledgling interest in the history of science and turn it into a project I can truly be proud of. Bridging disciplines is not easy, and he has been unwavering in patience and encouragement. It has sometimes been difficult to balance the time spent on each aspect of my academic work, and Moti has always provided a clear head, a positive outlook, and wealth of knowledge to keep me on the right path. I can't thank him enough.

Likewise, I have to thank the members of my thesis committee, David Stevenson, Andy Ingersoll, and Mike Gurnis, for their help and support. The administrators in the GPS office, especially Irma Black, Margaret Carlos, and Nora Oshima, have been very helpful to me over the years. I also thank Felicia Hunt, Natalie Gilmore, and Joe Shepherd in the Graduate Office, as well as Mary Morley and Tess Legaspi in the Registrar's Office, for helping me find the best path forward to achieve my goals at Caltech.

It may sound strange to credit an extracurricular activity with anything so weighty as character development, but I owe much of the personal growth I've experienced over the past few years to my participation in Caltech theater: TACIT, EXPLiCIT, and Caltech Playreaders. A play is a funny thing. It takes an incredible amount of effort by a great many people to put together a production, and, start to finish, it only lasts a few weeks before it's over. But it's the opportunity to create something from nothing in such a short time, the pulling together of everyone involved—and at Caltech, that means every person has a lab to return to, a problem set to finish, or a spacecraft to monitor—that makes it worthwhile. Brian Brophy has been a tireless advocate for theater on campus, and Caltech is lucky to have him. Kathryn Bikle has generously allowed me to assist her in directing two summer Shakespeare plays, and I have learned so much from her example. David and Ella Seal, Todd Brun, Cara King, Kim Becker, Ann Lindsey, Teagan Wall, Kim Boddy, Ben Sveinbjornsson, Doug Smith, Sarah Slotznick, Ben Solish, Holly Bender, Miranda Stewart, Ashley Stroupe, Kari Hodge, Amit Lakhanpal—you all have made such a tremendous difference in my life.

I also have Caltech theater to thank for landing me the amazing opportunity to produce *The PHD*

Movie with Jorge Cham, a lucky break in many ways that has opened my eyes to the possibilities of science communication. I was incredibly shy as a child, and I still cannot quite believe that I see a role for myself as a communicator, but working with Jorge has taught me to keep creating, to accept and learn from feedback, and to trust my instincts. I am so grateful for everything I've learned from Jorge and from everyone else involved in the movie and PHD TV, including (but not limited to) Laurence Yeung, Crystal Dilworth, Alex Lockwood, Matt Siegler, Roser Segura Flor, Vahe Gabuchian, Zachary Abbott, and Zach Tobin. Thank you!

I credit my parents with inspiring and fostering my love of learning, and I am grateful to them and to my sisters, Sharon and Amanda, for all of the support they've provided throughout my time in graduate school. I am blessed to have gained another set of parents almost four years ago, and I thank them for welcoming me into their family. When I first moved to Pasadena, it was comforting to know that my Aunt Judith and Uncle Brad would be so close, and that my grandparents would be there as well for many months out of the year. I have greatly enjoyed getting to know them and my cousins, Zach and Jackson, and I am incredibly proud that Grandad will be at my defense. I wish that Nonny could have been here too, and I dedicate this thesis to her. She taught me the importance of living life to the fullest, starting new adventures, and finding happiness in the relationships we build with others.

Above all, I thank my husband, Jonathan Wolfe, without whom none of this could have happened. He is the real deal: a true partner, an honest critic, and a good friend. Thanks to him (and to our schnauzer, Simon, of course!), Pasadena has become my home.

The MIT Shakespeare Ensemble has a tradition of reciting a quote from *A Midsummer Night's Dream* just before the curtain goes up, and I think it's only fitting that I continue that tradition now, so here goes: "Take pains, be perfect. Adieu!"

Abstract

This work seeks to understand past and present surface conditions on the Moon using two different but complementary approaches: topographic analysis using high-resolution elevation data from recent spacecraft missions and forward modeling of the dominant agent of lunar surface modification, impact cratering. The first investigation focuses on global surface roughness of the Moon, using a variety of statistical parameters to explore slopes at different scales and their relation to competing geological processes. We find that highlands topography behaves as a nearly self-similar fractal system on scales of order 100 meters, and there is a distinct change in this behavior above and below approximately 1 km. Chapter 2 focuses this analysis on two localized regions: the lunar south pole, including Shackleton crater, and the large mare-filled basins on the nearside of the Moon. In particular, we find that differential slope, a statistical measure of roughness related to the curvature of a topographic profile, is extremely useful in distinguishing between geologic units. Chapter 3 introduces a numerical model that simulates a cratered terrain by emplacing features of characteristic shape geometrically, allowing for tracking of both the topography and surviving rim fragments over time. The power spectral density of cratered terrains is estimated numerically from model results and benchmarked against a 1-dimensional analytic model. The power spectral slope, β, is observed to vary predictably with the size-frequency distribution of craters, as well as the crater shape. The final chapter employs the rim-tracking feature of the cratered terrain model to analyze the evolving size-frequency distribution of craters under different criteria for identifying "visible" craters from surviving rim fragments. A geometric bias exists that systematically over counts large or small craters, depending on the rim fraction required to count a given feature as either visible or erased.

Contents

List of Figures

List of Tables

List of Acronyms

HPF Hartmann Production Function

LOLA Lunar Orbiter Laser Altimeter

LRO Lunar Reconnaissance Orbiter

LROC Lunar Reconnaissance Orbiter Camera

MESSENGER MErcury Surface, Space ENvironment, GEochemistry, and Ranging

MLA Mercury Laser Altimeter

MOLA Mars Orbiter Laser Altimeter

NAC Narrow Angle Camera

NLR NEAR Laser Rangefinder

PSD Power Spectral Density

PSR Permanently Shadowed Region

SLA Shuttle Laser Altimeter

USGS United States Geological Survey

WAC Wide Angle Camera

Chapter 1

Introduction

1.1 The Lunar Topography

The surface of the Moon has been the subject of telescopic investigations for hundreds of years, ever since the earliest instruments were first turned to the night sky (*Whitaker*, 2003), and long before the word "science" came into popular use (*Lindberg*, 1992). Our natural satellite is also the most visited planetary body by spacecraft, aside from the Earth itself, and the only destination (so far) to have been reached by human explorers. The Moon thus occupies a special place in the public imagination, and the shape and properties of its surface in particular have played a significant role in several major scientific debates of the last few decades, including the origin of the Earth-Moon system, the history of life and mass extinctions on our own planet, and the evolution of planetary surfaces throughout the solar system. In 1610, when Galileo first described the pattern of light and shadow he saw through his telescope as the interaction of sunlight with a rugged, three-dimensional terrain (*Galilei*, 1989), he began what has become a long tradition of seeking to decipher the "cuneiform writings" (*Fauth*, 1909) encoded in the lunar surface—that is, to interpret its physical features.

The topography of a planetary body contains the remnants of the geologic, geomorphologic, and cosmic processes that have contributed to its formation and subsequent modification. On the Moon, impact cratering is the dominant agent of surface modification (*Melosh*, 1989), although evidence of other processes, including vast volcanic plains and tectonic features like extensional graben and wrinkle ridges, is also abundant (*Wilhelms et al.*, 1987). Compared to the Earth, with its plate tectonics, atmosphere, and hydrologic cycle, the Moon thus presents a somewhat simplified setting in which to study the most ubiquitous process in the solar system, the collision of bolides with planetary surfaces and the formation of impact craters. Moreover, the lunar surface contains a record of times long past, the corresponding terrestrial record of which has been almost completely erased. The second quote in the dedication of this thesis was written by Ernst J. Öpik in his 1916 paper exploring the possibility that the lunar craters were formed by impact, rather than volcanic, processes. While he concludes that an impact origin is unlikely given the absence of similar features on Earth, he makes an eloquent observation that, to a great extent, describes our current approach toward lunar impact crater studies: the lunar surface is telling of conditions in the past, and that information can be used to interpret cratered terrains throughout the solar system.

This thesis focuses on two parallel approaches to understanding the lunar topography: on the one hand, we employ high-resolution elevation data from recent spacecraft missions to analyze the statistical properties of surface roughness, while on the other, we develop a cratered-terrain model to investigate the expected statistical signatures produced by the process of impact cratering. In developing and comparing these two approaches, our goal is to determine the extent to which the topographical markers of competing geomorphological processes can be disentangled for the Moon, with the hope that improving our understanding of the cratering record on our own satellite will provide a useful resource for other planetary surfaces.

1.1.1 Interpreting Cratered Terrains

Craters were among the first lunar features to be described by early observers, although the word "crater" was only applied to them in the late-18th century, first by Johann Schröter, who borrowed the term from volcanology. This conflation of terms was not accidental, as Schröter, along with most of his contemporaries, believed the lunar craters to be of volcanic origin, based on analogy with terrestrial features. Various versions of the impact theory for the origin of lunar craters were also proposed, but they found little support until the early 20th century, when, fueled by new wartime experiences with aerial reconnaissance and bomb craters, the explosive nature of the impact process began to be explored (*Ives*, 1919; *Gifford*, 1924; *Wegener and Şengör*, 1975). In the decades leading up to the First World War, the debate over lunar craters was fought on two fronts, as both the reliability of terrestrial analogy as a means of interpreting extraterrestrial features and the utility of laboratory-scale impact experiments were contested. The explosion hypothesis provided an explanation for the near-perfect circularity of lunar craters, a common stumbling block for the impact hypothesis because oblique impact angles were known to be more likely than vertical ones (*Gilbert*, 1893) and small-scale experiments commonly resulted in elliptical craters. At the same time, the identification of terrestrial impact craters, especially Meteor Crater in Arizona, led to a broader understanding of the Earth's own impact history (*Hoyt*, 1987). Further developments in the 1940s by *Dietz* (1946), who studied changes in physiographic form with increasing crater diameter, and by *Baldwin* (1949), who connected the depth-diameter scaling for impact craters and chemical explosion craters, established a quantitative relationship between impact energy and crater morphometry (*Doel*, 1996). Detailed studies of nuclear test craters and Meteor Crater led Eugene M. Shoemaker to spearhead the founding of the Astrogeology branch of the United States Geological Survey (USGS) and to initiate the first geologic maps of the Moon (*Shoemaker*, 1963, 1977; *Shoemaker and Hackman*, 1962; *Wilhelms*, 1993).

The recognition that stratigraphic relationships between geologic units of different ages can be determined by close examination of the lunar surface forms the basis of our present understanding of the Moon's surface history. Five major periods, primarily defined by the formation of major basins and the emplacement of mare basalts, are distinguished, the boundaries of which are calibrated by absolute ages from lunar samples: Copernican ($\sim$ 1.1 Gya-present), Eratosthenian ($\sim 3.2 - 1.1$ Gya), Imbrian ($\sim 3.85 - 3.2$ Gya), Nectarian ($\sim 3.9 - 3.85$ Gya), and Pre-Nectarian ($\sim 4.5 - 3.9$ Gya) (*Wilhelms et al.*, 1987; *Stöffler and Ryder*, 2001).

The comparison of crater densities on different surfaces provides a system of relative ages that can be referenced to the absolute ages from radiometric dating of returned samples and lunar meteorites (*Hartmann*, 1970; *Neukum et al.*, 1975; *Strom*, 1977). Statistical treatments of the size-frequency distribution of lunar craters were first derived from telescopic observations of the near side of the

Moon (*MacDonald*, 1931; *Young*, 1940; *Öpik*, 1960; *Baldwin*, 1964), and more detailed studies became feasible in the mid-1960s with the return of photographs from successful lunar probes in the Ranger and Surveyor programs (*Brinkmann*, 1966; *Jaffe*, 1967). Since that time, the interpretation of cratered terrains from a statistical standpoint has developed into a fruitful subfield with its own terminology, conventions, and literature (*Melosh*, 1989), and it now encompasses the study of planetary surfaces across the solar system (*Passey and Shoemaker*, 1982; *Zahnle et al.*, 2003; *Pike*, 1988; *Neukum and Ivanov*, 1994). Detailed examinations of cratered surfaces establish a geologic timescale correlated across planetary bodies (*Shoemaker et al.*, 1961), to determine the populations of impactors responsible for forming them (*Ivanov et al.*, 2002), and to thus provide constraints on dynamical models of solar system formation (*Bottke Jr et al.*, 2005).

1.1.2 Surface Roughness

The term "surface roughness" has generally been used since the 19th century to convey the degree to which an interface—whether it be the outer surface of a rock outcrop (*Shaler and Davis*, 1881), a metal tool (*Nasmyth and Carpenter*, 1874), or bone (*Adams*, 1874)—departs from a perfectly smooth surface. The development of aerial photography and radar in the early 20th century marked the origins of remote sensing as it is practiced today (*Campbell*, 2002), and led to new ways of quantifying the surface roughness of natural terrains and relating these measures to surface processes. In the 1970s, range-Doppler and radar techniques for quantifying surface roughness on planetary bodies came into their own, and techniques were developed to integrate ground-based and spacecraft observations (*Butrica*, 1996; *Ostro*, 1993). By the time laser altimetry was developed for Apollo 15 to measure topographic profiles from orbit (*Kaula et al.*, 1974), multiple kinds of elevation data were available for the Moon.

Today, surface roughness is still defined in a variety of ways, depending on the dataset used, the surface being investigated, and the purpose of the study (*Shepard et al.*, 2001; *Kreslavsky et al.*, 2013). Nevertheless, the quantification of roughness properties has proven highly useful in discriminating among geologic units and understanding the complex interaction between surface processes acting at different scales. On Mars, for example, *Kreslavsky and Head* (2000) found a systematic variation in the Hurst exponent (a unit of measure that captures the scale dependence of slopes, described in Chapter 2) with latitude that has been associated with the presence of subsurface ice. *Aharonson et al.* (1998) and *Aharonson et al.* (2001) found the extreme smoothness of sedimented basins on Mars, especially Amazonis Planitia, to be most analogous to heavily sedimented fluvial basins on Earth, such as the ocean floor. Power spectra of topography were used by *Nimmo et al.* (2011) to study the lithospheres of icy satellites, and *Zuber et al.* (2000) considered surface slopes on asteroid 433 Eros to classify it as a rubble pile. On the Moon, *Rosenburg et al.* (2011) and *Kreslavsky et al.* (2013) found significantly different behavior in roughness properties above and below approximately kilometer scales, with important implications for competing surface processes such as the the emplacement of craters, the generation of lunar regolith through impact gardening, and seismic shaking in the vicinity of large impacts.

1.1.3 Planetary Surface Topography from Laser Altimetry

For planetary applications, laser altimetry relies on the accurate detection and timing of laser pulses reflected from a planetary surface, as well as accurate tracking of spacecraft position from Earth. Thus, orbit determination is the main source of error in the resulting measurements, which are based on the travel time of the emitted and reflected pulses (*Neumann*, 2001). The vertical precision with which each measurement within an orbit track can be made provides a separate, generally smaller, source of error, and the frequency of laser pulses determines the along-track spacing of the elevation measurements (*Smith et al.*, 2010a).

Table 1.1 contains a summary of performance parameters for selected laser altimeters carried on planetary missions. The first instruments were designed for Apollo 15, 16, and 17, and they measured the height of the command and service module at intervals of 30 to 43 km (*Kaula et al.*, 1974). From February through May of 1994, the Clementine orbiter mapped the topography of the Moon (*Smith et al.*, 1997; *Zuber et al.*, 1994), while the Shuttle Laser Altimeter 1 and 2 (SLA-01 and SLA-02) measured the Earth's topography on STS-72 and STS-85, respectively (*Garvin et al.*, 1998). The

Mission Name	Launch Date	Firing Rate (Hz)	Horizontal Accuracy	Vertical Precision	Vertical Accuracy
Apollo 15, 16, 17[a]	1971-1972	0.06	30 km	4 m	400 m
Clementine[a]	1994	0.6	3 km	40 m	90 m
SLA-01[a]	01/1996	10	40 m	0.75 m	2.78 m
SLA-02[a]	08/1997	10	40 m	0.75 m	6.74 m
NLR[a]	02/1996	1-2	20 m	0.31 m	10 m
MOLA[a]	11/1996	10	100 m	0.38 m	1 m
MLA[b]	08/2004	8	15-100 m	1 m	20 m
Kaguya[c]	09/2007	1	50 m	5 m	1 m
Chang'e 1[d]	10/2007	1	30 m	50-100 m	1 m
LOLA[e]	06/2009	28	50 m	10 cm	1 m

Table 1.1: Comparison of laser altimeters flown on planetary missions, from [a]*Neumann* (2001), [b]*Zuber et al.* (2012b); *Smith et al.* (2012), [c]*Araki et al.* (2009), [d]*Li et al.* (2010); *Ping et al.* (2009), and [e]*Smith et al.* (2010a); *Barker et al.* (2014).

NEAR Laser Rangefinder (NLA) was carried on NEAR Shoemaker, a spacecraft that orbited asteroid 433 Eros several times before touching down on the surface (*Zuber et al.*, 2000). The Mars Orbiter Laser Altimeter (MOLA), launched in November of 1996, provided the first global topographic dataset from laser altimetry for Mars (*Smith et al.*, 2001). The Mercury Laser Altimeter (MLA) was launched in 2004 on the MESSENGER (MErcury Surface, Space ENvironment, GEochemistry, and Ranging) spacecraft and, following two flybys in 2008, entered orbit around Mercury in March of 2011. Both the Japan Aerospace Exploration Agency (JAXA) and the Chinese Lunar Exploration Program launched lunar missions in 2007, Kaguya and Chang'e 1, respectively, and each mission carried a laser altimeter (*Araki et al.*, 2009; *Li et al.*, 2010; *Ping et al.*, 2009).

The Lunar Reconnaissance Orbiter (LRO) was launched in June of 2009, carrying the Lunar Orbiter Laser Altimeter (LOLA), the first multibeam laser altimeter designed to measure planetary surface topography (*Smith et al.*, 2010a). A diffractive optical element splits a single laser beam into five output beams, each of which illuminates a 5-m-diameter spot on the surface, and the backscattered pulses are detected and stored independently by the receiver (*Smith et al.*, 2010b). The 28-Hz pulse repetition rate results in a total sampling rate of 140 measurements per second, and, to date, more than 6.3 billion elevation measurements have been recorded (*Barker et al.*, 2014). Successive laser shots are separated by approximately 57 m, and the smallest distance between spots is 25 m (see Figure 2.1). The 5-spot pattern allows for calculation of surface slopes both between laser shots (along-track) and within individual spots in two orthogonal directions, for the first time providing an estimate of the true gradient at one particular scale (*Rosenburg et al.*, 2011). LOLA's high firing rate, multispot pattern, and high precision and accuracy have provided an unprecedented topographic dataset for the Moon that is well suited for investigations of surface roughness and the statistics of cratered terrains like those presented in the following chapters.

1.2 Chapter Overview

This thesis focuses on two interrelated aspects of the lunar topography: impact cratering and surface roughness. The former is the dominant agent of lunar surface modification, both today and throughout most of the Moon's history (*Wilhelms et al.*, 1987). The process of impact cratering and the landscapes it creates have been extensively studied in terms of size-frequency distributions of craters and their implications for relative surface ages (*Shoemaker and Hackman*, 1962; *Neukum et al.*, 1975; *Hartmann*, 1984). Impact cratering at many scales, from large basin-forming events to micrometeorite bombardment, also produces characteristic surface roughness features, and the relationship between the two is the subject of the investigations presented here.

The structure of the remaining chapters reflects the two parallel approaches we take to understanding lunar surface roughness and its relation to impact cratering: analysis of high-resolution elevation data from LOLA and forward modeling of cratered terrains. Chapter 2 presents global surface roughness maps using a variety of roughness parameters, including median absolute slope at several scales, median bidirectional slope at the LOLA footprint scale, median differential slope, and Hurst exponent. We explore major regional differences in roughness properties and find that the scale-dependence of lunar surface roughness reveals a change in character at approximately the 1-kilometer scale in the lunar highlands. The next chapter focuses this analysis on several local regions to assess the geologic applications of roughness maps at the lunar south pole, Shackleton crater, and mare surfaces of varying age. Chapter 3 presents a cratered terrain model that we have developed to track both the three-dimensional topography and surviving rim fragments of individual

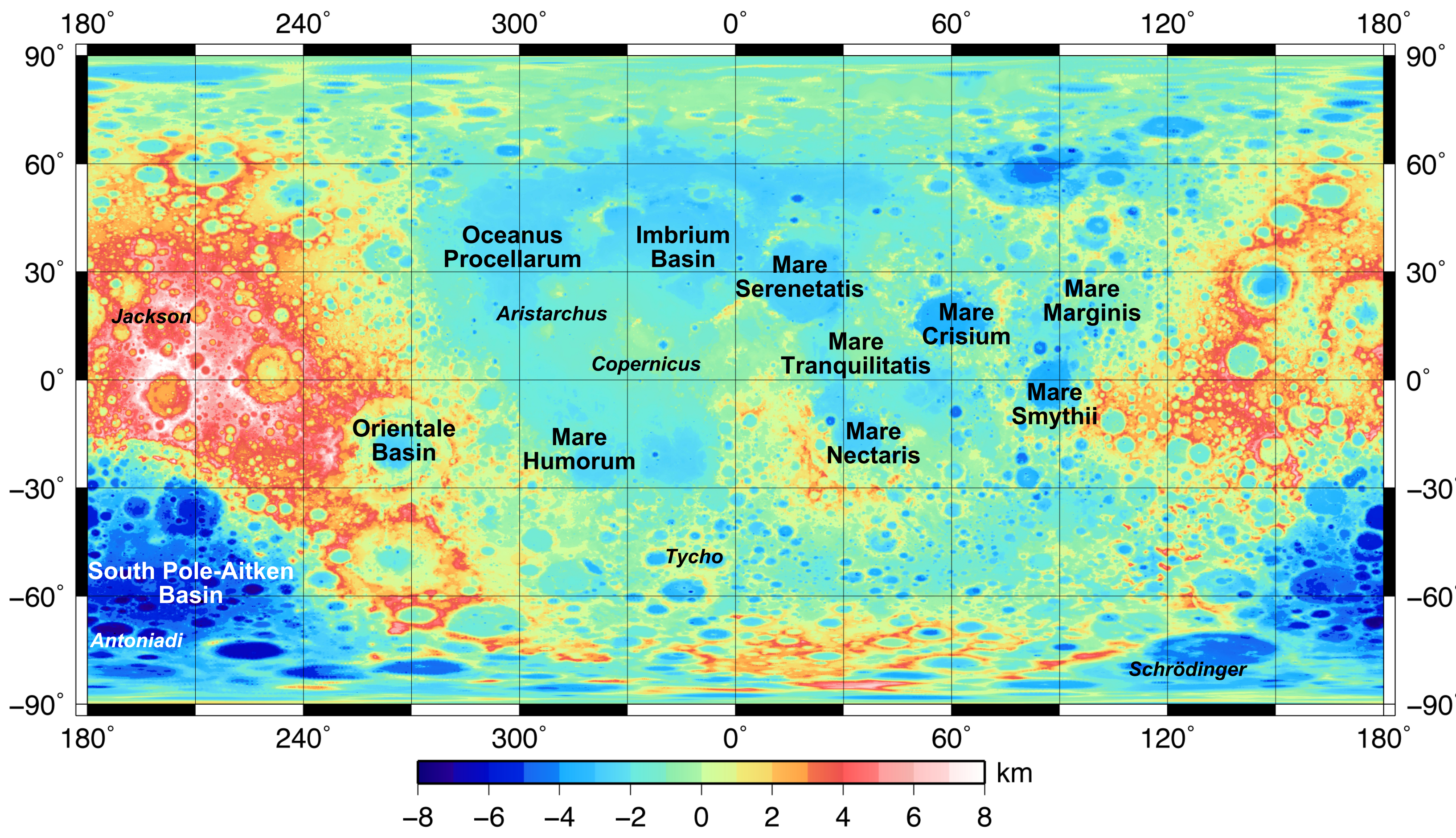

Figure 1.1: Lunar topography from the Lunar Orbiter Laser Altimeter (LOLA) in a simple cylindrical projection, with major basins and relevant features.

craters through time. The dependence of the power spectral density (PSD) on the size-frequency distribution of emplaced craters and the spectral content (shape) of individual craters is explored both analytically and numerically and compared to the PSD along LOLA transects. The final chapter employs the crater rim-tracking capability of the numerical model to investigate the evolution of the size-frequency distribution of "visible" craters as craters accumulate and overlap each other, addressing the geometric bias that results from over- or undercounting large craters and suggesting several potential solutions. Figure 1.1 contains a map of the lunar topography from LOLA that includes major geographical features that are relevant to the work presented in the following chapters.

Chapter 2

Global Surface Slopes and Roughness from the Lunar Orbiter Laser Altimeter

Originally published in:

Rosenburg, M., O. Aharonson, J. Head, M. Kreslavsky, E. Mazarico, G. Neumann, D. Smith, M. Torrence, and M. Zuber (2011), Global surface slopes and roughness of the moon from the lunar orbiter laser altimeter, *Journal of Geophysical Research: Planets (1991–2012)*, *116*(E2).

Abstract

The acquisition of new global elevation data from the Lunar Orbiter Laser Altimeter (LOLA), carried on the Lunar Reconnaissance Orbiter (LRO), permits quantification of the surface roughness properties of the Moon at unprecedented scales and resolution. We map lunar surface roughness using a range of parameters: median absolute slope—both directional (along-track) and bidirectional (in two dimensions)—median differential slope, and Hurst exponent, over baselines ranging from ∼17 m to ∼2.7 km. We find that the lunar highlands and the mare plains show vastly different roughness properties, with subtler variations within mare and highlands. Most of the surface exhibits fractal-like behavior, with a single or two different Hurst exponents over the given baseline range; when a transition exists, it typically occurs near the 1-km baseline, indicating a significant characteristic spatial scale for competing surface processes. The Hurst exponent is high within the lunar highlands, with a median value of 0.95, and lower in the maria, with a median value of 0.76. The median differential slope is a powerful tool for discriminating between roughness units and is

useful in characterizing, among other things, the ejecta surrounding large basins, particularly Orientale, as well as the ray systems surrounding young, Copernican-age craters. In addition, it allows a quantitative exploration on mare surfaces of the evolution of surface roughness with age.

2.1 Introduction

As signatures of surface evolution processes acting over geologic time, surface slopes and slope distributions provide important clues to the morphologic history of a planetary surface in terms of both formation and modification mechanisms. Moreover, the comparison of surface regions based on quantitative measures of roughness and its scale dependence is a powerful tool for interpreting the relationships between geologic and topographic units and their origins, and has been successfully employed for various planetary bodies, including Earth (*Morris et al.*, 2008; *Neumann and Forsyth*, 1995; *Smith and Jordan*, 1988), Mars (*Aharonson et al.*, 2001; *Orosei et al.*, 2003; *Kreslavsky and Head*, 2000), and Venus (*Sharpton and Head*, 1985). Attempts to study surface roughness on the Moon have spanned the decades between the Apollo era and the present (*Daniels*, 1963; *Moore and Tyler*, 1973; *Yokota et al.*, 2008), yet, to date, no comprehensive study of surface slopes and slope distributions has been possible at high resolution and across many scales.

The Lunar Orbiter Laser Altimeter (LOLA) began collecting data in late June, 2009, after the successful entry into orbit of the Lunar Reconnaissance Orbiter (LRO) (*Smith et al.*, 2010a; *Zuber et al.*, 2010). With a ground track configuration consisting of five illuminated spots on the surface arranged in a cross pattern (Figure 2.1), LOLA allows for determination of slopes at multiple baselines, both between pairs of spots within each laser shot and between sequential shots. The high vertical precision (∼10 cm), accuracy (∼1 m), and high density (∼57-meter along-track spacing) of LOLA measurements permit an unprecedented opportunity for quantitative morphologic characterization of the lunar surface relevant to current and past surface processes, as well as to future lunar landing site selection. For comparison, the Mars Orbital Laser Altimiter (MOLA) operated with a vertical precision of ∼1.5 m, a spatial accuracy of ∼100 m (including pointing errors), and an along-track spacing of ∼300 m (*Smith et al.*, 2001).

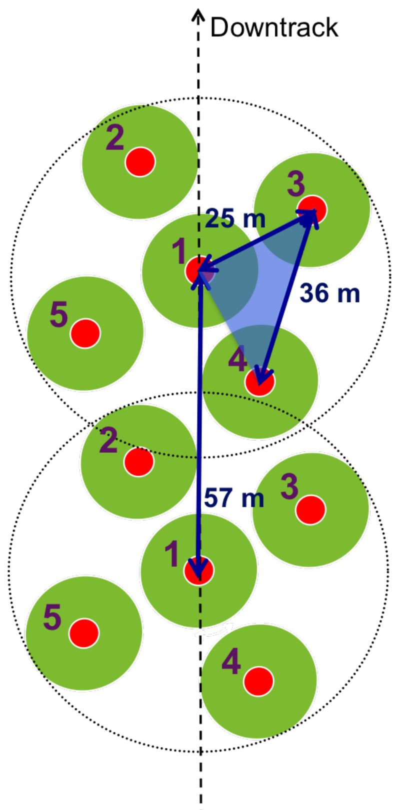

Figure 2.1: Plan view of two consecutive LOLA shots with spot numbers labeled. The shot-to-shot distance is ∼57 meters, and the smallest point-to-point baseline available is ∼25 m. An example of a triangle used to calculate bidirectional slopes is shaded in blue. Red circles indicate the illuminated footprint of each laser spot, while green circles represent the field of view of each detector.

2.2 Topography Data

LRO maintains a nearly circular, 50-km polar orbit that scans all longitudes of the Moon each month. We use 3,180 tracks from the commissioning and mapping mission phases, acquired from September 17, 2009, to March 9, 2010, to compute and analyze a variety of parameters describing surface slopes and roughness. The data have been processed to remove anomalous points (due to instrumental effects such as noise), and are spaced ∼57 meters apart along track and (on average) ∼3.8 km across track at the equator and closer at the poles. Additional data have narrowed the cross-track spacing to ∼1.8 km at the equator (*Smith et al.*, 2010b).

2.3 Global Surface Roughness of the Moon

Quantitative measures of surface roughness have been defined in the literature in a number of ways. Here, we investigate several measures of surface roughness, both in the interest of robustness in characterizing roughness units, and in order to facilitate comparison with the literature. For one-dimensional slopes, we examine the root mean square (RMS) slope, the median absolute slope, and the median differential slope for a variety of horizontal scales, as well as the Hurst exponent, which describes how slopes scale with baseline (the baseline is the horizontal length-scale over which the slope is measured). In addition, LOLA's 5-spot pattern allows for the calculation of two-dimensional slopes by fitting a plane to a set of three points along the track, resulting in the magnitude and direction of steepest descent.

2.3.1 RMS and median slopes

The RMS slope is routinely calculated for the statistical analysis of topography because radar reflection scatter is often parameterized with this metric. In one dimension, it is defined as the RMS difference in height Δz between each pair of points (also known as the deviation, ν) divided by the distance between them, Δx:

$$s\left(\Delta x\right)=\frac{\nu\left(\Delta x\right)}{\Delta x}=\frac{1}{\Delta x}\langle\left[z\left(x_{i}\right)-z\left(x_{i-1}\right)\right]^{2}\rangle^{\frac{1}{2}}, \tag{2.1}$$

where the angle brackets indicate the mean. However, because the RMS slope depends on the square of the deviation, this parameter is quite sensitive to outliers; this poses a significant problem because the slope-frequency distribution for natural surfaces is often non-Gaussian with strong tails. The median absolute slope is a more robust measure of typical slopes, as it is less affected by long tails in the distribution.

To find the RMS and median slope in the along-track direction, point-to-point slopes were calculated for each track, stored at the midpoint, and averaged according to (1) within 0.5-degree (∼15-km) sliding windows, each spaced 0.25 degrees (∼7.5 km) apart. The LOLA lasers have a firing frequency of 28 Hz, corresponding to a shot density of approximately 540 shots per degree downtrack, or roughly 270 shots per window at best. However, due to noise and instrument performance issues, missing points are not uncommon. Since the RMS slope is sensitive to the number of points, N, included in each window, uneven N across the surface can introduce variations in the RMS slope map that are not due to real roughness features. To minimize this bias, windows were only considered valid if more than 250 measurements contributed to the average in that location. The median absolute (unsigned) slope is far less sensitive to the number of points in each bin. Given LOLA's ground spot pattern, the smallest baseline available for slope calculations is about 25 m, the distance on the surface from the center spot to any of the four corners (Figure 2.1).

One-dimensional slopes calculated along profile underestimate the true gradient of the surface wherever the direction of steepest descent diverges from the along-track direction. At the smallest scales, this ambiguity can be resolved by computing the slopes in two dimensions from multiple points within each laser shot. We use vector geometry to compute the plane passing through three spots, recording the magnitude and azimuth of the slope. One such triangle appears as a shaded region in Figure 2.1. The effective baseline of the slope is taken to be the square-root of the area of the triangle. The slope values are then binned as before, and the median reported for 0.5-degree overlapping windows spaced 0.25-degrees apart.

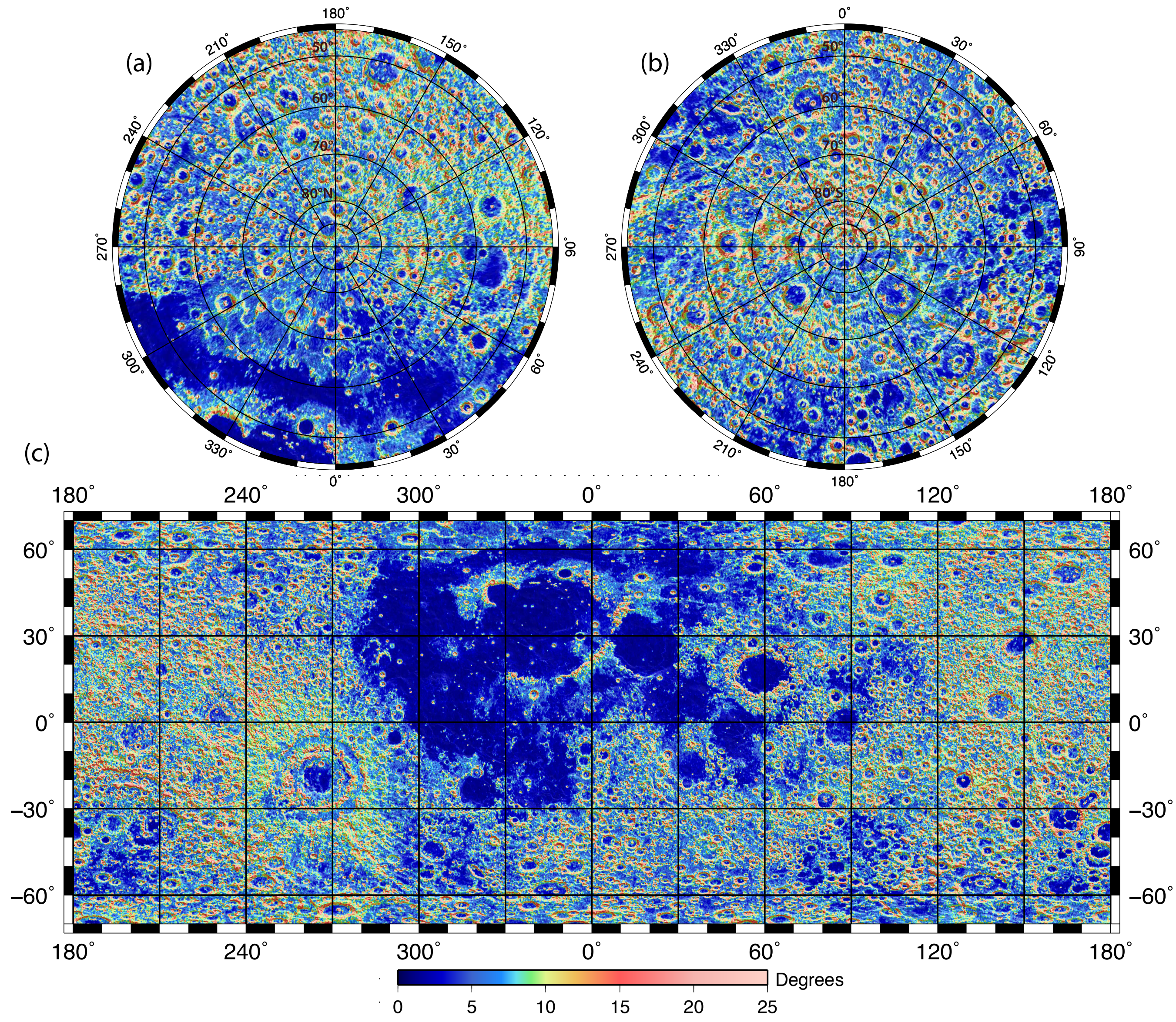

Figure 2.2: Median bidirectional slope map at the ∼17-meter effective baseline. Slopes are calculated by fitting a plane between three elevation data points. Median slopes are reported for 0.5-degree windows spaced 0.25 degrees apart. (a) The north pole, shown from 45°N and (b) the south pole from 45°S, both in a stereographic projection. (c) Cylindrical equidistant projection of the latitudes from 70°S to 70°N.

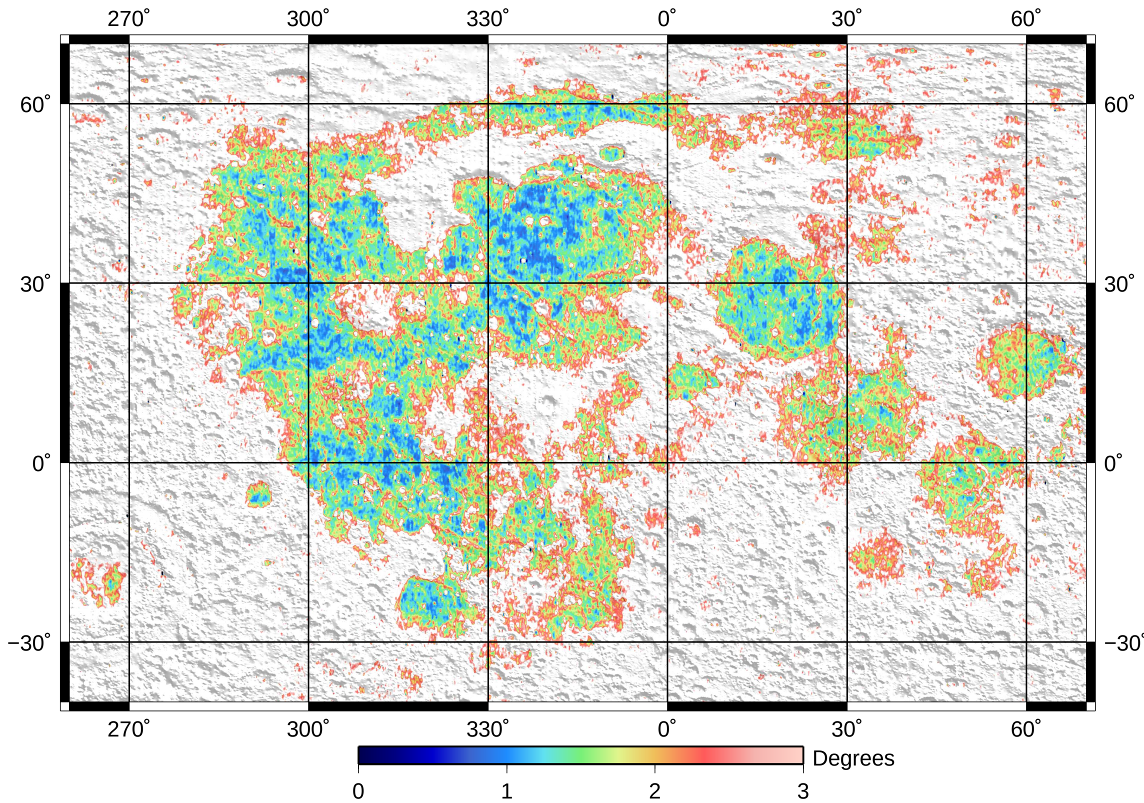

Figure 2.3: Median bidirectional slope, as described in Figure 2.2, with a color stretch designed to emphasize the subtle variations in slope within the lunar maria. Large-scale flow fronts and tectonic features such as wrinkle ridges appear as long, continuous regions of slopes higher than the surrounding plains, and are most evident within the Imbrium, Crisium, and Serenetatis basins.

A map of the median bidirectional slope at the ∼17-meter scale is shown in Figure 2.2. Note that while the results are reported in units of degrees, the statistics are computed in gradient units (m/m). The maria are easily distinguishable from the highlands as smooth regions with median slopes $\leq 3°$, while the steepest median slopes ($\geq 10°$) occur within crater walls and the blocky ejecta blankets surrounding major impact basins and young rayed craters. The multi-ring structure of the Orientale impact basin is clearly visible in surface slopes at this scale, along with the topographically expressed secondary crater chains emerging radially from the continuous ejecta deposit.

The floor of South Pole-Aitken basin appears as a region of subdued slope; a sampling of the basin floor (excluding mare deposits, which would contribute their own roughness signature) has a median slope of 5.8°, nearly two degrees lower than the median value for the highlands, 7.5°, although the distributions overlap (see Table 2.1). Within the nearside mare plains, large-scale flow fronts and wrinkle ridges are delineated by subtle variations in slope, particularly evident within the Imbrium, Serenetatis, and Crisium basins (Figure 2.3). Slopes rapidly transition between the two major highland and mare roughness units at their boundaries, where mare basalts are often tilted and deformed (*Solomon and Head*, 1980) and have only partially embayed the surrounding rougher terrain.

For isotropic topography, a relationship exists between point-to-point and bidirectional slope distributions: given a one-dimensional slope distribution, the equivalent distribution of two-dimensional slopes can be found by applying a statistical correction. The probability distribution functions of the 1D slopes $F(p)$ and 2D slopes $F(s)$ are related by *Aharonson and Schorghofer* (2006):

$$F(p) = \int_{|p|}^{\infty} \frac{F(s)}{\sqrt{s^2 - p^2}} ds. \tag{2.2}$$

In practice, this integral equation may be discretized and inverted. Figure 2.4 is a global comparison of our measured slopes in one and two dimensions and the adjusted point-to-point slope histogram. We find moderately good agreement between measured bidirectional slopes and those predicted from the 1D slope distribution, although the 2D measured slopes are slightly steeper than predicted from the 1D distribution, typically by 25%. We can place constraints on two factors that contribute to this discrepancy. Anisotropy in our slope measurements occurs when triangles with high aspect ratios are used for plane fitting. LRO's orbital configuration creates a preferred direction for the long axis of these triangles, and because slopes are generally shallower at longer baselines, the azimuthal distribution is skewed to favor the perpendicular to the downtrack direction. To minimize this effect, we included only triangles with low aspect ratios, using spots 1, 3, and 4. While some anisotropy remains, this consideration improves the agreement by nearly a factor of 2. Part of the discrepancy is also due to the fact that comparing slopes at similar baselines is rendered difficult by instrument constraints. The minimum baseline for point-to-point slopes ($\sim$25 m) is larger than the effective baseline of our preferred triangles ($\sim$17 m). As a result, bidirectional slopes have a tendency to be larger than their 1D counterparts, where a component of this difference is due solely to the mismatch in baselines. A slightly better agreement can be obtained by using a local Hurst

	Highlands	Maria	South Pole-Aitken Basin (All)	South Pole-Aitken Basin (Floor)	South Pole	North Pole
Median Slope at the ~17-m Effective Baseline (°)	$7.5^{+12.3}_{-4.2}$	$2.0^{+4.1}_{-1.0}$	$7.2^{+12.0}_{-3.0}$	$5.8^{+10.5}_{-3.0}$	$7.6^{+12.4}_{-4.2}$	$6.9^{+11.5}_{-3.8}$
Median Hurst Exponent	$0.95^{+0.97}_{-0.92}$	$0.76^{+0.85}_{-0.63}$	$0.95^{+0.97}_{-0.93}$	$0.94^{+0.97}_{-0.91}$	$0.95^{+0.97}_{-0.92}$	$0.94^{+0.96}_{-0.91}$
Median Breakover Scale (km)	$0.98^{+1.13}_{-0.74}$	$0.53^{+0.97}_{-0.24}$	$1.01^{+1.14}_{-0.81}$	$1.01^{+1.15}_{-0.82}$	$1.01^{+1.15}_{-0.79}$	$0.97^{+1.12}_{-0.73}$
Typical Deviogram Shape(s)	Monofractal Bilinear	Complex	Monofractal Bilinear	Monofractal Bilinear Complex	Monofractal Bilinear	Monofractal Bilinear Complex

Table 2.1: Statistical estimators of surface roughness properties for major lunar geographic regions. The median value is reported along with the 25% and 75% percentile points as a measure of the width of each distribution.

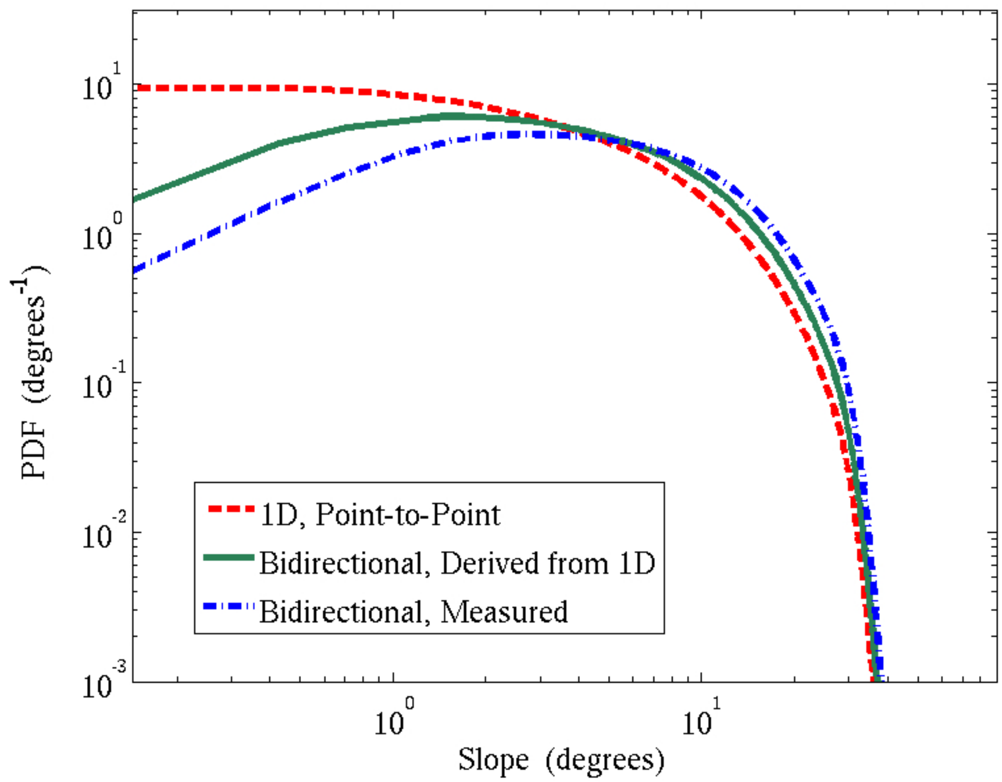

Figure 2.4: Global slope histograms for the Moon. The red line (dashed) shows the distribution of measured point-to-point slopes at the 25-meter baseline. This distribution is recalculated to the green line (solid) using the method of *Aharonson and Schorghofer* (2006) to predict bidirectional slopes from the one-dimensional slope histogram. Measured bidirectional slopes at the ∼17-meter scale are shown in blue (dot-dash). All distributions are normalized such that the integral of the probability density function is equal to 1. Assuming that the topography is indeed isotropic, the remaining discrepancy in the measured and derived distributions is due to the geometry of the triangles used to measure 2D slopes, and to the mismatch in scales over which the slopes are measured in each case. Both effects are constrained by LRO's orbital configuration and instrument limitations.

exponent (defined in section 3.3) to scale the slope distribution to a common horizontal baseline. However, this demands additional assumptions and the improvement is not large.

2.3.2 Median differential slope

The median differential slope is a measure introduced by *Kreslavsky and Head* (2000) in order to disentangle small- and large-scale contributions to surface roughness. For the baseline of interest, L, it isolates roughness features on the order of L by subtracting the point-to-point slope at twice the given baseline:

$$s_d = \frac{z_{\frac{L}{2}} - z_{-\frac{L}{2}}}{L} - \frac{z_L - z_{-L}}{2L}. \tag{2.3}$$

The resulting value, s_d, is a measure of slopes at a certain scale with respect to longer-wavelength features.

As with the RMS and median bidirectional slopes, median differential slopes were calculated in 0.5-degree windows spaced 0.25 degrees apart, and only those windows with more than 250 measurements were retained. Following *Kreslavsky and Head* (2000), differential slopes at a given baseline were calculated according to Equation (2.3) by subtracting slopes calculated at two different baselines. Practically, this involves calculating the position of each slope midpoint along the track length and interpolating the slope midpoints at the longer baseline to the points occupied by the smaller-baseline slope profile to accomplish the subtraction at the correct location. This method ensures that the two slope profiles are always aligned correctly, thereby avoiding errors in the value of the differential slope calculated. This procedure is identical to the detrending process described in section 2.3.3 and illustrated in Figure 2.6, except that the ratio of baselines is always 2.

Differential slopes were calculated in this manner for all baselines ranging from one shot spacing apart (~57 m) to 25 shot spacings apart (~1.4 km). Only profiles involving a single laser spot were considered for the calculation, in order that the slopes over multiple baselines be computed along the same direction. Figure 2.5 shows a composite color map of the lunar surface which presents roughness at three different scales, ~560 m (10 shot spacings) in the red channel, ~220 m (4 shot spacings) in

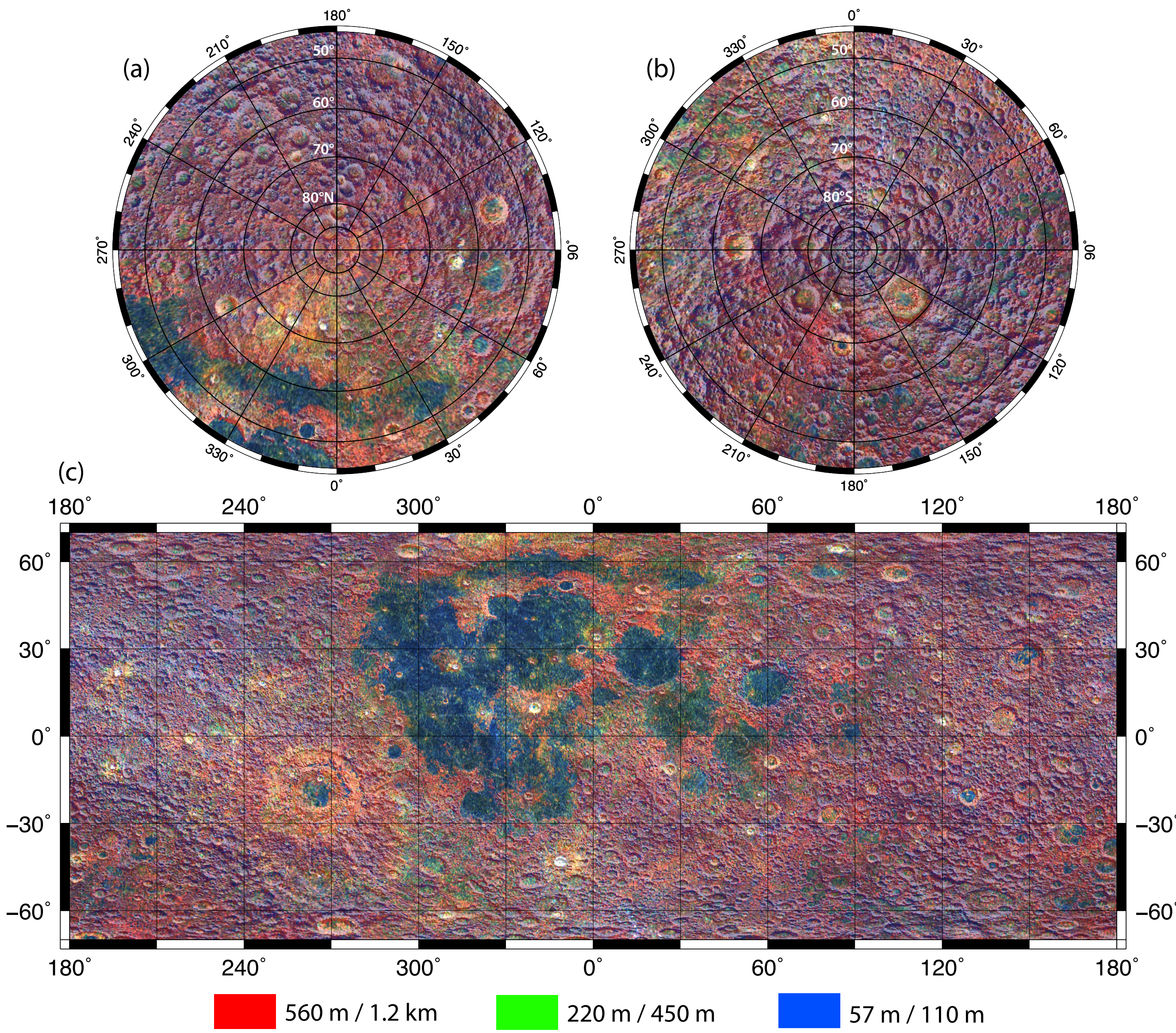

Figure 2.5: Composite color map of median differential slope. Differential slopes at three different baselines were calculated according to Equation 2.3. The blue channel corresponds to roughness at the smallest scale considered, one shot spacing, or ∼57 m. Green represents roughness at the ∼220-meter baseline, and red the ∼560-meter baseline. Map projections are the same as in Figure 2.2.

green, and ∼57 m (1 shot spacing) in blue. Variations in the roughness properties across the surface are apparent and substantial, showing intriguing characteristic signatures for several terrain types. The lunar maria are roughest at the smallest scale and smoother at large scales, making them easily distinguishable by their blue tones in the composite image. A comparison of mare ages (*Hiesinger et al.*, 2010) to Figure 2.5 shows that flows of different ages have different roughness signatures; the youngest (e.g., those within Oceanus Procellarum and Mare Imbrium) are rough only at the smallest scale, while successively older flows (e.g., Mare Tranquilitatis and Mare Marginis) increase in roughness at larger scales. At the smallest scale, roughness remains approximately constant with age, potentially indicating that saturation on small scales occurs on relatively swift timescales. In the composite map, these age variations correspond to a transition in color from deep blue to blue-green. The ejecta surrounding major basins—particularly around Orientale, but also older basins—are roughest at the longest scale, causing these regions to appear orange or red. Young, Copernican-age craters appear white because they are bright in all channels; the least modified features on the Moon, they are rough at all scales. Moreover, the ray systems related to these craters, so evident in albedo maps, but not obviously expressed as topographic relief, are roughest at the intermediate scale, probably reflecting crater chains and clusters that often populate crater rays (*Oberbeck*, 1975; *Pieters et al.*, 1985). As a result, they are clearly expressed as star-shaped yellow to orange haloes surrounding each feature (Figure 2.6). Other, subtler variations, not obviously related to a single geologic feature, occur across much of the surface. The region spanning latitudes 30°S to 60°N and longitudes 160°E to 240°E, representing a large uninterrupted stretch of lunar highlands, appears relatively bright and with a mottled appearance, consistent with an old surface saturated with craters at many different scales. South Pole-Aitken basin is somewhat redder than its surroundings, except for the patches of mare within superimposed craters.

As a diagnostic tool for distinguishing unique roughness units, the median differential slope is a useful measure of surface roughness. However, because it involves measuring small-scale roughness with respect to long-wavelength roughness features, it can be more difficult to interpret physically as a slope characteristic. For this reason, the median absolute slope at a given scale is a more intuitive

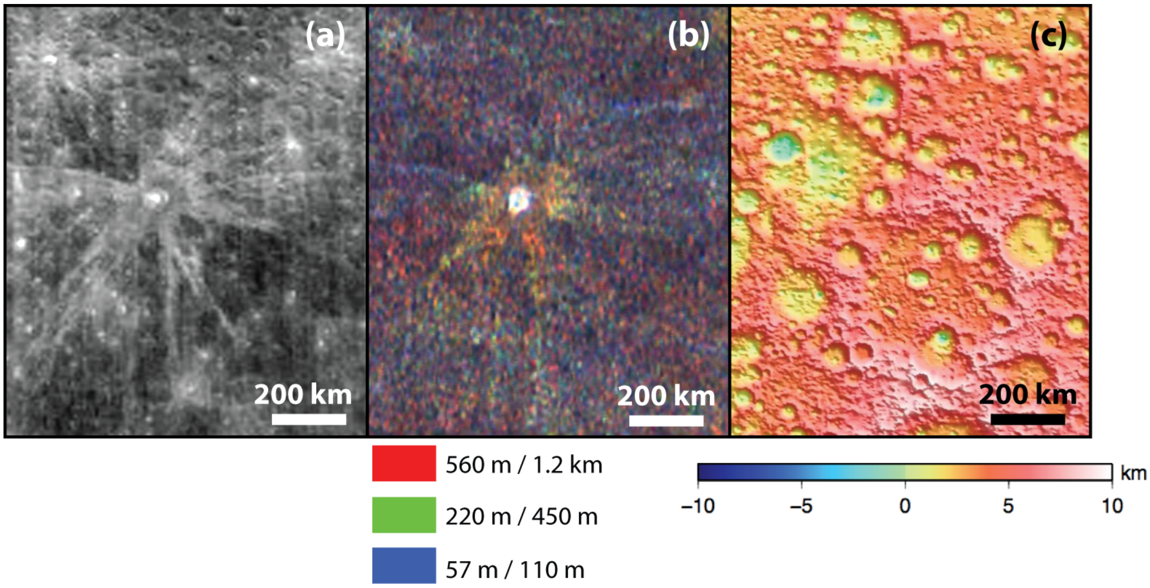

Figure 2.6: Lunar far-side crater Jackson and its ray system, centered at 19°E and 22.4°N, shown in (a) the 750-nm Clementine albedo map (*McEwen and Robinson*, 1997), (b) the median differential slope map, as in Figure 2.5, and (c) the topography (*Smith et al.*, 2010b). Rays of young, Copernican-age craters are clearly expressed as streaks of high albedo relative to the background. Though they do not add obvious relief to the topography, the rays are distinctly rougher at the ~220-meter and ~560-meter baselines compared to the highlands, making them appear yellow to orange in the composite roughness map.

parameter.

2.3.3 Hurst exponent

Topography is often considered as a nonstationary random field with self-affine fractal-like properties (*Turcotte*, 1997). Self-affinity implies a scaling behavior such that an increase of factor r in the horizontal length scale corresponds to an increase in the vertical length scale of r^H, where H is known as the Hurst exponent and falls between 0 and 1 for real surfaces (*Turcotte*, 1997; *Orosei et al.*, 2003). The Hurst exponent is directly related to both the fractal dimension of the surface, $D = 1+d-H$, and the slope of the power spectrum, $\beta = 2H+d$, where in each case d is the number of spatial dimensions: 1 for a profile or 2 for a surface (*Schroeder and Wiesenfeld*, 1991).

The Hurst exponent describes the power law behavior of surface slopes when they are scaled to different horizontal baselines:

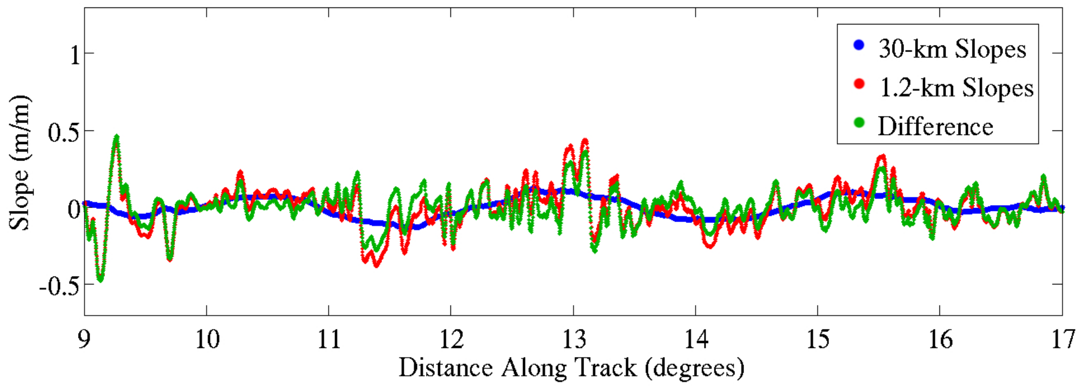

Figure 2.7: Method of detrending slope data. Slopes measured at the ∼30-km baseline (in blue) are subtracted from ∼1.2-km slopes (red), leaving a detrended slope profile behind (green) and avoiding large-scale tilts in the topography.

$$s(\Delta x) = s_0 \left(\frac{\Delta x}{\Delta x_0}\right)^{H-1} = \frac{\nu(\Delta x)}{\Delta x}. \tag{2.4}$$

Written as such, it is clear that the deviation $\nu(\Delta x) \propto (\Delta x)^H$. H can thus be estimated as the slope of a best-fit line to log $\nu(\Delta x)$ vs. log (Δx) (*Orosei et al.*, 2003).

We calculate the RMS deviation for a range of baselines from ∼57 m to ∼2.7 km (1 to 50 shot spacings) and analyze the deviogram, or structure function, $\nu(\Delta x)$. As in the previous calculations, the deviation values were calculated along track in overlapping windows. However, *Shepard et al.* (2001) have shown that errors can be introduced when the range over which the Hurst exponent is fit exceeds 10% of the topographic profile length (the window size). Therefore, we use 1-degree (30-km) windows for this calculation, spaced 0.5 (15 km) apart. We use only shot-to-shot profiles of laser spot 3, selected for its consistency.

To remove roughness features on the order of our window size, we detrend each deviogram at the 30-km scale. This process de-emphasizes large-scale roughness features in favor of small-scale features of more interest to this study, and it avoids biases due to long-wavelength trends that are undersampled within each window (*Shepard et al.*, 2001). Figure 2.7 shows how the detrending is accomplished. Slopes measured at the 30-km baseline are subtracted from small-scale slopes, leaving a slope profile with a mean near zero within the window. Slopes at scales less than 3 km are only slightly affected by the detrending process except where long-wavelength slopes are high, as, for example, those near mountain ranges.

In some cases, the deviograms are well characterized by a single log-log slope (exponent), but many others transition to a different slope at a certain length scale. This behavior is well documented in the literature for other planetary surfaces (*Shepard et al.*, 2001; *Morris et al.*, 2008), and is often attributed to surface processes acting at small and large scales. For the Hurst exponent fit within each window along the track, we use baselines ranging from one shot spacing (∼57 m) to the breakover scale—the point where the deviogram diverges from a straight line, Δx_0—for that location. Figure 2.8 is a map of the Hurst exponent calculated in this way. Although the baseline range used in this map varies over the surface, this method avoids including fits to nonlinear sections of each deviogram and thus presents a more accurate estimate of the Hurst exponent at the smallest available scales.

The highest Hurst exponents on the Moon are found in the highlands within crater walls and the rims and ejecta of large basins, and in these regions values above 0.95 are not uncommon. This result is surprising, given that typical Hurst exponents for topographic surfaces on the Earth and Mars are lower, between 0.7 and 0.9 (*Kreslavsky and Head*, 2000; *Orosei et al.*, 2003; *Morris et al.*, 2008). A Hurst exponent of 1 implies self-similar topography, meaning the roughness at small scales is exactly replicated at large scales. The high values observed for the lunar highlands may be related to the density of impact craters in these regions and the absence of competing morphologic processes to transport fine material downhill. Hurst exponents within the lunar maria are lower than those within the highlands, with a median value of 0.76, indicating smoother topography at large scales relative to small scales.

To classify deviogram shapes, we use a method similar to that of *Main et al.* (1999) which establishes whether a given deviogram is best fit by one line or by two, or whether the deviogram is poorly fit by any linear model. We compute the least squares fits in each case and compare the sums of the residuals, adding a penalty when additional parameters are introduced into the fit (i.e., three parameters are required for a line, five for two lines). This method classifies each deviogram by its

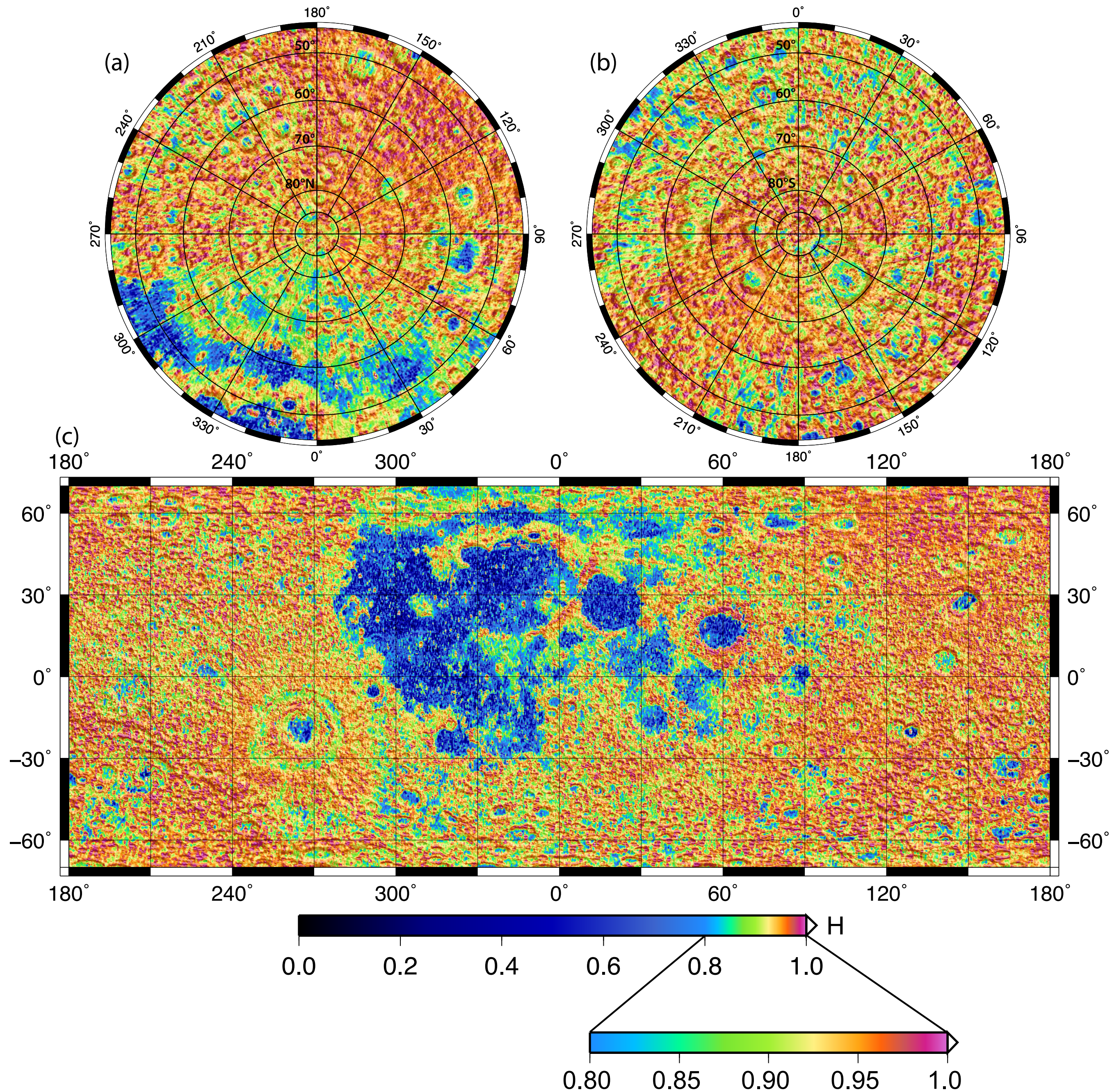

Figure 2.8: Hurst exponent map. For each 0.5-degree pixel, the Hurst exponent is computed as the slope of the best fit line to the deviogram, over the baseline range beginning at one shot spacing (∼57 m) and extending to the breakover point for that location, Δx_0. The color scale was chosen to emphasize the dynamic range of the variations between 0.8 to 1, although substantially smaller H is common in the maria. Map projections are the same as in Figure 2.2.

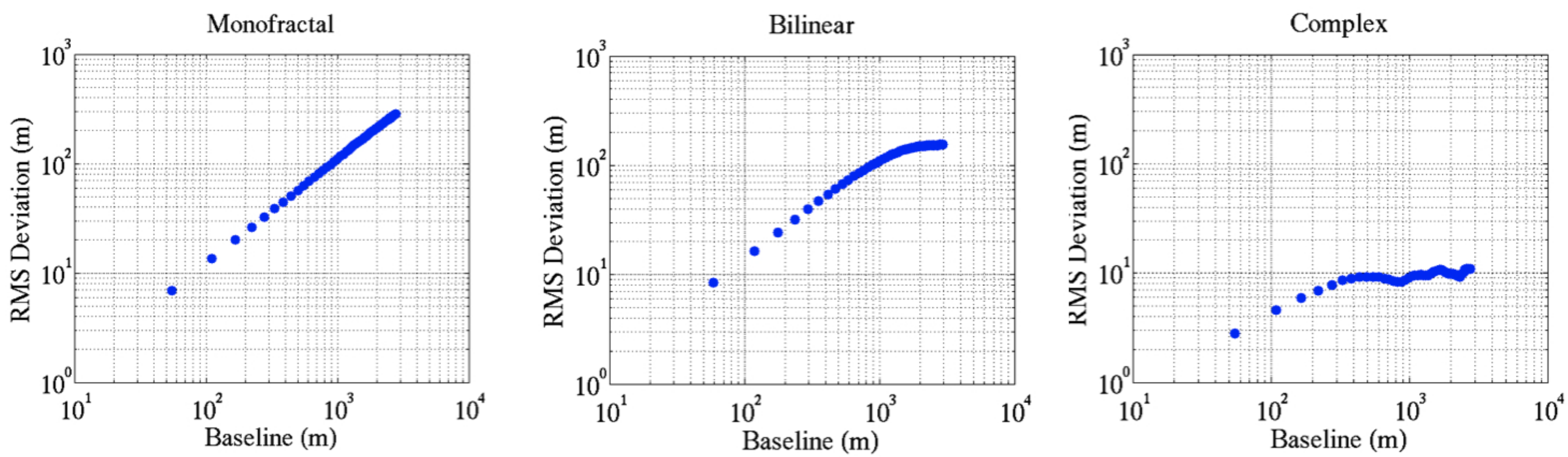

Figure 2.9: Observed deviogram shapes. Though many deviograms are monofractal over the baseline range explored (from 1 to 50 shot spacings, or ∼57 m to ∼2.7 km), most are bilinear, breaking over to a shallower slope at a certain breakover baseline. Many others exhibit complex behavior that is not well characterized by a line over a given portion of the baseline range.

shape (Figure 2.9) and yields the relevant slope(s) of the deviogram, an estimate of the breakover baseline, Δx_0, and confidence intervals on all of the above.

Figure 2.10 shows the distribution of deviogram shapes across the surface of the Moon and how they partition among major topographic regions. Polygons defining the lunar maria were taken from the USGS series of geologic maps of the Moon (*Wilhelms et al.*, 1971, 1977; *Scott and McCauley*, 1977; *Lucchitta and Center*, 1978; *Stuart-Alexander and Center*, 1978; *Wilhelms et al.*, 1979) and used to select data within the mare plains. The rim of South Pole-Aitken basin was defined using the best-fit ellipse from (*Garrick-Bethell and Zuber*, 2009). The polar regions included latitudes from 60° to the pole, excluding patches of mare basalts and the South Pole-Aitken basin region. All areas falling outside these regions were designated highlands. By surface area, most deviograms are best characterized by two lines (∼59%), with the remainder of the surface nearly evenly divided between monofractal (∼17%) and complex (∼24%) deviogram shapes, in which the slope changes continuously and rapidly with baseline, often alternating sign. Complex deviograms are mainly found in the lunar maria, whereas the highlands exhibit primarily monofractal or bifractal behavior. Other geographic regions, including the north and south poles and the South Pole-Aitken basin, behave much like the lunar highlands. This partitioning indicates a profound difference in character between the two major units; on the one hand, highland deviograms behave as nearly self-similar fractals, while mare topography diverges from fractal behavior altogether at the breakover point.

Within areas that adhere to fractal behavior, the baseline at which the breakover occurs, Δx_0, is a significant parameter constrained by the two-line fit to the deviogram because it has a physical meaning related to the surface processes that contribute to the evolution of the Moon's topography. Formation and modification mechanisms act over a range of scales and may have distinct Hurst exponents. The breakover point is thus an estimate of the scale at which surface processes acting at longer scales are overtaken by those acting on smaller scales. In other words, it represents the baseline at which competing surface processes are equal contributors to the topography.

Figure 2.11 is a stacked histogram showing the distribution of breakover points for all deviograms and their locations within the major geographic regions. Within the maria, breakover points are

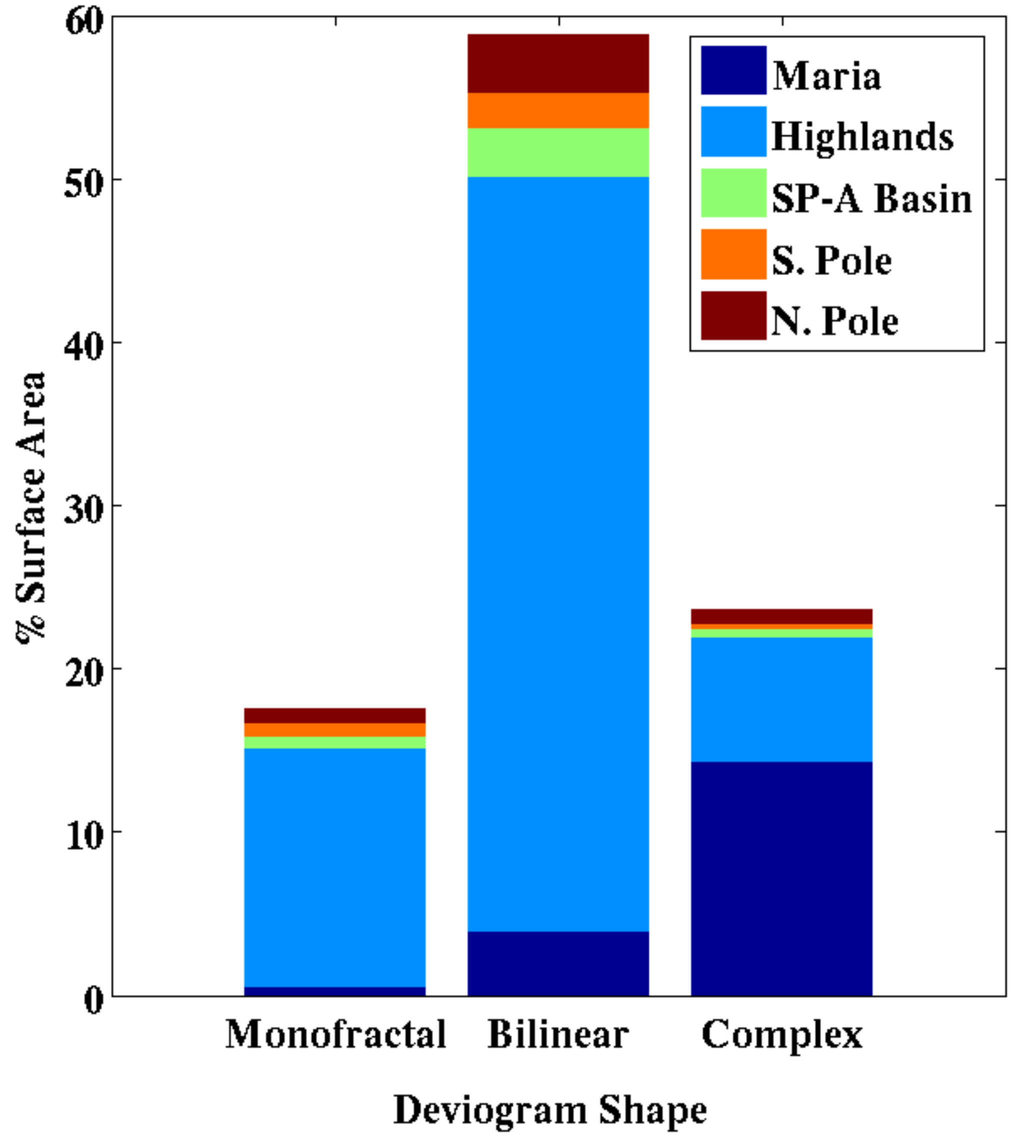

Figure 2.10: Abundance of deviogram shapes by surface area, sorted by region. The most common deviogram shape is bilinear (∼59%), with monofractal (∼17%) and complex (∼24%) making up the remaining area. The highlands are almost entirely bilinear and monofractal, while the maria contain primarily complex deviograms.

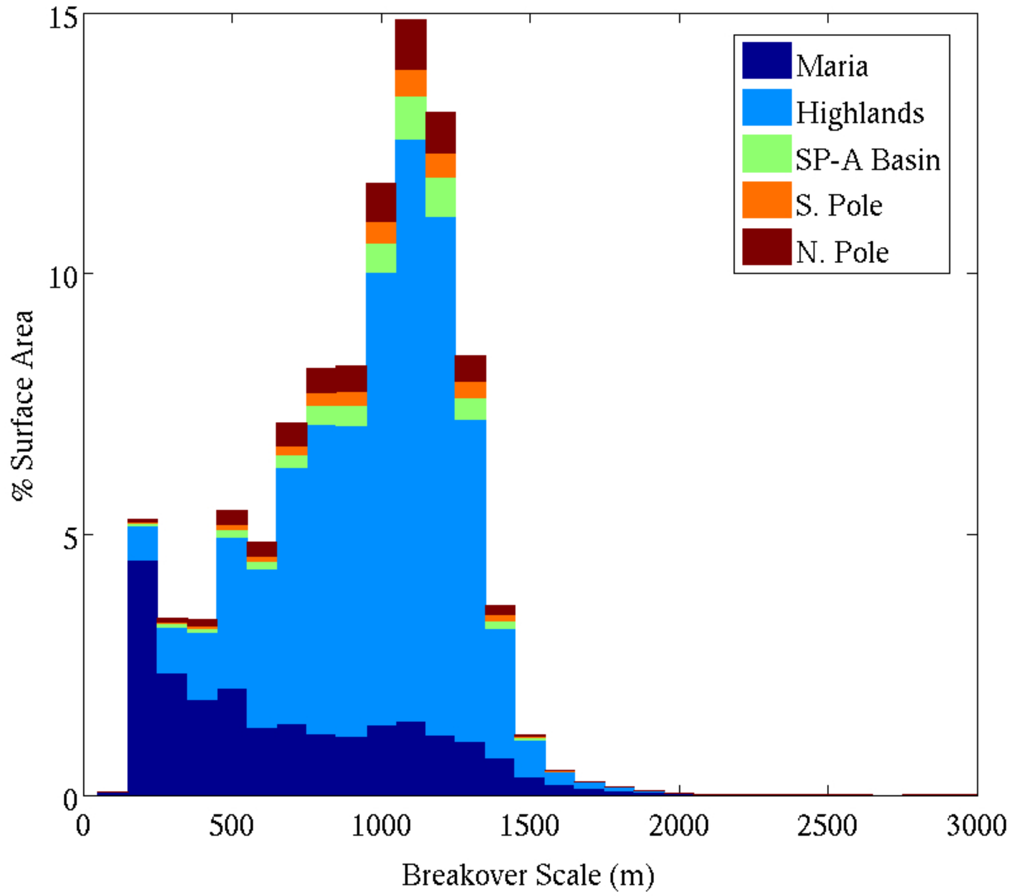

Figure 2.11: Breakover point histogram, sorted by region. Whereas the maria exhibit a broad range of breakover points, reflecting the complexity of deviograms in these regions, the other regions have a strongly-peaked distribution of breakover points near 1 km. This characteristic baseline indicates a transition between two surface processes, and may tell us about the Moon's surface history.

broadly distributed, reflecting the complex nature of the deviograms found there. All other regions, however, have a strong peak at ~1 km, suggesting a significant transition between surface processes acting above and below this scale. Impact cratering and mare basalt emplacement are most likely responsible for many of the key differences between the lunar highlands and the maria. Other processes that may have contributed to the observed roughness properties remain to be identified and quantified, but likely candidates for exploration include mass wasting, perhaps due to seismic shaking, ejecta mantling, and micrometeorite gardening.

2.4 Conclusions

New altimetry data from LOLA allow a unique opportunity to quantify the surface roughness properties of the Moon. We find that topography within the highlands and the mare plains exhibit substantially different behaviors, while other geographic regions show more subtle variations. Table 2.1 presents a summary of the most important roughness characteristics for each major region. For each parameter, the median is reported, as it best reflects a typical value for the region, along with the 25% and 75% percentile points, which indicate the shoulders of each distribution and hence provide an estimate of the width. We find that most of the surface is characterized by fractal-like behavior with either one or two Hurst exponents over the baseline range covered, from ~57 m to ~2.7 km, with a strong tendency to break over near the 1 km scale. The Hurst exponent is generally high in the lunar highlands, reflecting nearly self-similar topography in these regions. Within the maria, however, deviograms transition from fractal at small scales to complex at a range of breakover points, and the Hurst exponent is both lower and more diverse.

2.5 Acknowledgements

The authors would like to acknowledge the LRO and LOLA engineering teams, without whom the data presented here would not have been possible. The research was partially funded by NASA grants NNX08AZ54G and NNG09EK06C:1.

Chapter 3

Geologic Applications of Roughness Maps

Parts of the work presented here were originally prepared for and published in:

Zuber, M. T., J. W. Head, D. E. Smith, G. A. Neumann, E. Mazarico, M. H. Torrence, O. Aharonson, A. R. Tye, C. I. Fassett, M. A. Rosenburg, et al. (2012a), Constraints on the volatile distribution within shackleton crater at the lunar south pole, *Nature*, *486*(7403), 378–381

and

Kreslavsky, M. A., J. W. Head, G. A. Neumann, M. A. Rosenburg, O. Aharonson, D. E. Smith, and M. T. Zuber (2013), Lunar topographic roughness maps from Lunar Orbiter Laser Altimeter (LOLA) data: Scale dependence and correlation with geologic features and units, *Icarus*, *226*(1), 52–66

3.1 Introduction

Surface roughness maps are valuable tools for geologic mapping and interpretation because they provide a means of analyzing large-scale variations in the typical character of textures at smaller scales. Identification of these variations can aid in defining geologic units, determining their relative ages, and characterizing the dominant surface processes acting at different scales to produce and modify topography. Moreover, roughness calculations derived from spacecraft observations, like those computed with topography data from the Lunar Orbiter Laser Altimeter (LOLA) carried on the Lunar Reconnaissance Orbiter (LRO) (*Smith et al.*, 2010a), rely on differences between successive elevation measurements, thus exploiting the exceptional precision in ranging along each orbit, which is much higher than the precision in overall orbit determination (*Smith et al.*, 2010b; *Kreslavsky et al.*, 2013). By utilizing this high internal precision, roughness calculations therefore maximize the differential topographic information returned.

As discussed in the previous chapter, roughness can be defined in many different ways, and several roughness parameters are typically employed for different purposes. This profusion of definitions led *Kreslavsky et al.* (2013) to describe six key qualities that roughness parameters must be assessed on for use in geological interpretation: 1) intuitive character; 2) independence with respect to regional tilts; 3) ability to capture typical surface textures; 4) specificity of scale; 5) statistical stability; and 6) tolerance of individual peculiarities within the dataset used (*Kreslavsky et al.*, 2013). These requirements are often in conflict, and no roughness parameter is ideal in all aspects. For example, the RMS slope (defined in Eq. 2.1) is often reported because it can be related to measurements of radar reflection scatter, and it is also an intuitive measure of surface roughness, satisfying requirement (1). However, because the RMS slope is sensitive to even a small proportion of steep slopes, and because topographic surfaces tend to have slope-frequency distributions with heavy tails, this parameter fails criteria (3) and (5).

For purposes of discrimination among geologic units, the median differential slope described in the previous chapter and *Rosenburg et al.* (2011) satisfies many of the key criteria and possesses several useful characteristics. Defined in Equation 2.3, the differential slope isolates features on a given scale of interest, L, by subtracting the slope at twice this scale, $2L$. It is thus unaffected by larger-scale, regional tilts (criterion 2) and describes a well-defined, specific scale (criterion 4), allowing for detailed examination of scale dependence in surface roughness. Reporting the median differential slope within each sliding window along a LOLA track guarantees that the roughness values reported are typical of the region and not overly influenced by a few unusually high values (criterion 3). While this parameter satisfies these criteria, there is a tradeoff with criterion (1). Because the reported values are slopes at a given scale measured with respect to slopes at twice that scale, differential slope is not as intuitive a measure of surface roughness as the RMS slope or RMS height. Nevertheless, it is useful for emphasizing roughness variations and distinguishing among geologic units.

Rosenburg et al. (2011) (see also Chapter 2) presented the first global roughness maps utilizing topography data from LOLA, introducing a variety of roughness parameters, including median slope, bidirectional slope, differential slope, and Hurst exponent (Chapter 2). *Kreslavsky et al.* (2013) extended this global analysis, using a related roughness parameter, the topographic curvature, at hectometer and kilometer scales. These studies investigate the scale dependence of surface slopes and provide a global context for regional roughness variations, to which more detailed surveys of local roughness can be referenced. This chapter focuses on two such investigations, using the full range of data collected during LRO's nominal and science mission phases. First, the lunar south pole is examined in detail, with particular attention to Shackleton crater and the progression of roughness signatures among craters and basins of increasing size, from simple craters to ringed basins. Second, the analysis of roughness on mare surfaces in Chapter 2 is extended to examine the relationship between scale-dependent roughness and surface age.

3.2 Lunar South Pole

During the mapping and science phases of the mission, which extended from September, 2010, through December, 2013, LRO traveled in a consistent 50-km polar orbit, a geometry that resulted in a confluence of tracks over the north and south poles. The high density of measurements available in these regions allows for a much greater resolution in gridded data (*Zuber et al.*, 2012a), as well as a higher density of along-track roughness calculations than is globally available. Figure 3.1 contains a color composite map of the median differential slope extending from 60°S to the south pole, showing roughness at three different scales, consistent with the global maps shown above in Figure 2.5. The smallest scale for slope calculations accessible to LOLA is equivalent to the shot spacing, approximately 57 m. Slopes at this scale and twice this scale ($\sim$ 110 m) were computed and binned in 1/64° ($\sim$ 480 m) overlapping windows along each orbit track, and the windows were spaced 1/128° ($\sim$ 240 m) apart. After aligning the resulting slope profiles, the values were subtracted and the median differential slope for each window was reported at the midpoint. This process was repeated for slopes at many other scales, three of which were combined to produce the composite image shown in Figure 3.1. Small-scale slopes ($\sim$ 57 m) are shown in the blue channel, intermediate scales ($\sim$ 220 m) in green, and larger scales ($\sim$ 560 m) in red. The pixel resolution is 1/64°, or

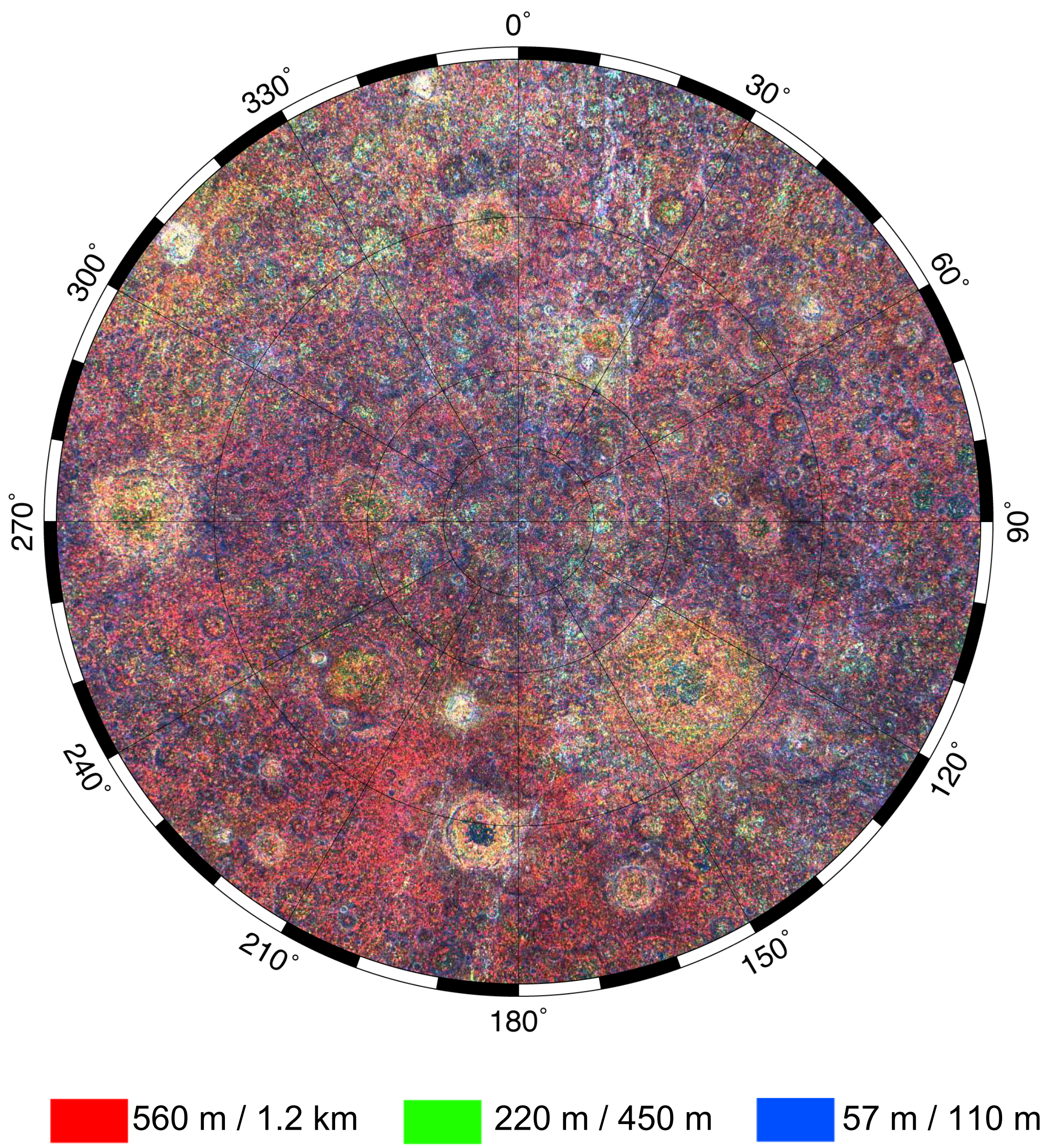

Figure 3.1: Median differential slope map of the lunar south pole from 60°S, showing differential slopes at three scales in the three color channels as in Figure 2.5. The blue channel corresponds to differential slopes at ~ 57 m, green corresponds to ~ 220 m, and red ~ 560 m.

approximately 0.48 km.

This map represents a significant improvement in resolution compared to Figure 2.5, made possible in part by the inclusion of more LOLA tracks, but also by the confluence of tracks over the poles due to orbit geometry. Several observations made in the previous chapter on global roughness are also apparent here. For example, the brightest features are young, Copernican-age craters which appear white in the composite image because they are rough at every scale included. Prominent features include the craters De Forest (77.3°S, 162.1°W), Zucchius (64.1°S, 50.3°W), and Rutherford (60.9°S, 12.1°W), all of which have associated ray systems that appear as star-shaped enhancements in intermediate scales (green shades) outside the crater rims. Several very long, bright, linear features are also visible extending from lower latitudes and crossing near the pole. One pair of these features is associated with the crater Tycho (43.3°S, 11.4°W), which is thought to be the youngest feature of its size on the lunar surface (*Kreslavsky et al.*, 2013). The rays are not always associated with distinct topographical relief, but nevertheless contain a unique signature in the differential slope map. They deviate very little from great circles and are brightest on the near side, closest to Tycho. As noted by *Kreslavsky et al.* (2013), these rays are composed of regions of relatively smoother and rougher segments, the latter corresponding to clusters of secondary craters.

3.2.1 Large Craters and Basins

Aside from the bright young craters and the long linear rays, the most noticeable features in Figure 3.1 are the large craters and basins that range in size from ~ 50 to ~ 300 km in the case of Schrödinger (75°S, 134.4°E). At the scales included in this differential slope map, craters in this range of diameters are characterized by a distinctive set of features which follow the progression of crater morphology from large complex craters with central peaks to multi-ring basins. Lyman (64.8°S, 163.6°E) is a $D = 84$ km crater that has undergone relatively little erosion by subsequent impacts. Figure 3.2 shows a portion of the Lunar Reconnaissance Orbiter Camera (LROC) Wide Angle Camera (WAC) Mosaic centered on the crater, with an inset showing the corresponding portion of the differential slope map shown in Figure 3.1. The roughly circular rim crest is visible as

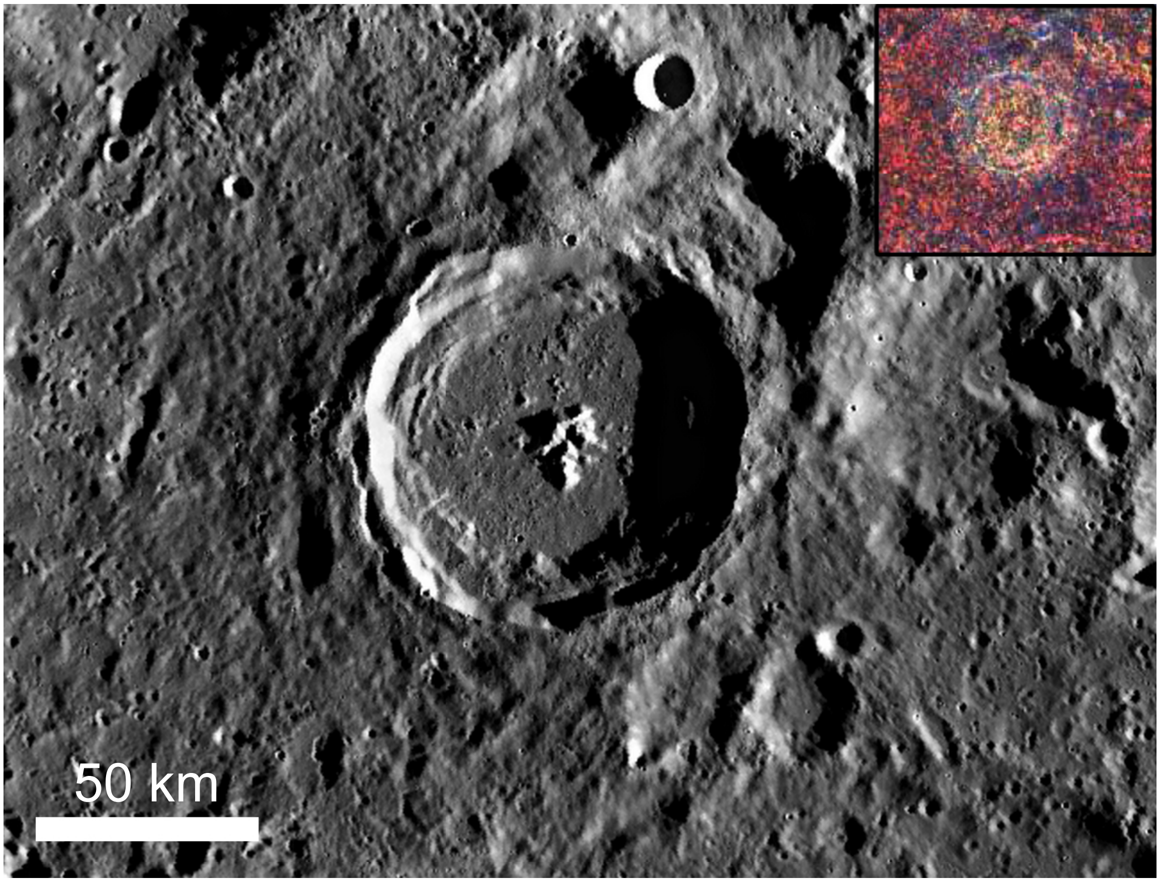

Figure 3.2: Lyman crater (74.2°S, 90.8°E) shown in the LROC WAC mosaic in a south polar stereographic projection. The inset shows the corresponding portion of the median differential slope map shown in Figure 3.1.

a bright white ring that is largely uninterrupted around the crater perimeter, indicating that the sharp relief at the rim crest is registered in slopes at the scales represented by all channels. Just inside the rim, a dark blue ring defines the steep inner walls, which are quite smooth at all scales; only the smallest scale (~ 57 m) shows any signal at all, consistent with the effects of mass wasting observed both within and without the crater rim. The slumped material forms a ring on the crater floor that appears with a red hue in the differential slope map, reflecting its hummocky character on kilometer scales. The prominent central peak formation appears with a similar hue, while the remainder of the crater floor is roughest at intermediate scales, resulting in a somewhat yellower appearance mottled with darker regions of relatively smooth terrain.

This bullseye pattern of concentric rings corresponding to the morphologic features is found in many other complex craters shown in Figure 3.1 with some important variations. For example, Hale

(74.2°S, 90.8°E) is a relatively young impact crater of nearly the same size as Lyman ($D = 83$ km), containing few superposed craters, but its multiply terraced rim is expressed as a wide annulus of enhanced roughness at the largest scale (~ 560 m), rather than a continuous bright ring. The floor of Hale is also somewhat smoother than that of Lyman, appearing as a dark blue ring surrounding the central peak complex, which is offset from the center toward the south. The slightly larger crater Demonax ($D = 114$ km, 78.2°S, 59.0°E) is much more heavily eroded, and its smoother walls form a wide dark annulus around the bright crater floor, which is relatively level and contains both hummocky, mass-wasted material (red, roughest at the 560-m scale) and flat terrain punctuated by kilometer-scale craters (yellow, roughest at the 220-m scale). These variations in roughness signature among complex craters of similar size thus provide useful markers for identifying crater age and degree of degradation. This is an important feature, especially at the lunar poles, where illumination conditions are highly variable and regions of permanent shadow persist in the floors of many circumpolar craters. Gridded digital elevation models from LOLA can be used to count craters in these regions, but roughness analysis like that presented here provides another means of assessing relative ages.

Antoniadi (69.7°S, 172.0°W) is a large peak ring crater ($D = 143$ km)— one of only a few features possessing both a central peak and a surrounding inner ring (*Wilhelms et al.*, 1987), a transitional morphology between complex craters and ringed basins that is not well understood. Located within the South Pole-Aitken Basin, Antoniadi also happens to contain the lowest elevation on the Moon (*Smith et al.*, 2010b). Like its smaller counterparts, this crater has a sharp rim crest defined by a bright white ring, although in this case the ring is not continuous. The steep inner walls form a dark blue ring, part of which corresponds to the brightly illuminated north wall in the LROC WAC Mosaic shown in Figure 3.3. The region between the walls and the inner ring is rough at the ~ 220-m scale, while the chain of mountain segments making up the ring itself is distinguishable as a somewhat redder annulus, reflecting the change in texture. Likewise, the central peak and other isolated massifs visible inside the inner ring are rough only at the largest scale, ~ 560m.

The interior of the inner ring is covered with a young mare deposit (*Wilhelms et al.*, 1979),

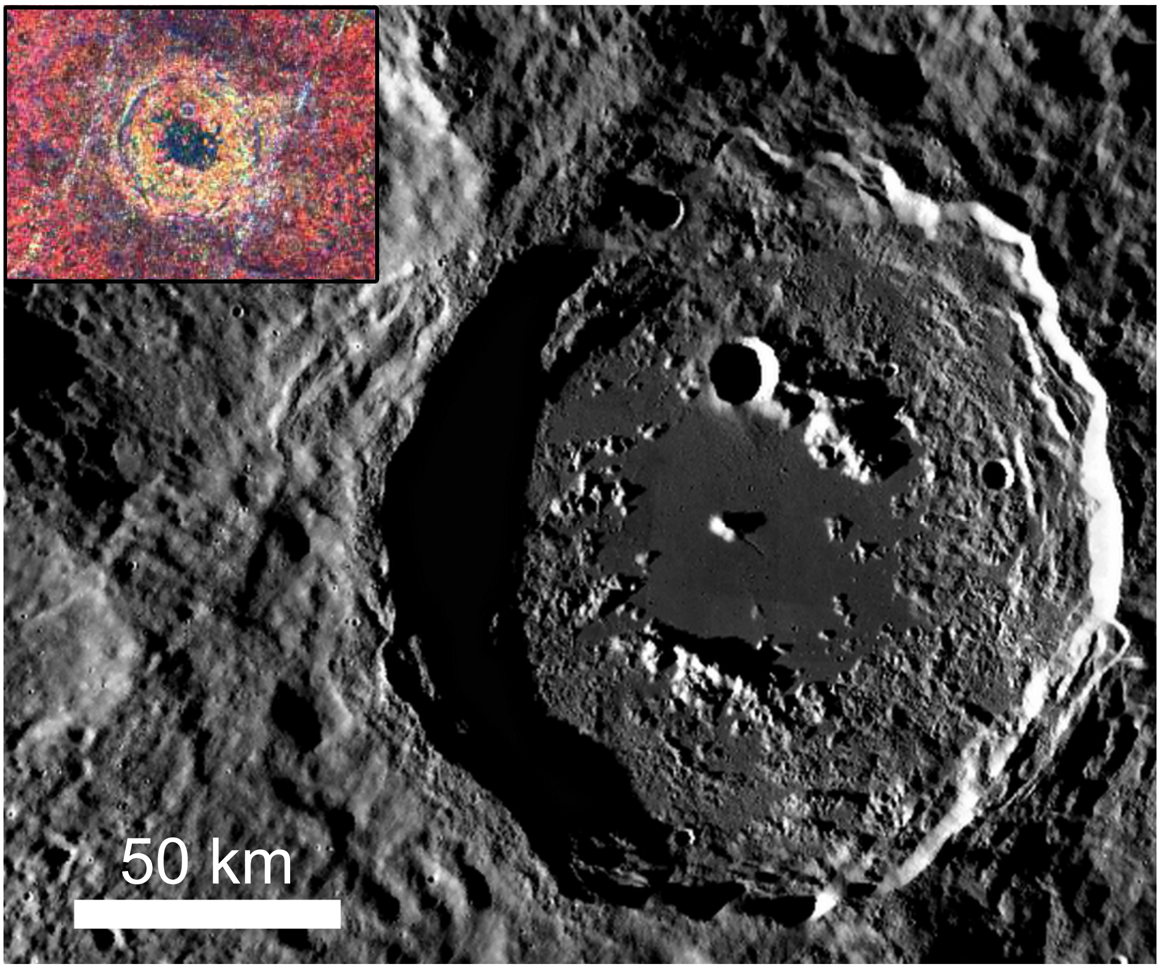

Figure 3.3: Antoniadi crater (69.7°S, 172.0°W) shown in the LROC WAC mosaic in a south polar stereographic projection. The inset shows the corresponding portion of the median differential slope map shown in Figure 3.1.

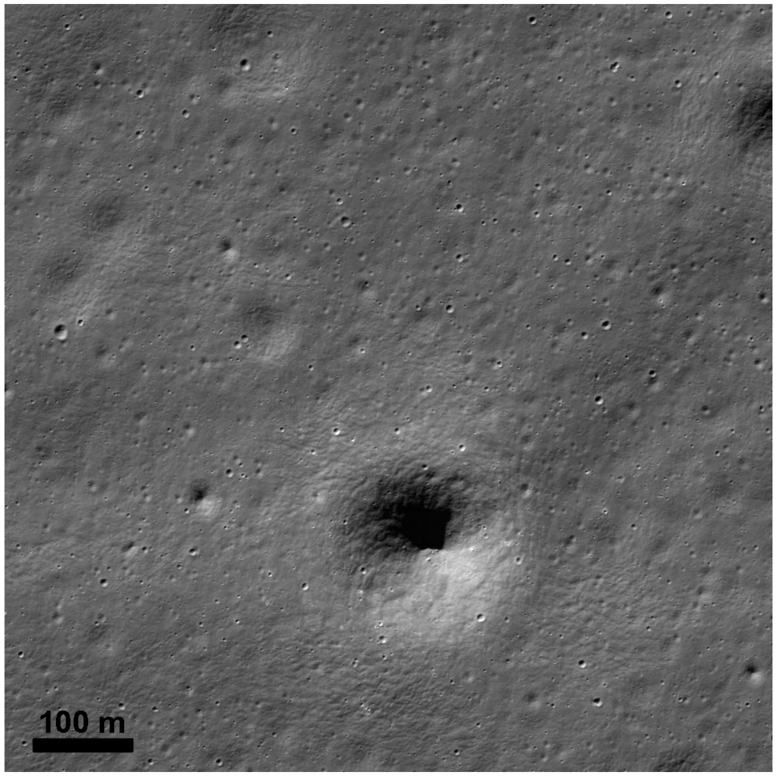

Figure 3.4: Mare deposits on the floor of Antoniadi, shown in a portion of LROC NAC image M1130635802R.

and its roughness signature is similar to those of comparably young mare-filled basins on the near side of the moon shown in Figure 2.5. This unit is relatively smooth at all scales shown in the composite image, with most signal present in the smallest LOLA scale, ~ 57 m. Figure 3.4 shows the floor of Antoniadi within the inner ring from a portion of the LROC Narrow Angle Camera (NAC) image M1130635802R. The mare surface is covered with small craters down to sizes below the image resolution (~ 1 m/pix). Some craters appear relatively pristine, but many others, like the largest feature shown ($D \sim 180$ m), have been smoothed by the diffusive action of regolith gardening (see Chapter 4). Craters like this one contribute to the differential slope at the ~ 57-m scale, but appear smooth at larger scales, as shown in Figure 3.3.

Aside from the South Pole-Aitken Basin, Schrödinger (75.0°S, 132.4°E) is the largest basin poleward of 60°S (Figure 3.1), with $D = 312$ km. The basin and the corresponding section of the differential slope map are shown in Figure 3.5. As with Antoniadi and Lyman, distinct roughness zones can be identified that correspond to morphologic features of the basin. Schrödinger's rim is a

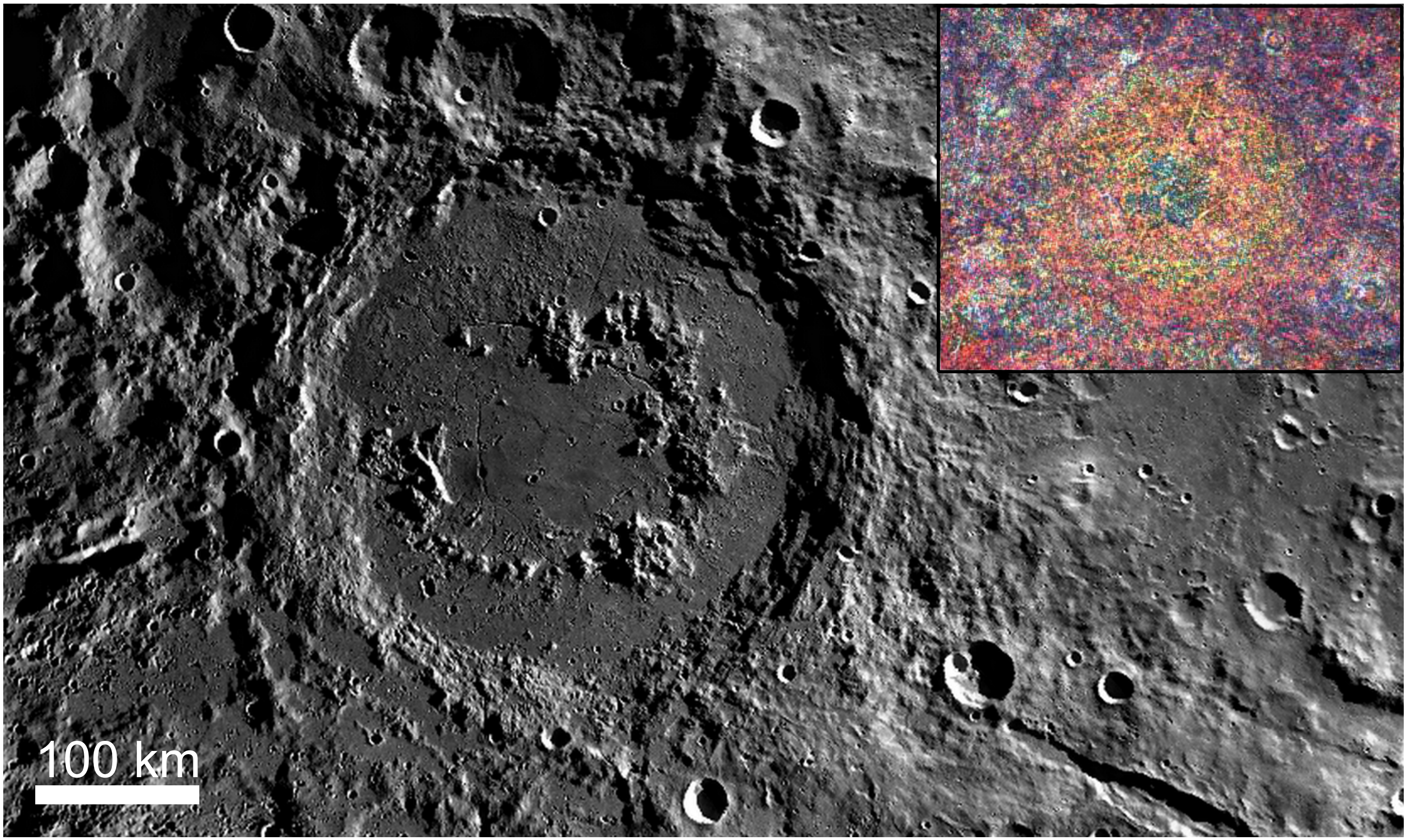

Figure 3.5: Schrödinger basin (75.0°S, 132.4°E) shown in the LROC WAC mosaic in a south polar stereographic projection. The inset shows the corresponding portion of the median differential slope map shown in Figure 3.1.

broad, terraced annulus that is roughest at the largest scale included in the composite image, ~ 560 m. The inner ring, which occurs at about half the crater diameter, has a similar hue, reflecting the kilometer-scale roughness of the rugged chain of mountain segments. Between the walls and the inner ring, the floor is relatively bright and roughest at intermediate scales (~ 220 m), appearing yellow. Within the inner ring, where the surface has been reworked by lava flows and impact gardening, the shortest scale dominates and the area appears blue in the composite map, much brighter (rougher) than Antoniadi's mare-filled interior. Several distinctive tectonic features are easily seen in the roughness map, including many of the radial and concentric fractures that traverse the crater floor, sometimes crossing the peak ring (*Mest*, 2011).

Several smaller craters ($D < 50$ km) with characteristic roughness signatures are visible in Figure 3.5 outside the rim of Schrödinger. The rough rim crest appears as a bright white ring, within which the steep crater walls appear dark blue. The center of each crater is distinctively rough at larger scales ($\sim 220-560$ m), appearing orange in the color composite image. This particular pattern of concentric roughness zones characterizes many craters in this size range throughout Figure 3.1, including Shackleton crater, a feature of great interest because of its location so near to the south pole and, consequently, the unique illumination conditions.

3.2.2 Shackleton Crater

Shackleton crater, nearly centered at the lunar south pole (89.9°S, 0°E), is a relatively fresh 21-km crater. The floor is almost entirely in permanent shadow, while the walls receive continuous sunlight, due to the Moon's low inclination, and, as a result, the floor of the crater is a perennial cold trap (*Watson et al.*, 1961; *Arnold*, 1979). However, whether lunar volatiles are present within the crater or other permanently shadowed regions (PSRs) remains an open question, as previous orbital and Earth-based radar mapping and imaging missions have returned conflicting results (*Nozette et al.*, 1996; *Stacy et al.*, 1997; *Campbell et al.*, 2006; *Simpson and Tyler*, 1999; *Nozette et al.*, 2001). LOLA illuminates the surface at a wavelength of 1064 nm, allowing for brightness measurements of PSRs at that wavelength in the absence of sunlight. *Zuber et al.* (2012a) found that the walls of Shackleton

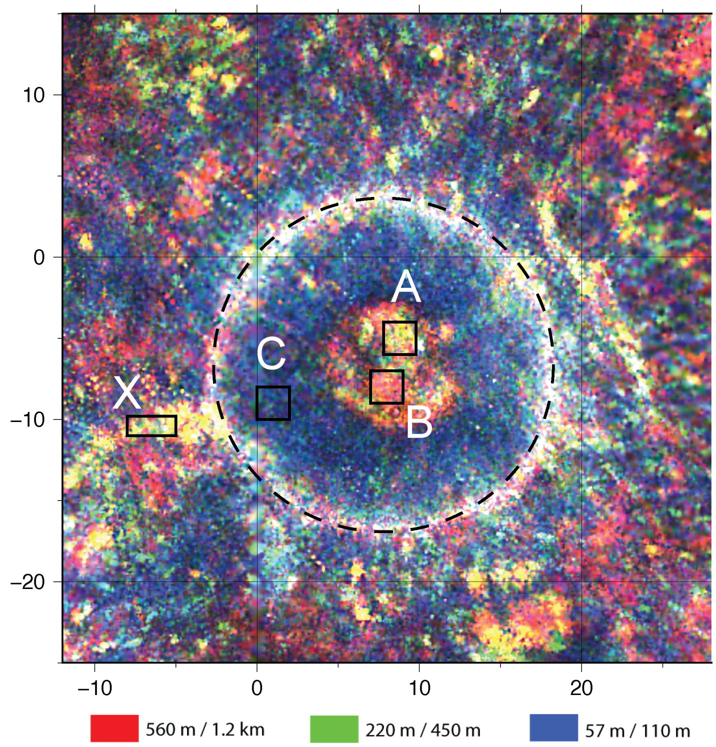

Figure 3.6: Color composite image showing differential slope at three scales: 560 m (10 LOLA shot spacings) in the red channel, 220 m (4 shot spacings) in green, and 57 m (1 shot spacing) in blue. The median differential slope at each scale is reported for overlapping windows of width 1/64° (∼ 480 m), spaced 1/128° (∼ 240 m) apart. Boxes represent regions sampled to create Figure 3.7, and the location of the rim crest is shown as a dashed black line. Several distinct roughness units are apparent within Shackleton Crater. The crater walls, which are smooth at large scales, retain roughness only at the smallest scales, causing them to appear dark blue. The crater floor, which contains a hummocky mound unit that is smooth at all scales but roughest at large scales, thus appearing red in the image, and a flat region, which is roughest at intermediate and large scales, thus appearing yellow. Outside the rim, secondary crater fields identified in *Zuber et al.* (2012a) (Figure 1e) appear as yellow streaks due to their unique contribution to the topography at intermediate and large scales.

crater are anomalously bright, and the crater floor, while darker than the walls, is brighter than the surrounding terrain. These observations are consistent with downslope movement of regolith, exposing fresher material in the crater walls, and decreased space weathering on the crater floor due to shadowing. The brightness of the floor at 1064 nm could also be explained by a 1-mm-thick layer of regolith containing $\sim 20\%$ water ice (*Zuber et al.*, 2012a).

A detailed examination of surface roughness in the vicinity of Shackleton crater reveals several distinct roughness units. Figure 3.6 is a color composite image showing the median differential slope at three baselines, as in Figure 3.1: ~ 57 meters in the blue channel, ~ 220 meters in green, and ~ 560 meters in red. The boxes mark sampled regions within each roughness unit, and differential slopes are shown in Figure 3.7 for a variety of scales. The walls of the crater (Fig. 3.6, C) are smooth at the large and intermediate scale, retaining roughness only at the shortest scale and thus appearing blue in the image. The floor can be divided into two regions, a flat portion (Fig. 3.6, A) and an elevated terrain possibly related to mass wasting at the crater walls (Fig. 3.6, B). The roughness of this mound unit increases at the largest scales due to its hummocky character, but it is smoother than the flat region at all scales < 850 m, due to its paucity of craters. In fact, at the shortest scales the mound is the smoothest of the representative regions shown. The flat floor has a higher crater age and appears yellow due to the addition of slopes on the intermediate scale, while the rim itself, the crest of which is marked by a dashed black line in Figure 3.6, is rough at all scales, appearing white. Areas of suspected secondaries (Fig. 3.6, X) are clearly defined in the roughness map as yellow streaks, owing to high slopes at the largest and intermediate scales and little roughness at the smallest scale. The distinct character of these roughness units and their correlation with mapped geologic units using gridded topography data illustrates the usefulness of roughness maps for clarifying relationships between superposed units. For example, secondary craters are often difficult to distinguish from primary craters of similar diameters in visual imagery. However, because they are often formed at lower velocities than primary craters, they tend to have different morphologies and depth-to-diameter scaling relationships. As Figure 3.6 shows, they contribute a unique signature to the topographic roughness that can aid in their identification and mapping.

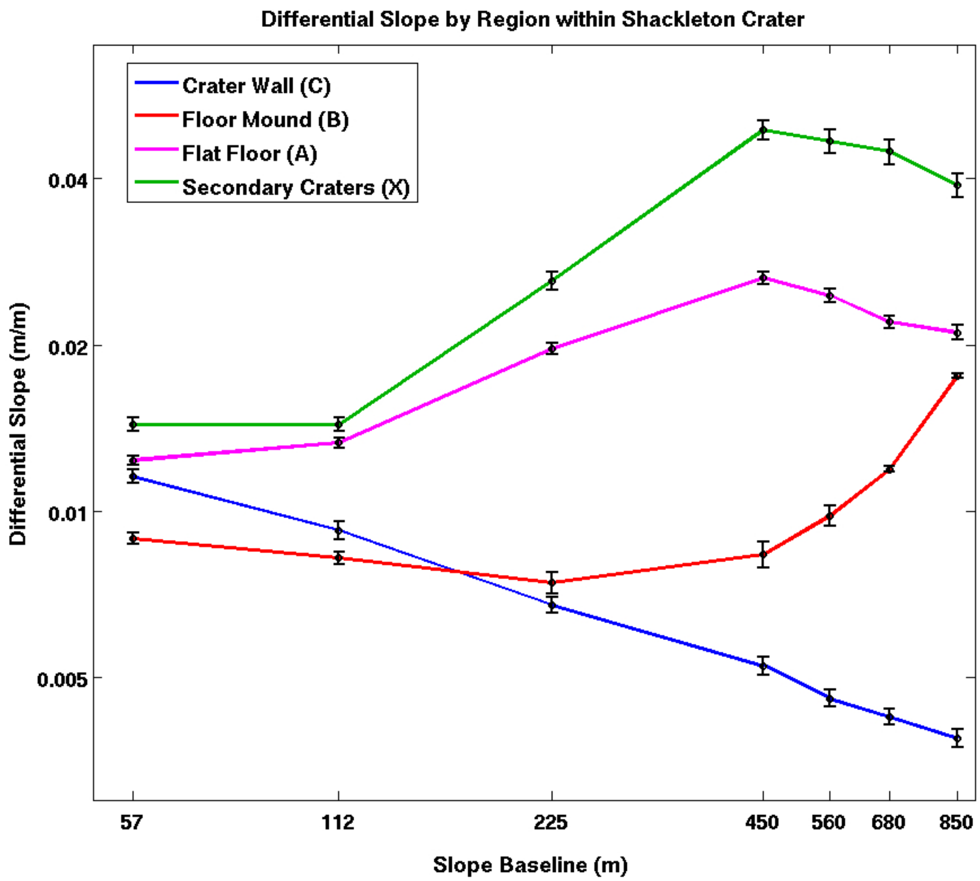

Figure 3.7: Differential slope for several baselines corresponding to 1, 2, 4, 8, 10, 12, and 15 LOLA shot spacings, showing roughness variation with scale for several distinct roughness units related to Shackleton crater. The region sampled for each roughness unit is marked by a box in Figure 3.6. Labels correspond to the regions mapped for crater counting in *Zuber et al.* (2012a) (Figure 1e). The crater wall (Fig. 3.6, C) is smooth at large scales and retains roughness only at the smallest scale, while the hummocky terrain on the crater floor (Fig. 3.6, B) is smooth at small and intermediate scales, becoming rougher at large scales. The flat part of the crater floor (Fig. 3.6, A) is roughest at intermediate scales, similar to the clusters of suspected secondary craters (Fig. 3.6, X). Standard 2σ error bars represent the spread of the distribution of median differential slopes within each sampled region and for each baseline considered.

3.3 Roughness of Mare Surfaces

As discussed above, the median differential slope is a powerful tool for discriminating between roughness units. It can also help us to understand the evolution of roughness on surfaces of varying age, particularly in the lunar maria. *Farr* (1992) explored the development of surface roughness at centimeter- to meter-scales on progressively older terrestrial lava flows, showing that particular features in the topographic power spectrum could be correlated with specific geologic processes occurring on these surfaces, such as aeolian deposition and fluvial dissection. On the Moon, the major roughening agent at every scale is the accumulation of impact craters. The power law exponent of the observed cumulative size-frequency distributions in the maria is negative for sub-kilometer craters, at approximately -4 (*Melosh*, 1989; *Neukum et al.*, 2001), indicating that small craters are much more numerous than large ones. Thus, resurfaced areas collect small craters first and accumulate successively larger ones over time. Roughness on surfaces of varying age is expected to reflect this sequence, the younger surfaces remaining smoother at larger scales. Older surfaces, which have had time to collect craters over a greater range of diameters, are expected to have significant roughness components at intermediate and larger scales.

In Figures 2.5 and 3.1, mare deposits generally appear dark blue because they are relatively smooth, and what roughness does exist occurs at the smallest scale studied ($\sim$ 57 m), which is shown in the blue channel of the composite images. However, variations in hue are apparent between different mare regions. Comparing the differential slope at many different scales ranging from $\sim$ 57 m to $\sim$ 1.4 km, we find a trend that corresponds to the reported ages of various mare units, as estimated by *Hiesinger et al.* (2010) from detailed crater counts. Figure 3.8 contains a context map in which the outline of the mare deposits (*Wilhelms et al.*, 1971, 1977; *Scott and McCauley*, 1977; *Lucchitta and Center*, 1978; *Stuart-Alexander and Center*, 1978; *Wilhelms et al.*, 1979) are overlain on the elevation map, and sampled regions are marked by lettered boxes. Figure 3.9 shows the differential slope at several baselines for the regions sampled, which range from the oldest dated flows in Mare Marginis and Mare Tranquilitatis ($>$ 3.6 Ga) to flows of intermediate age in Mare Humorum ($\sim$ 3.3 Ga) and Mare Imbrium ($\sim$ 2.7 Ga), to the youngest dated unit in Oceanus Procellarum ($<$ 2.5 Ga)

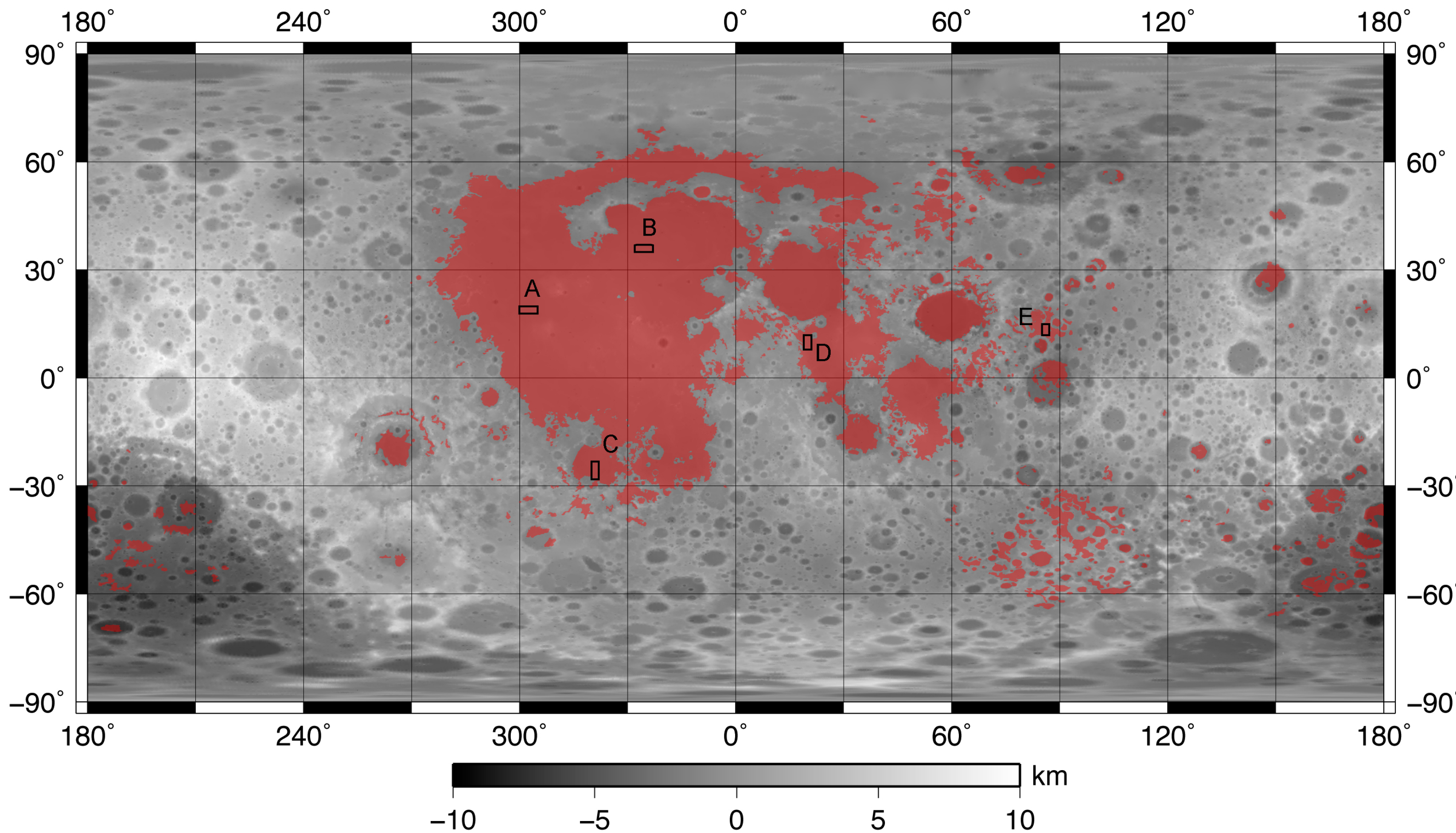

Figure 3.8: Context map for sampled regions within the lunar maria, showing the outline of mare deposits (*Wilhelms et al.*, 1971, 1977; *Scott and McCauley*, 1977; *Lucchitta and Center*, 1978; *Stuart-Alexander and Center*, 1978; *Wilhelms et al.*, 1979) overlain on the lunar topography in a simple cylindrical projection.

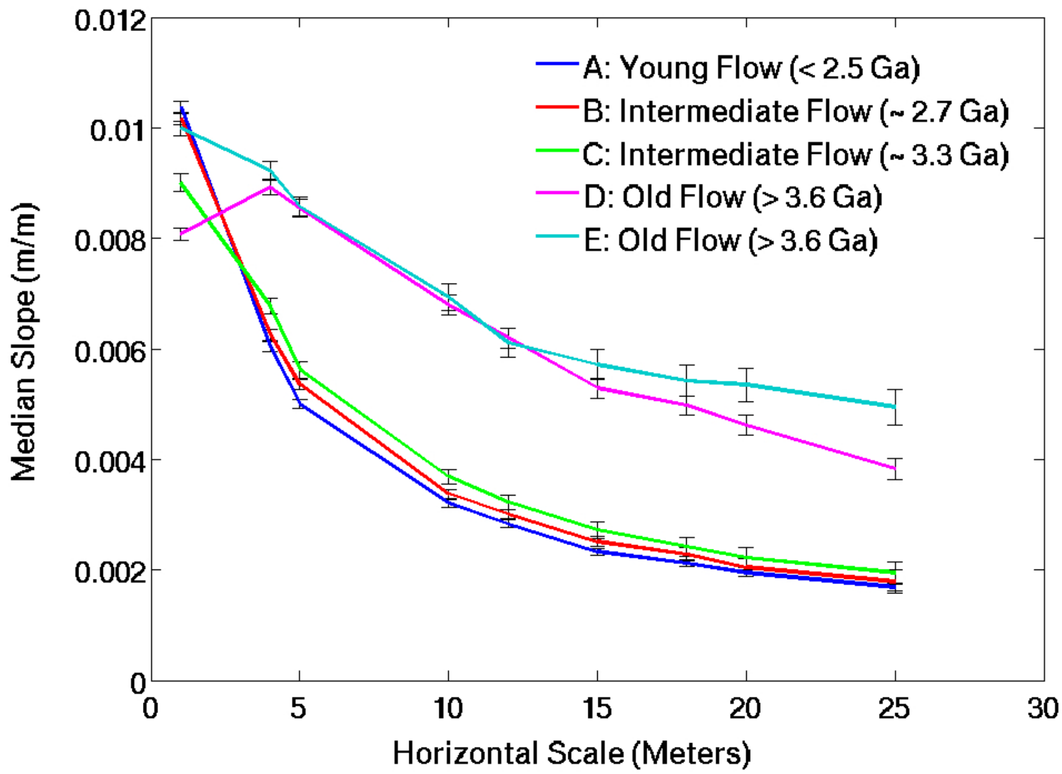

Figure 3.9: Comparison of differential slopes at many baselines within the sampled regions of the lunar maria. Standard 2σ error bars represent the spread of the distribution of median differential slopes within each sampled region and for each baseline considered.

(*Hiesinger et al.*, 2010). Letters in the legend correspond to the boxes in the context map (Fig. 3.8).

The youngest mare units, within Oceanus Procellarum and Mare Imbrium, are rough only at the smallest scales, while successively older flows (e.g., those within Mare Tranquilitatis and Mare Marginis) contain significant roughness components at longer baselines. At the smallest scale, median differential slope remains roughly constant among all sampled regions, suggesting that perhaps crater saturation at small ($D < 100$ m) scales occurs relatively swiftly. This observation is consistent with *Kreslavsky et al.* (2013) and *Rosenburg et al.* (2011), who note that at hectometer scales, roughness is approximately constant on global scales, both on maria and highlands terrain. Differential slopes at larger baselines vary systematically with the age of the surface considered, although, as *Kreslavsky et al.* (2013) point out, the roughness of mare surfaces is not a function of age alone, and specific regions of young terrain can be found that are rougher than older mare surfaces.

3.4 Summary

Roughness maps provide a means of analyzing large-scale variations in typical surface texture at a range of finer scales. As such, they are useful tools for geologic mapping and interpretation, with specific application to the identification of geologic units, assessment of relative ages, and characterization of the effects of competing surface processes acting at different scales. Detailed studies of local regions, like those discussed above for the lunar south pole, Shackleton crater, and mare surfaces of varying age, extend and focus the analysis initiated in the global roughness maps of *Rosenburg et al.* (2011) (Chapter 2) and *Kreslavsky et al.* (2013).

Focusing on the lunar south pole, where the confluence of LOLA tracks results in a high density of elevation measurements conducive to detailed study using differential slopes, we find that many features express unique roughness signatures, including rough, Copernican-age craters and their associated ray systems. Aside from a slight enhancement at the $\sim$ 560-m scale, South Pole-Aitken basin, the largest and oldest basin on the Moon, is poorly defined in the differential slope map shown in Figure 3.1, despite its obvious expression in the topography (*Garrick-Bethell and Zuber*, 2009). Complex craters and basins ranging from $D \sim 50$ to ~ 300 km exhibit a typical sequence of approximately concentric roughness zones: a bright white (rough at every scale) ring corresponding to the rim crest, a dark blue (smooth at all scales) annulus corresponding to the steep inner walls, and discontinuous arcs that appear red (rough at the $\sim$ 560-m scale) in the composite color maps (Fig. 3.1), which correspond to hummocky, slumped material from the crater walls, segments of the peak-crater ring, and the central peak formations. Where the interiors of large basins have been filled and reworked by volcanic flows, as in Antoniadi and Schrödinger, the topography is smoother than the rest of the crater floor, rough only at the smallest scale considered, $\sim$ 57 m. Small craters ($D < 50$ km) also exhibit many of these key features, notably the rough rim crest and steep inner walls. The consistency of these roughness units across crater diameters reflects the underlying consistency in the scale of crater modification processes such as mass wasting and impact gardening.

Shackleton crater, of interest for its unique illumination conditions, possesses several distinct roughness units that correlate well with geologic units mapped using the elevation data. Brightness measurements at the 1064-nm scale of the LOLA laser are consistent with the downslope movement of material on the steep crater walls, exposing fresher, brighter material underneath, while the relatively bright crater floor can be explained either by decreased space weathering in the shadowed crater interior or a thin surface layer of material containing a significant fraction of water ice (*Zuber et al.*, 2012a). The dark blue appearance of the crater walls and the red hue of the mound unit (interpreted as a potential slump deposit) in Figure 3.6 supports the mass wasting hypothesis suggested by the brightness measurements. Regions of suspected secondary craters also are shown to have a distinct roughness signature in the differential slope map at these baselines, demonstrating the utility of roughness measures in distinguishing between primary and secondary craters.

Finally, the evolution of roughness on mare surfaces of varying age is examined using differential slopes at several different baselines within several mare units whose ages have been determined via crater counts by *Hiesinger et al.* (2010). We find that roughness at the shortest scale accessible with LOLA, ~ 57 m, is approximately constant across all sampled regions, suggesting that crater saturation at small scales ($D < 100$ m) has occurred. At larger scales, older mare units are rougher than their younger counterparts, having had more time to collect craters within a broader range of diameters.

Chapter 4

Power Spectral Density of Cratered Terrains

Abstract

Impact cratering produces characteristic variations in the topographic power spectral density (PSD) of heavily cratered terrains, which are controlled by the size-frequency distribution of craters on the surface and the spectral content (shape) of individual features. These variations are investigated in two parallel approaches. First, a cratered terrain model, based on Monte Carlo emplacement of crater features and benchmarked by an analytical formulation of the one-dimensional PSD, is employed to generate topographic surfaces at a range of size-frequency power law exponents and shape dependencies. For self-similar craters, the slope of the PSD, β, varies inversely with that of the production function, α, leveling off to 0 at very high α (surface topography dominated by the smallest craters) and maintaining a roughly constant value ($\beta \sim 2$) at very low α (surface topography dominated by the largest craters). The effects of size-dependent shape parameters and various crater emplacement algorithms are also considered. Second, we compare the model-derived predictions for the behavior of the PSD with values of β calculated along transects from the Lunar Orbiter Laser Altimeter (LOLA). At small scales ($\sim$115 m to 1 km) the PSD slope agrees reasonably well with the model predictions for the observed range of lunar size-frequency distributions. Differences between global PSD slopes at sub-kilometer and kilometer scales reflect the scale separation in roughness noted by *Rosenburg et al.* (2011) and *Kreslavsky et al.* (2013) using different but related surface

roughness parameters. Understanding the statistical markers left by the impact cratering process on the lunar surface is useful for distinguishing between competing geological processes on planetary surfaces throughout the solar system.

4.1 Introduction

The high resolution of the topography dataset recently recorded by the Lunar Laser Orbiter Altimeter (LOLA), together with ongoing improvements in computing power, provides unprecedented opportunities to correlate model results with observed lunar features. Nowhere is this more pertinent than in impact crater studies. The evolution of cratered terrains is not well understood, despite decades of study (*Melosh*, 1989; *Richardson et al.*, 2005; *Richardson*, 2009), but our understanding of it is crucial to our knowledge of planetary bodies, especially those for which non-photographic data are scarce, such as the outer planet satellites. Numerical cratering models have seen vast improvements in spatial resolution over the past two decades (*Richardson*, 2009; *Howard*, 2007), and are now capable of tackling a range of crater scales broad enough to allow comparison with real cratered terrains. At the same time, renewed efforts to map the Moon down to meter scales have been stimulated by the abundance of high-resolution images returned by the Lunar Reconnaissance Orbiter Camera (LROC), including recent citizen scientist projects to count craters and evaluate counting statistics (*Robbins et al.*, 2014).

A quantitative comparison of cratered terrain model results and lunar topography analysis thus has never been more feasible, on hand, and relevant to further our understanding of lunar surface processes. To this end, we have developed a cratered terrain model that generates surfaces saturated with craters, and have used it to investigate the statistical properties of such landscapes and how they depend on factors such as the size-frequency distribution of impactors, crater shape, and competing surface processes. By keeping track of both topography and remaining rim fractions of emplaced craters (via a rim-tracking algorithm) the model allows us to evaluate the power spectral density (PSD) and size-frequency distribution of visible craters before and after the surface has attained equilibrium. Finally, comparing our results to the lunar topography, in both highland and mare regions, can help to distinguish among markers of competing geomorphologic processes acting on the lunar surface.

4.2 Models

Any impact cratering model necessarily simplifies a set of complex, local, and interdependent processes, many of which remain active areas of research in their own right. Depending on the task at hand, different researchers have chosen to model different aspects of the cratering process, from a highly detailed slope-failure and regolith-tracking approach (*Richardson*, 2009) to a landscape generator used to study aeolian and fluvial systems on Mars (*Howard*, 2007). Whatever the goal, two primary phases of crater emplacement must be observed: 1) some degree of erasure, or resetting, of the initial topography, and 2) superposition of the crater shape. Here, we study the characteristic statistical properties of cratered terrains in order to more easily identify and disentangle signatures of competing geomorphologic processes on planetary surfaces. Modeling is divided into three phases. First, we develop a 1-dimensional Monte Carlo simulation that emplaces craters on a flat domain with periodic boundary conditions. Resetting is accomplished through a simple rule: once the location for a new crater has been selected, the existing topography is surveyed and the area within the crater rim is reset to its own mean. In the second modeling phase, we use an analytic formulation to benchmark the 1D numerical model for terrains accumulating craters of a single size. We then develop a procedure for combining craters of different sizes according to a given size-frequency distribution. The resulting synthetic power spectral density can be directly compared to that generated using the 1D emplacement model. Using the numerical and analytic models together, we can thus understand the evolution of 1D cratered terrains, starting from a flat plane and proceeding to equilibrium. Finally, we move to a two-dimensional domain and compute the power spectral density along 1D transects to allow for direct comparison to the LOLA topography dataset.

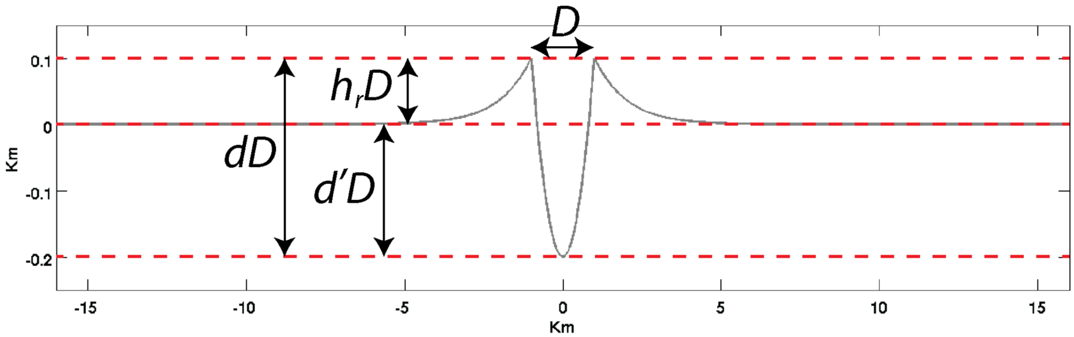

Figure 4.1: Crater shape parameters used in the numerical and analytic models. The measurable quantity (rim-to-floor) depth-to-diameter ratio (d) is given by $d = d' + h_{\rm r}$, the depth below the surrounding terrain and the rim height, respectively (both normalized by diameter). The exponential shape of the ejecta blanket is controlled by the ejecta falloff exponent, γ.

4.2.1 1D Numerical Model

One-dimensional craters consisting of a cavity and an exponential ejecta blanket are accumulated on a flat domain of size X with periodic boundary conditions. Crater shape is parameterized by depth-to-diameter ratio, d (referring to the rim-to-floor depth), rim height-to-diameter ratio, $h_{\rm r}$, cavity shape exponent, m, and exponential ejecta falloff exponent, γ. For all 1D models, m is taken to be 2 (parabolic cavity shape), yielding the following crater shape equation:

$$h(x) = \begin{cases} (d' + h_{\rm r})D\left(\frac{2x}{D}\right)^2 - d'D & |x| \le \frac{D}{2} \\ h_{\rm r}De^{\gamma\left(1-\frac{2x}{D}\right)} & |x| > \frac{D}{2}, \end{cases} \tag{4.1}$$

where d is the depth below the surrounding terrain ($d' = d - h_{\rm r}$) normalized by the crater diameter (see Fig. 4.1). For 1D volume-conserving craters, the three parameters d, $h_{\rm r}$, and γ are not independent variables but are related by the expression:

$$\gamma = \frac{3h_{\rm r}}{2d' - h_{\rm r}}. \tag{4.2}$$

when $m = 2$ (*Garvin and Frawley*, 1998; *Heiken et al.*, 1991).

We first consider self-similar crater shapes, and subsequently introduce more realistic, size-dependent shape parameters. Crater diameters are chosen according to a specified size-frequency distribution characterized by the power law exponent α:

$$N_{\rm c} \propto cD^{-\alpha}, \tag{4.3}$$

where $N_{\rm c}$ is the cumulative size-frequency distribution (in units of number of craters per unit area), and c is a constant with units dependent on α.

Crater locations are selected at random, and the initially flat plane (or profile, in the 1D case) accumulates enough craters to completely cover the surface several times. Equilibrium, defined here as the point at which the PSD ceases to change with the addition of more craters, is achieved first at the highest frequency and evolves to lower frequency as larger craters are emplaced. Once equilibrium has been achieved for the scales corresponding to the frequency range of interest, the PSD is computed and averaged over time to provide the best estimate of the equilibrium power spectral density.

$$P(k) = \frac{1}{X}\left[\int_{-X/2}^{X/2} e^{-ikx} h(x)\mathrm{d}x\right]^2. \tag{4.4}$$

We use two methods to compute the PSD. First, we use Fast-Fourier Transform, from which the PSD can be directly computed from the square of the coefficients, as in Equation 4.4. Second, we employ a multi-taper method to estimate the power spectral density with several filters (implemented by MATLAB's function `pmtm`). This is a useful tool for analyzing non-periodic signals like the lunar topography data collected by LOLA. Both the direct (FFT) method and the multi-taper approach provide robust estimates of the PSD for our model, but only the latter is used in our comparison of the model results to the lunar data.

To a first approximation, craters of diameter D are topographic features with a characteristic height, $H(D)$. These features, placed at random, contribute to the overall topography in a manner similar to a random walk, in that they can add coherently or incoherently, and the elevations they build therefore increase roughly as the square root of the number emplaced. The exponential term of the Fourier integral (Eqn. 4.4) is approximately constant over a scale D, and the number of these craters contributing to the power is $f_D X/D$, where f_D is the fraction of the domain covered by craters of this size. Equation 4.4 can thus be rewritten as:

$$P(k) = \frac{1}{X}\left[\int_0^X e^{-ikx} h(x) \mathrm{d}x\right]^2 \sim \frac{1}{X}\left[H(D) D \sqrt{\frac{f_D X}{D}}\right]^2. \tag{4.5}$$

For our model craters, the amplitude H can be thought of as the rim-to-floor depth, $H = dD$. More rigorously, the equilibrium power spectral density of a surface saturated with craters of a single size D can be calculated analytically by considering the two phases of crater emplacement specified in the numerical model: 1) resetting of initial topography and 2) building of the crater shape. The latter procedure is straightforward, as the superposition of the crater shape on the newly reset topography translates to a linear addition of power in the frequency domain. The power spectral density of our crater shape function (Eqn. 4.1) can be written by evaluating Equation 4.1 with Equation 4.4:

$$P_{\mathrm{build}} = \frac{2}{X}\left[\frac{D}{2}\left(\frac{4h_{\mathrm{r}}}{k}\sin\frac{kD}{2} + \frac{16(d'+h_{\mathrm{r}})}{k^2 D}\cos\frac{kD}{2} - \frac{32(d'+h_{\mathrm{r}})}{k^3 D^2}\sin\frac{kD}{2}\right) + \frac{2h_{\mathrm{r}} D^2\left(2\gamma\cos\frac{kD}{2} - kD\sin\frac{kD}{2}\right)}{4\gamma^2 + (kD)^2}\right]^2. \tag{4.6}$$

The crater shape PSD depends strongly on the ratio of rim height to crater depth, which through Equation 4.2 also controls the lateral extent of the ejecta blanket. Craters with no ejecta must have unrealistically tall rims to remain volume conserving ($h_{\mathrm{r}} = 2d'$). These craters contribute most of their power to wavelengths on the order of their diameter D. As the ratio h_{r}/d' decreases, the peak of the crater shape PSD broadens and moves to longer wavelengths, as the spatial footprint of the crater increases (Fig. 4.2). For self-similar craters, the peak frequency of the crater shape PSD is linear with D and the peak power scales as D^4, regardless of the crater shape parameters chosen.

To find an analytical expression to represent the resetting of initial topography, we first consider a harmonic surface with power in a single arbitrary frequency, k^*, over a domain X, within which an area D is reset to its own mean:

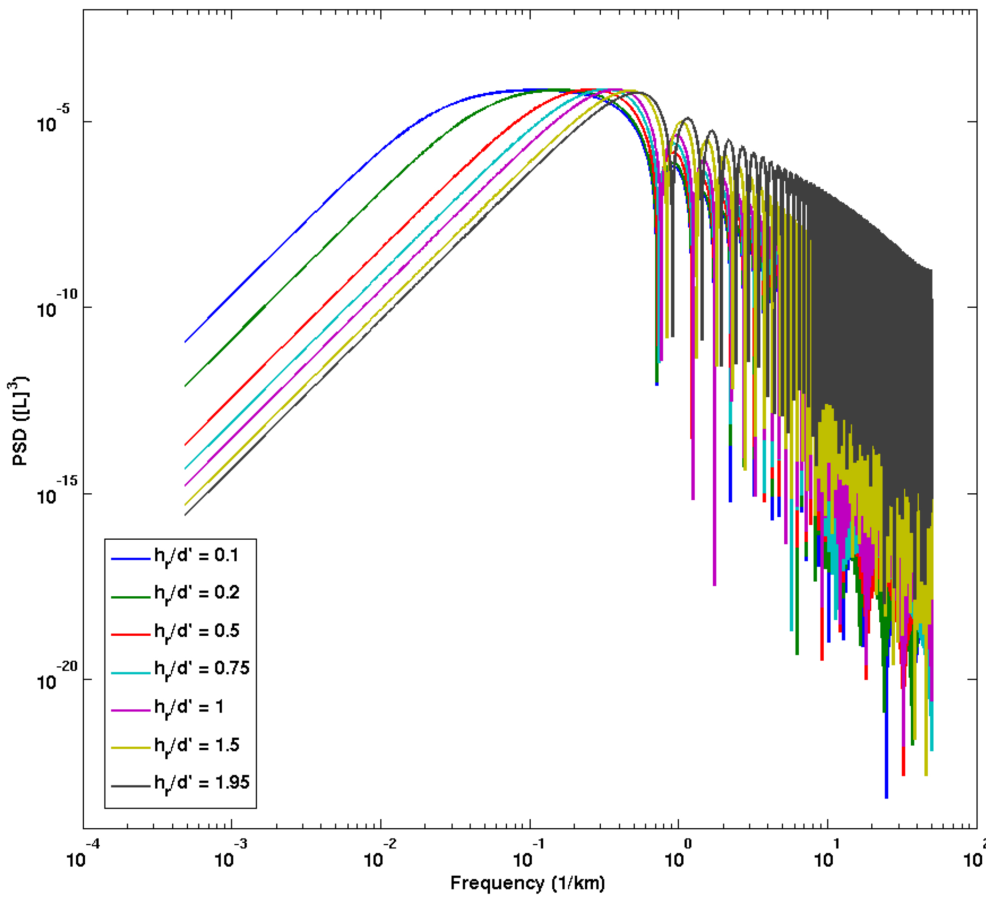

Figure 4.2: Examples of crater shape PSDs ($P_{\rm build}$) for craters with diameter $D = 2$ km. For volume-conserving craters, the ratio $h_{\rm r}/d'$ determines the value of the ejecta falloff exponent, γ, which in turn controls the shape of the crater shape PSD. Craters with no ejecta blanket ($h_{\rm r}/d = 2$, $\gamma = \infty$) have a narrow peak at frequency $f = 1/D$ ($k = 2\pi/D$). For $h_{\rm r}/d' < 2$, the peak in the PSD broadens and shifts to lower frequencies as the footprint of the crater increases.

$$h(x) = \begin{cases} \cos k^* x & |x - x_c| \le \frac{D}{2} \\ \frac{1}{D}\int_{x_c - D/2}^{x_c + D/2} \cos k^* x \mathrm{d}x & |x - x_c| > \frac{D}{2}, \end{cases} \tag{4.7}$$

where x_c is the center of the new crater and the region to be reset. Considering that the reset region can fall anywhere within the domain X, we must also average over all possible crater locations, and we can write an equation for the Fourier Transform of this function as follows:

$$F_{\text{reset}} = \int_{-X/2}^{X/2} \cos k^* x e^{-ikx} \mathrm{d}x + \int_{x_c - D/2}^{x_c + D/2} \left(\frac{2}{k^* D} \sin k^* D2 \cos k^* x_c - cos k^* x \right) e^{-ikx} \mathrm{d}x. \tag{4.8}$$

In calculating the PSD from this function, we find that the first term yields a Kronecker Delta function with height X^2 at $k = k^*$, while the second term integrates to a function that increases as k^2 at small frequencies, peaks at $k = 2\pi D$ (or $f = 1/D$), and falls off again as k^{-2} at high frequency (Fig. 4.3a).

Having found the effect of resetting on a single frequency, integration over k^* yields the total effect on the PSD of resetting an area of size D. Given an initial power spectrum with a steep slope at low frequencies, such as P_{build}, power is redistributed by resetting from the peak to lower frequencies, introducing a k^2 trend at the lowest frequencies (Fig. 4.3b).

The evolution of a 1D terrain that accumulates craters of size D can thus be completely captured by iterating between resetting (Eqn. 4.8) and crater building (Eqn. 4.6), a procedure that can be written in matrix form:

$$P_{\text{final}} = M P_{\text{initial}} + P_{\text{build}}. \tag{4.9}$$

M is the resetting matrix (each row of which is calculated from Equation 4.8 for a different k^*) that acts on the initial PSD of the topography before P_{build} is added. This matrix representation is especially useful because the equation can be inverted to find the equilibrium power spectral density, where $P_{\text{final}} = P_{\text{initial}} = P_{\text{equil}}$:

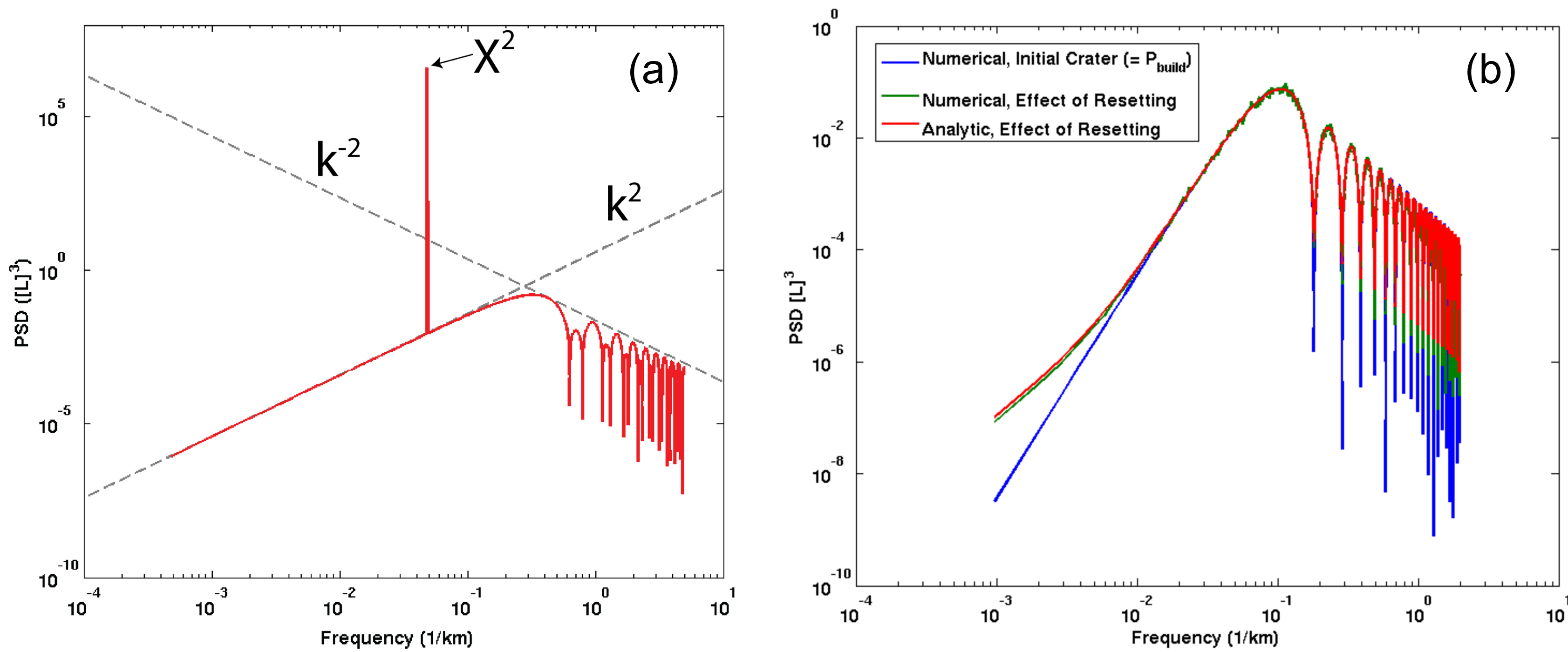

Figure 4.3: (a) PSD of a sinusoidal surface (of frequency k^*) on a domain of size $X = 1024$ km after an area $D = 5$ km has been reset to its own mean. Resetting transforms the initial PSD, a simple Delta function at $k = k^*$, such that the peak power diminishes, and power is added to low and high frequencies, where the PSD scales as k^2 and k^{-2}, respectively, peaking at $k \sim 2\pi/D$. (b) Effect on the PSD of resetting a surface containing a single crater. The numerical model is averaged over 100 instantiations, varying the location of the initial crater and the reset region. The analytic formulation sums the effect of resetting for each frequency (calculated from Eqn. 4.7), resulting in a redistribution of power from higher frequencies to lower frequencies, where the PSD scales as k^2.

$$P_{\text{equil}} = (I - M)^{-1} P_{\text{build}}. \tag{4.10}$$

The analytic formulation presented here provides a consistent benchmark for the numerical model results under simplified conditions (1D, self-similar craters of a single size, simple resetting algorithm), both for an evolving cratered terrain (Fig. 4.4a) and a landscape in equilibrium (Fig. 4.4b). The first crater emplaced contributes the crater shape PSD. Subsequent craters increase the magnitude of the PSD everywhere and introduce the k^2 trend at low frequencies due to resetting the terrain. After approximately one covering time ($\sim X/D$ craters), the PSD reaches equilibrium at its peak frequency, corresponding to wavelengths of scale D, as well as all higher frequencies, and power in this frequency range ceases to evolve with time. As more craters are emplaced, equilibrium extends to larger scales according to the square root of the number of craters (a proxy for time in these simulations). It is important to note that while the area of a surface may be covered with craters, its power spectrum will continue to evolve well past a single covering time until equilibrium is achieved at all frequencies.

4.2.2 Synthetic PSDs

Because the equilibrium PSD for a given crater size D peaks at a unique frequency related to D, a procedure for combining craters of different sizes according to a given size-frequency distribution may be derived. The resulting PSD (referred to here as the "synthetic" PSD) can then be compared to the PSD derived from the numerical model, in which craters of different sizes are emplaced together on a domain.

The equilibrium PSD for single-size craters is characterized by a flat region at long wavelengths, a peak whose magnitude scales as D^3, and a k^{-2} tail at short wavelengths with peaks at integer multiples of D. Both the location and the magnitude of the primary peak vary with crater shape (h_{r}/d'), displaying different behaviors above and below $\gamma = 3$ (corresponding to $h_{\mathrm{r}}/d' = 1$) (Fig. 4.5a). For craters with little or no ejecta blanket, the peak in the PSD occurs at $f = 1/D$ and moves linearly to longer wavelengths as h_{r}/d' decreases (Fig. 4.5a), according to:

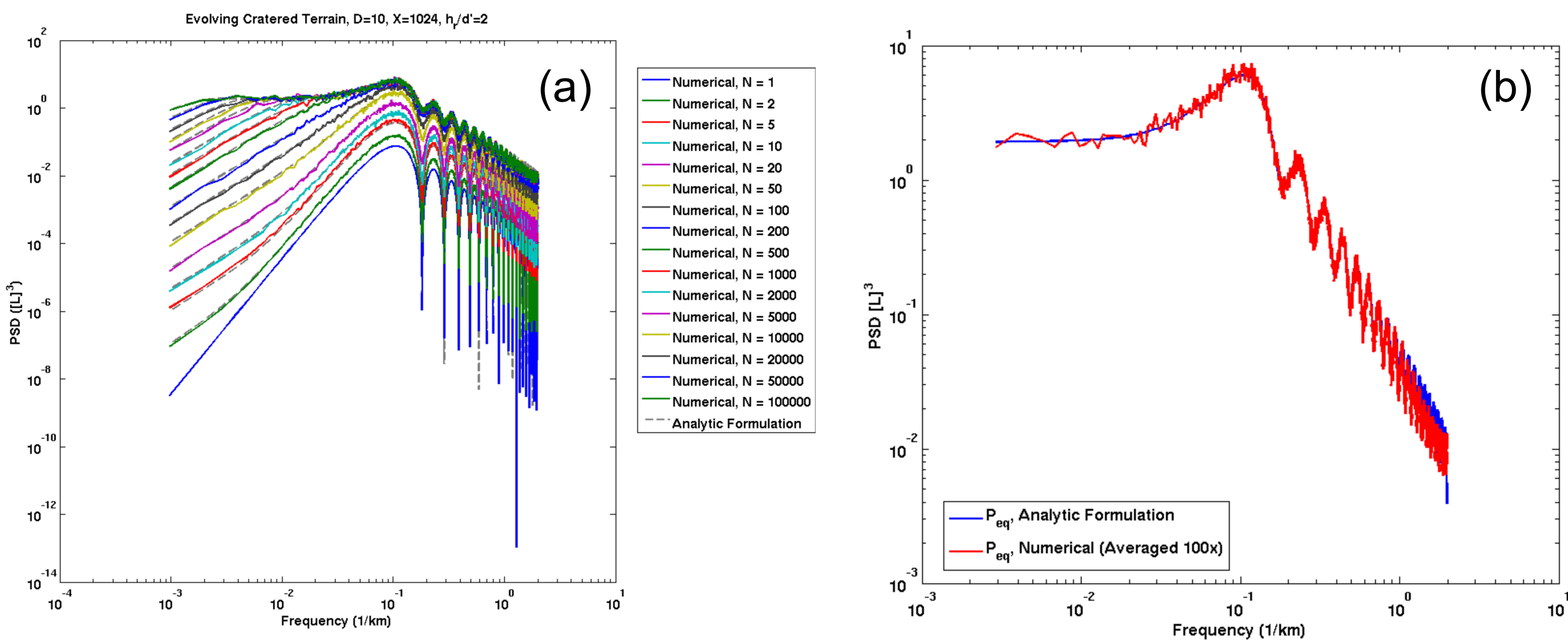

Figure 4.4: (a) Comparison of the numerical and analytic approaches to modeling the power spectral density of an evolving cratered terrain. All models are 1-dimensional, with self-similar craters of diameter $D = 10$ km and no ejecta blanket ($h_{\mathrm{r}}/d' = 2$). Dashed lines represent the analytic formulation, while colored lines show the numerical results averaged over 100 iterations each. After the first crater is emplaced, the PSD is exactly equal to P_{build}. As craters continue to accumulate, a k^2 trend is introduced at low frequencies, and the overall magnitude increases, clearly showing the alternating effects of resetting the surface and building new crater shapes. As the surface approaches equilibrium, the highest frequencies stabilize first, and the equilibrium PSD begins to take shape with the flat region shifting to lower frequencies. (b) Equilibrium PSD calculated by solving the matrix relation for resetting and building with craters of a single size $D = 10$ km (Eqn. 4.9). The analytic formulation agrees with the numerical model, which was averaged over 100 instantiations, each accumulating 10^5 craters on a domain of size $X = 1024$ km.

$$f_{\max} = \begin{cases} \frac{1}{D} & \gamma \geq 3 \\ \frac{\gamma}{3D} & \gamma < 3. \end{cases} \tag{4.11}$$

The magnitude of the peak is approximately constant for high values of γ and scales as γ^2 for smaller values (Fig. 4.5b).

To first order, the power contributed by crater size D in equilibrium is dominated by the primary peak, which scales as D^3, as expected from Equation 4.5 for self-similar craters and $f_D = 1$ (single-size craters). To approximate the equilibrium PSD of a terrain covered with craters of many sizes, we can add the individual single-size equilibrium PSDs in a prescribed proportion. This proportion depends on the frequency of occurrence (specified by the size-frequency power law exponent α) and the fraction of the surface, f_D, characterized by craters of that size. When large craters dominate the area (when $\alpha < L$, the dimensionality of the model), f_D is simply proportional to the area of the crater, D^L, because large craters erase everything smaller than themselves with a single covering. When small craters dominate the area, they must have time to diffuse topography at larger scales to erase them, and f_D is proportional to D^{L+2}. Using the latter relation, we expect the PSD to scale as:

$$k^{-\beta} \sim D^{\beta} \sim D^3 D^{-\alpha} D^{L+2} = D^{L+5-\alpha}. \tag{4.12}$$

Comparing the result to our functional form for the PSD, $k^{-\beta}$, we find that in 1D the power law exponent of the PSD, β, obeys a simple relation: $\beta \sim 6 - \alpha$.

The slope of the power spectral density on a log-log plot against frequency, β, varies inversely with the size-frequency distribution exponent, α. As α increases, the number of small craters for every large crater also increases, producing more features on small scales and thus shallowing the PSD. We expect this tradeoff to occur at intermediate values of α, while in the high- and low-α limits, we expect β to become constant. For low α, the surface topography is dominated by craters of the largest size, $D_{\max}$, and the equilibrium PSD resembles the single-size PSD for $D_{\max}$. The peak therefore occurs at approximately $f \sim 1/D_{\max}$, which is near (but greater than) the minimum

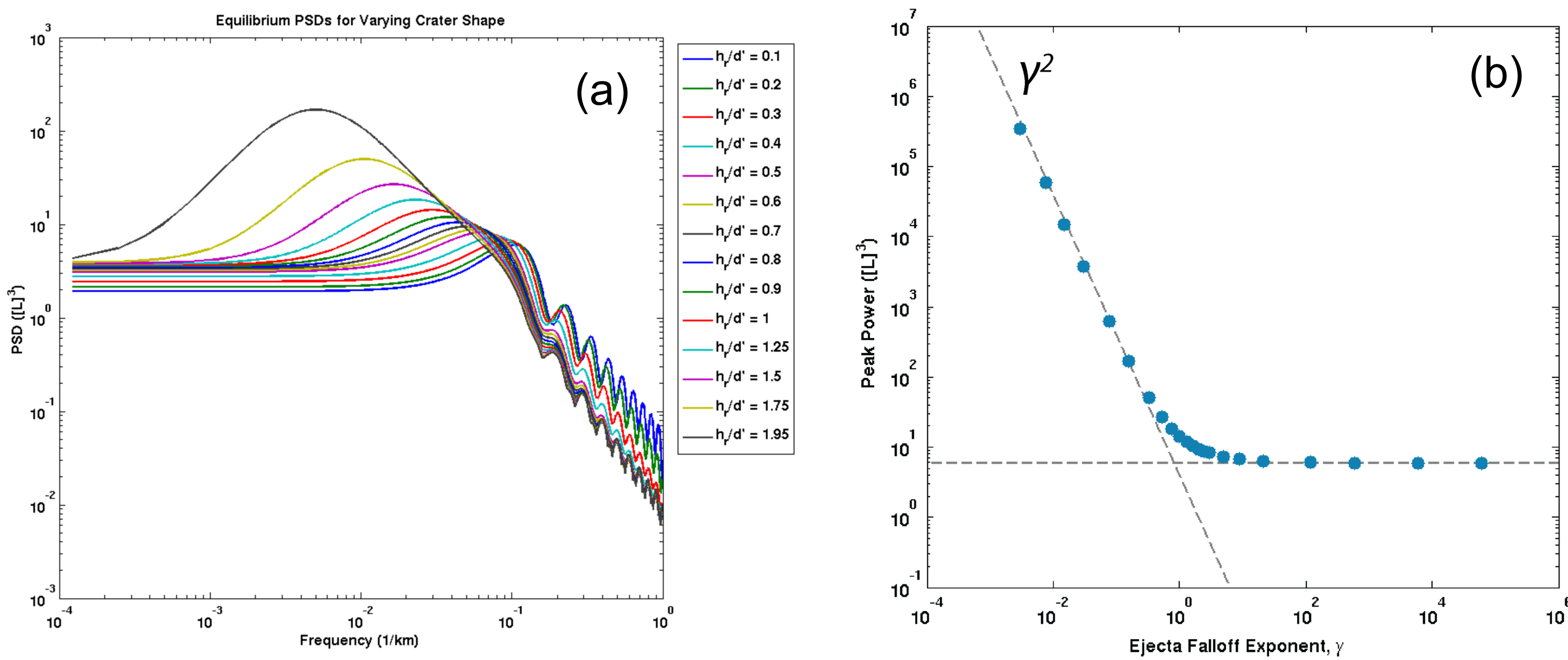

Figure 4.5: (a) Equilibrium PSDs for craters of size $D = 10$ km, consisting of a flat region at low frequencies, a peak whose location and magnitude depend on the crater shape parameters, and a high frequency tail that falls off as k^{-2}. For high values of h_{r}/d' (high γ), the peak occurs at frequency $f = 1/D$ ($k = 2\pi/D$), and shifts to lower frequencies as the ejecta extent increases (as h_{r}/d' decreases). (b) In equilibrium, the peak of the PSD (for 1D, single-size craters) is constant for high γ ($\gamma \geq 3$, or $h_{\mathrm{r}}/d' \geq 1$) and scales as γ^2 for lower values. This corresponds to an increase in peak power for craters with extended ejecta blankets.

frequency set by the domain size, $1/X$. For all frequencies greater than $1/D_{\mathrm{max}}$, the PSD resembles the high-frequency tail of the single-size PSD for D_{max}, which has a slope of $\sim k^{-2}$. Therefore, $\beta \sim 2$ in the low-α limit. For high α, the surface topography is dominated by the smallest craters, D_{min}, and the equilibrium PSD resembles the single-size PSD for D_{min}. The peak in the PSD occurs at approximately $f \sim 1/D_{\mathrm{min}}$, which is near (but less than) the maximum frequency set by the resolution of the model (the Nyquist frequency), and $\beta = 0$ for smaller frequencies. Thus, for a 1D domain and to first order, we predict β to behave as follows:

$$\beta = \begin{cases} 2 & \text{High } \alpha \\ 6-\alpha & \text{Intermediate } \alpha \\ 0 & \text{Low } \alpha. \end{cases} \tag{4.13}$$

This prediction is tested in two ways: first, by synthetically combining the single-size PSDs according to the prescription derived above in Equation 4.12, and second, by using the numerical model to emplace craters of different sizes together as a function of α. Figure 4.6 shows the results of both model types for 1D, self-similar craters with no ejecta blanket ($h_{\mathrm{r}}/d' = 2$) and values of α ranging from 0.25 to 8. For the numerical model, the PSD was averaged over many covering times. The power law exponent of the synthetic PSDs behaves as expected from Equation 4.13: β remains relatively constant at $\beta \sim 2$ for low α and transitions to a constant at $\beta = 0$ for high α. Intermediate values of α generate PSDs that fit our expectation of $\beta \sim 6 - \alpha$.

The results of the numerical model show more structure than the first-order prediction summarized in Equation 4.13, and this can be understood by considering in detail the processes of building and erosion of topographical features at every scale and the crater sizes that are most efficient at each of these processes. The range of size-frequency exponents, α, can thus be divided into several distinct regimes, which are marked by horizontal arrows in Figure 4.6. First, one may consider which crater size, for a given α, is most efficient at covering the area of the domain; the answer will depend on the footprint of the crater and its frequency of occurrence, and except for the special value of $\alpha = L$, either the smallest or the largest craters included in the model will dominate the

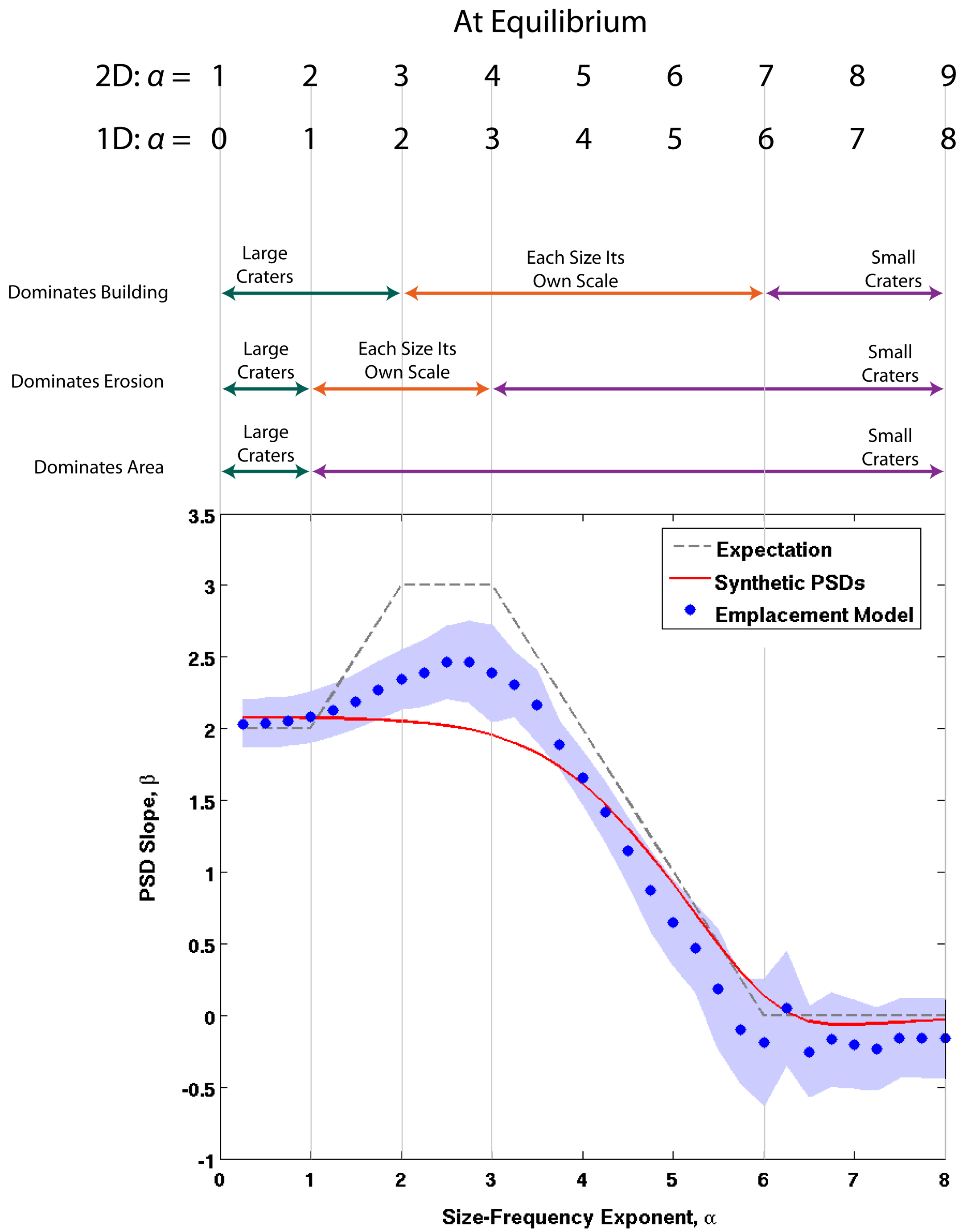

Figure 4.6: Power law exponent of the equilibrium PSD, β, comparing the numerical emplacement model, in which craters of different sizes are emplaced together according to a given size-frequency distribution, and the synthetic PSDs, which are a weighted sum of single-size equilibrium crater PSDs. The PSD is calculated from topography generated by the numerical model and averaged over many iterations once equilibrium conditions have been achieved (i.e., once the PSD ceases to evolve with the addition of more craters). The shaded region indicates 2σ error bars from the averaging and fitting the power law exponent.

area. At $\alpha = L$, all craters occupy an equal fraction of the total area of the domain. Which craters dominate the area, however, plays little role in the resulting behavior of β; this is determined by the interaction between building and erosion at every scale.

To understand this interaction, we examine each significant range of α for building and erosion separately and then consider their joint effect. From Figure 4.4, it is clear that, for a given crater diameter, equilibrium is reached first at frequencies greater than or equal to the peak frequency ($f \sim 1/D$), and the PSD in this range goes as $\sim k^{-2}$. At all lower frequencies, the PSD is characterized by a k^2 trend before equilibrium is reached. For different values of α, the power at any given scale will be primarily contributed by either the smallest craters, the largest craters, or craters with diameters near that scale. In the first case, the smallest craters contribute a spectrum that goes as k^2 for all frequencies lower than $f \sim 1/D_{\mathrm{min}}$. Large craters, on the other hand, contribute a k^{-2} spectrum at all frequencies higher than $f \sim 1/D_{\mathrm{max}}$. In between, each crater of a given diameter D will contribute the most power to its own peak frequency, at which frequency the power scales as D^{3+L}, and the total power from all craters of size D scales with their number: $D^{3+L}D^{-\alpha}$. Comparing these contributions to the total PSD, we find the boundaries marked in Figure 4.6 for building. For a particular scale D, the largest craters and craters of size D will contribute equally to building when $\alpha = L + 1$, while the smallest craters and craters of size D will contribute equally when $\alpha = 5 + L$.

Just as with building, the erosion of features of a given scale will be dominated by either the largest craters, the smallest craters, or craters with diameters on that scale. The smallest craters diffuse their own scale (and smaller scales) in the time it takes them to cover the surface, but to erode larger craters, they must cover the surface many times. The time it takes to diffuse a crater of scale D' with craters of size D ($D \leq D'$) may be estimated as:

$$t_{\mathrm{diff}} = \left(\frac{D'}{D}\right)^2 \frac{1}{c} D^{\alpha-L} = \frac{1}{c} D^{\alpha-L-2} D'^2. \tag{4.14}$$

where c is the same constant as in Equation 4.3, whose units depend on α. The diffusion time goes as D'^2, which is also reflected in Figure 4.4, as equilibrium spreads to lower frequencies at a rate proportional to the square root of the number of craters emplaced. Diffusion by the smallest craters thus contributes a k^{-2} spectrum to all larger scales. By contrast, large craters do not need to diffuse the scales smaller than themselves to erode them; they need only cover them. Once the surface has been covered with craters of the largest size, all smaller scales have also been eroded, and this process contributes a scale-independent spectrum, k^0. As with the building process, there is an intermediate range in which craters of each size dominate the erosion of their own scale, and this can be seen in Equation 4.14 when $D = D'$. For this case, the diffusion time goes as $t_{\text{diff}} \propto D^{\alpha-L}$, and diffusion in this regime contributes a spectrum of $k^{L-\alpha}$. The boundaries of these erosion regimes are determined by comparing the spectra contributed by each class of craters. For a particular scale D, the largest craters and craters of size D will contribute equally to erosion when $\alpha = L$, while the smallest craters and craters of size D will contribute equally when $\alpha = L + 2$.

These building and erosion regimes, marked by arrows in Figure 4.6, can now be compared to determine the total effect on the behavior of β. For the steepest size-frequency distributions ($\alpha > L + 5$), the PSD is expected to scale as k^2 (from building) multiplied by k^{-2} (from erosion), yielding a value of $\beta = 0$. For α between $L+2$ and $L+5$, $k^{\alpha-L-3} \cdot k^{-2} = k^{\alpha-L-5}$ and $\beta = \alpha - L - 5$. The range of α between $L + 1$ and $L + 2$ is special in that craters of a given size dominate both the building and erosion of their own scale, and the resulting PSD power law exponent is independent of α: $k^{\alpha-L-3} \cdot k^{L-\alpha} = k^{-3}$. β is expected to be 3 in this range. For α between L and $L + 1$, $k^{-2} \cdot k^{L-\alpha}$ yields $\beta = \alpha - L + 2$, and for the smallest range of $\alpha < L$, $k^{-2} \cdot k^0$ predicts a constant value of $\beta = 2$, as Equation 4.13 originally suggested. The numerical emplacement model reproduces this behavior in the power law exponent of the equilibrium PSD, with the exception that it fails to produce values of β greater than ~ 2.5, a circumstance that we believe would be improved (at significant computational expense) by further increasing the dynamic range of the model.

4.2.3 Effect of Crater Shape

The behavior described in Figure 4.6 applies in any models using self-similar craters, regardless of crater shape. This occurs because for a given shape parameter ratio h_{r}/d', the peak frequency is inversely proportional to D, preserving the scaling in Equation 4.12. Realistic craters are not

	Rim Height (for D in km)	Rim-to-Floor Depth (for D in km)
Simple Craters ($D < 15$ km)	$h_{\mathrm{r}}D = 0.036D^{1.014}$	$dD = 0.196D^{1.010}$
Complex Craters ($12 < D < 375$ km)	$h_{\mathrm{r}}D = 0.230D^{0.399}$	$dD = 1.044D^{0.301}$

Table 4.1: Morphometric relations for lunar craters, from *Heiken et al.* (1991), based on measurements from *Pike* (1974) and *Pike* (1977).

self-similar, but have shape parameters that scale with diameter. In addition to smooth changes in shape with increasing size, the transition diameter from simple to complex craters introduces an abrupt change, both in crater shape and in rim-to-floor depth (amplitude of the feature). This transition scales with surface gravity, and occurs around $D = 15$ km on the Moon. Morphometric relations for fresh lunar impact craters are listed in Table 4.1 in *Heiken et al.* (1991), based on *Pike* (1977) and *Pike* (1974), and these scaling relationships are summarized in Figure 4.7 and Table 4.1. Simple craters have a nearly constant shape parameter ratio of $h_{\mathrm{r}}/d' \sim 0.23$, while complex craters span a range of values from $h_{\mathrm{r}}/d' \sim 0.43$ to 0.67. Likewise, the rim-to-floor depths of simple craters scale linearly with their diameters, with a depth-to-diameter ratio of $d \sim 0.2$. This observation is consistent with recent investigations based on LOLA topography data (*Talpe*, 2012). Complex craters have lower amplitudes for their size, and this amplitude decreases with increasing diameter. The abrupt change in these two quantities—crater shape/ejecta extent and amplitude—at the transition diameter provides expectations for particular changes in the shape of the PSD. Simple craters add more power relative to their diameters than complex craters, and they add this power to lower frequencies according to Equation 4.11.

In one test, using self-similar craters with an abrupt transition at $D_{\mathrm{tr}} = 15$ km from $h_{\mathrm{r}}/d' = 0.2$ to 0.5 (corresponding to $\gamma = 1/3$ and $\gamma = 1$, respectively), synthetic PSDs for various values of α clearly reflect the change in crater shape (Fig. 4.8). For comparison, the sample runs including only self-similar simple craters and only self-similar complex craters are included in Figure 4.8 as dashed dark and light gray lines, respectively. At low α, the equilibrium PSD resembles the

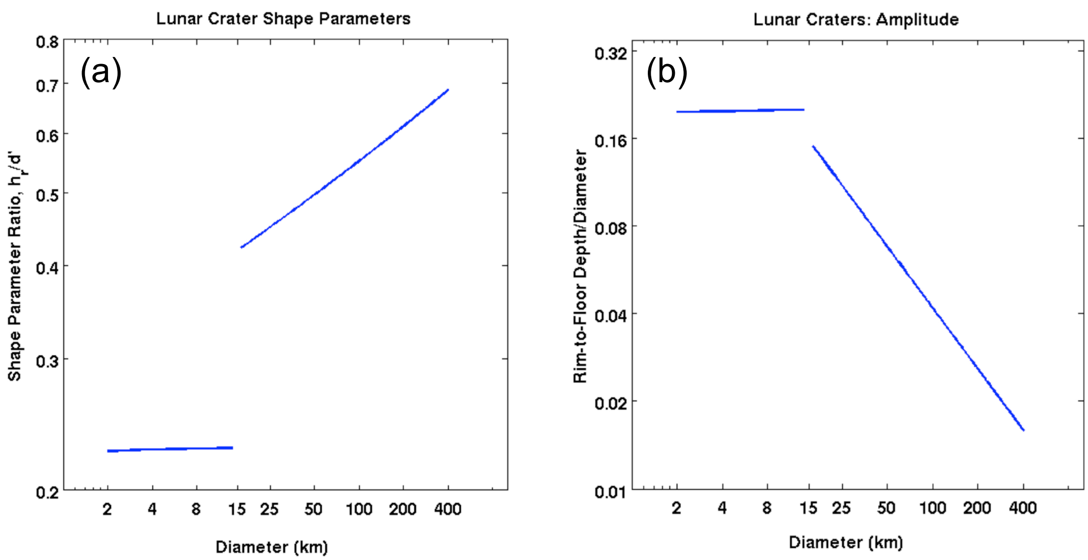

Figure 4.7: (a) Shape parameter ratios for lunar craters, based on morphometric relations listed in Table 4.1 of *Heiken et al.* (1991). Simple craters have lower rims relative to their diameters than complex craters, which means to be volume-conserving they must have more extensive ejecta blankets. Thus the peak frequency for crater shape PSDs occurs at lower frequencies for simple craters relative to their diameters, and the peak power is also greater, according to Eqn. 4.11 and Fig. 4.5b. Simple craters are nearly self-similar, while complex craters vary in shape a great deal. As diameter increases, crater rims become higher and ejecta more confined, resulting in crater shape PSDs with peaks nearer to $f = 1/D$. (b) Rim-to-floor depth (crater amplitude), based on morphometric relations listed in Table 4.1 of *Heiken et al.* (1991). Simple craters have a higher amplitude for their size than complex craters, meaning that they contribute proportionally more power at their peak frequencies. Simple craters are also nearly self-similar, while complex craters decrease in amplitude (relative to their diameters) with increasing size.

corresponding complex-craters-only case, as the largest craters dominate. When $\alpha = 3$, the smallest craters start to contribute to the overall PSD, beginning at the peak frequency of the largest simple crater ($D_{\mathrm{tr}} = 15$, $f_{\mathrm{peak}} \sim \gamma/3D \sim 1/135 = 0.0074$) and extending to all higher frequencies. For intermediate α, between 4 and 6, the equilibrium PSD follows the complex crater curve at low frequencies and transitions to follow the simple crater curve at high frequencies. Above $\alpha \sim 6$, the PSD is equivalent to the simple-craters-only case. If, instead of the abrupt transition at $D_{\mathrm{tr}} = 15$ km, the transition from simple to complex craters is smoothed out over a range of diameters near D_{tr} (e.g., from D =12-18 km), the resulting PSDs are qualitatively similar to the abrupt-transition case. Slight differences in the intermediate range of α's occur because the effect of the smallest craters is softened by the smoothed transition, and the larger craters dominate the total PSD shape to slightly higher frequencies.

Finally, we include the smooth power-law scaling of crater shapes summarized in Table 4.1. Simple craters are nearly self-similar, and their behavior is well understood within the analysis described so far. Complex craters, however, are not self-similar; their rim-to-floor depth- and rim height-to-diameter ratios scale as $D^{0.301}$ and $D^{0.399}$, respectively (Table 4.1). This dependence on diameter leads to a modified expectation for the peak power scaling for individual crater sizes. According to Equation 4.5, the power at the peak frequency goes as $P(f_{\mathrm{peak}}) \sim H^2 D f_D$ (where the amplitude H is the rim-to-floor depth, dD). When the depth-to-diameter ratio d scales linearly with diameter and $f_{\mathrm{peak}} \sim 1/D$, this peak power scales as D^3, as we have seen in our self-similar cratering models. In this case, however, $H \sim D^{0.301}$, and $f_{\mathrm{peak}} \sim D^{-0.8}$ (according to Eqn 4.11). Thus, the power at f_{peak} scales as $P(f_{\mathrm{peak}}) \sim D^{0.602} D f_D \propto D^{1.602}$, from which we can calculate how the peak power scales with diameter:

$$P_{\mathrm{peak}}(D) \sim \left(\frac{1}{D^{0.8}}\right)^{1.602} \sim D^{1.3}. \tag{4.15}$$

This scaling agrees with the results of the analytic model, and using Equation 4.12 and Equation 4.13, we can predict how the portion of the equilibrium PSD dominated by large craters behaves with varying size-frequency distribution. For intermediate values of α, $\beta \sim 1.3 + 2 + L - \alpha = 4.3 - \alpha$.

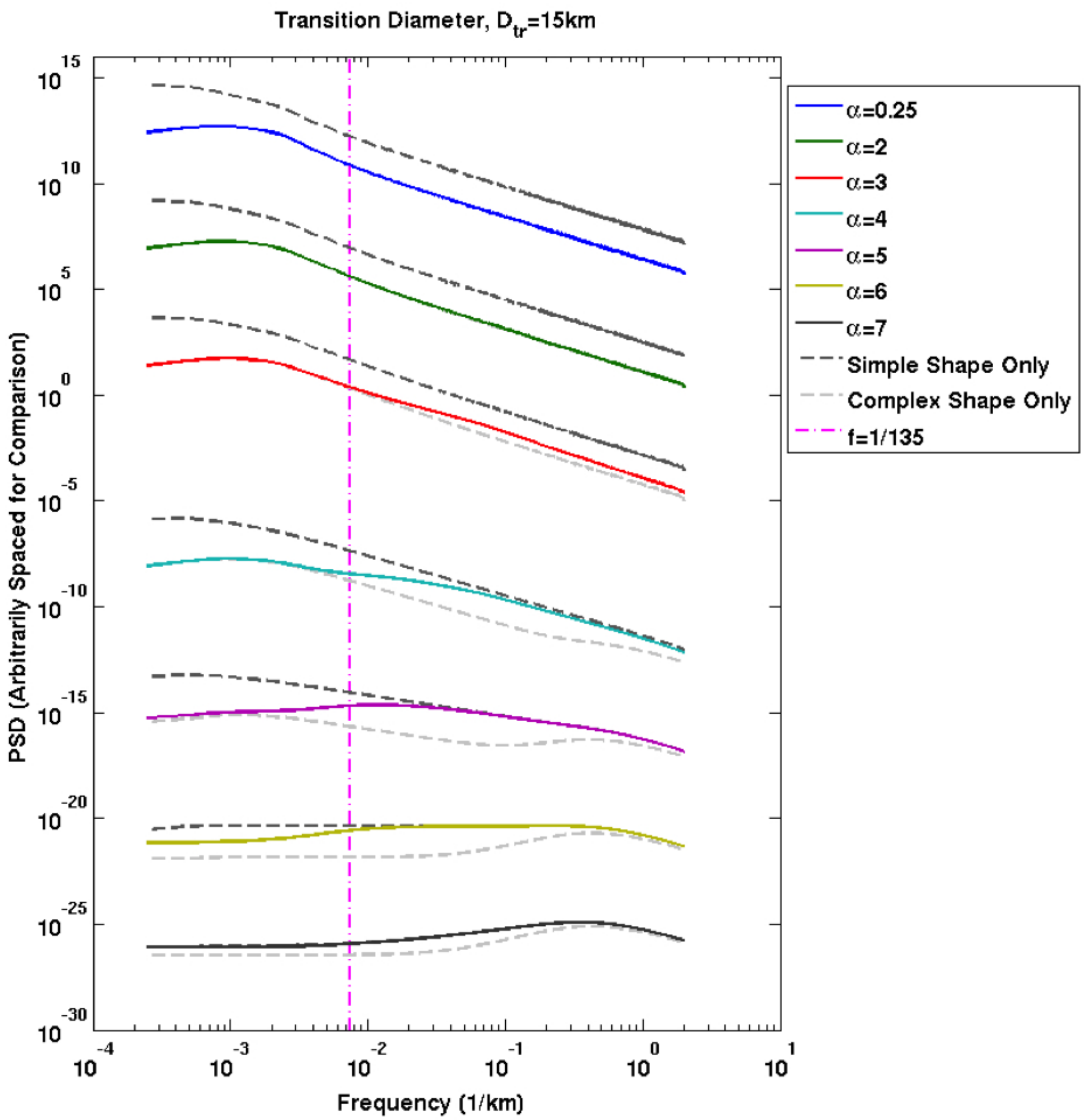

Figure 4.8: One-dimensional equilibrium PSDs for varying size-frequency distribution exponents, α, and a transition diameter, $D_{\rm tr} = 15$ km. Craters above $D_{\rm tr}$ are self-similar with shape parameters $h_{\rm r}/d' = 0.5$, $\gamma = 1$ (complex craters); craters below $D_{\rm tr}$ are self-similar with shape parameters $h_{\rm r}/d' = 0.2$, $\gamma = 1/3$ (simple craters). Dashed lines indicate model runs using only complex (light) or only simple (dark) crater shape parameters. For low α (< 3), equilibrium PSDs remain unaffected by the transition from simple to complex craters. For intermediate values of α ($\sim 4-6$), however, PSDs transition from matching the complex crater PSDs at low frequencies to matching the simple crater PSDs at high frequencies. This transition occurs first at $\alpha = 3$, where the extra power contributed by simple craters due to their shape (low $h_{\rm r}/d'$, extended ejecta) and high amplitude create a shoulder beginning at the peak frequency for the largest simple crater, $D = D_{\rm tr} = 15$ km. As α increases, the PSD increases in magnitude at the high frequencies first, quickly coming to resemble the simple crater PSDs. At low frequencies, the PSD resembles the complex crater PSDs until the small craters overwhelm the large craters and the entire range resembles the simple crater PSD.

At frequencies dominated by small craters, the D^3 scaling for peak power still holds, and the original Equations 4.12 and 4.13 are applicable. Thus, for 1-dimensional versions of lunar-like craters, the equilibrium PSD has two slopes that evolve separately, but predictably.

4.2.4 2-Dimensional Emplacement Models

The equations developed thus far to describe the behavior of 1D cratered terrains provide valuable predictions for the 2D case as well. Here, rather than calculating the two-dimensional Fourier Transform to estimate the PSD, we calculate the 1D PSD of each row and column of a 2D model surface and compute the average to facilitate comparison with the LOLA along-track measurements. The 2D model craters have an axisymmetric, parabolic cavity with a radial profile identical to that of their 1D counterparts. The ejecta blanket function differs somewhat, however, because the condition for volume conservation becomes:

$$\gamma = \frac{2h_{\mathrm{r}}\left(d'/h_{\mathrm{r}}\right)^{\frac{1}{2}}}{d' - h_{\mathrm{r}}}. \tag{4.16}$$

Because the ejecta spreads out radially with distance from the crater, the maximum rim height (no ejecta) case occurs where $h_{\mathrm{r}}/d' = 1$ and any given profile through the crater center is not itself volume conserving. This condition results in a somewhat different shape for the single crater PSD, which has a modest peak at $f \sim 1/D$ (for the no ejecta case) and a flat region at low frequency, whereas the 1D crater PSDs scaled as k^4 at low frequency. The peak power for an individual 2D crater scales as D^5, the extra power of D arising from a second integral over the spatial parameter in Equation 4.5. As before, it is possible to calculate synthetic PSDs of cratered terrains by adding the equilibrium PSDs of individual crater sizes in proportion to a given size-frequency distribution. The peak power of the equilibrium PSD scales as D^3 just as in the 1D case, and the power is constant from the peak to lower frequencies. Equation 4.12 is used with a value of $L = 2$ to predict the slope of the PSD, β, as a function of the size-frequency distribution exponent, α:

$$\beta \sim L + 5 - \alpha = 7 - \alpha. \tag{4.17}$$

This behavior is consistent with the PSDs derived from the numerical emplacement model, and is summarized in Figure 4.6. The power law exponent of the PSD for 1D and 2D domains is identical except for an offset of 1 in α.

4.2.5 Effect of Inheritance

Thus far, the resetting phase of crater emplacement has been modeled as simply as possible: the pre-existing topography is surveyed and reset to its mean within half a diameter of the center of the new crater to be emplaced. This algorithm is convenient, as we have seen, in that it permits an analytical representation of the power spectral density evolving with multiple impacts, and it also takes into account the erasure of the initial terrain while providing a reasonable reference elevation upon which to superimpose the new crater topography. However, the physical processes taking place in an impact event, which our resetting phase only approximates, are poorly understood, and other cratered terrain models have employed various algorithms to address this gap in our present understanding of the impact process. *Howard* (2007) introduces the inheritance parameter, I, which controls the degree to which pre-existing topography is preserved during crater emplacement. Within the rim, the terrain is reset to a linear combination of a reference mean elevation, h_{ref}, and the initial topography, h_i, favoring the latter near the rim and the former in the center of the cavity. Between the center and the rim, the degree of resetting varies as a parabola scaled by I:

$$h_{\mathrm{reset}} = (h_{\mathrm{ref}} - h_i)\left[1 - I\left(\frac{2r}{D}\right)^2\right]. \tag{4.18}$$

This approach has the advantage that the edge produced at the rim by the resetting step is softened when I is greater than 0. This edge—equivalent to a step function in our simple resetting procedure—is responsible for the k^{-2} slope at high frequency in the equilibrium PSD for a single crater size, because the Fourier Transform of a Heaviside function produces a slope of -1 in the frequency domain and the PSD is calculated from the square of the magnitude of the FFT. Hence, for terrains accumulating craters of many sizes, this choice of resetting algorithm has important consequences for the power spectral slope, which tends to level off at $\beta \sim 2$ when the size-frequency

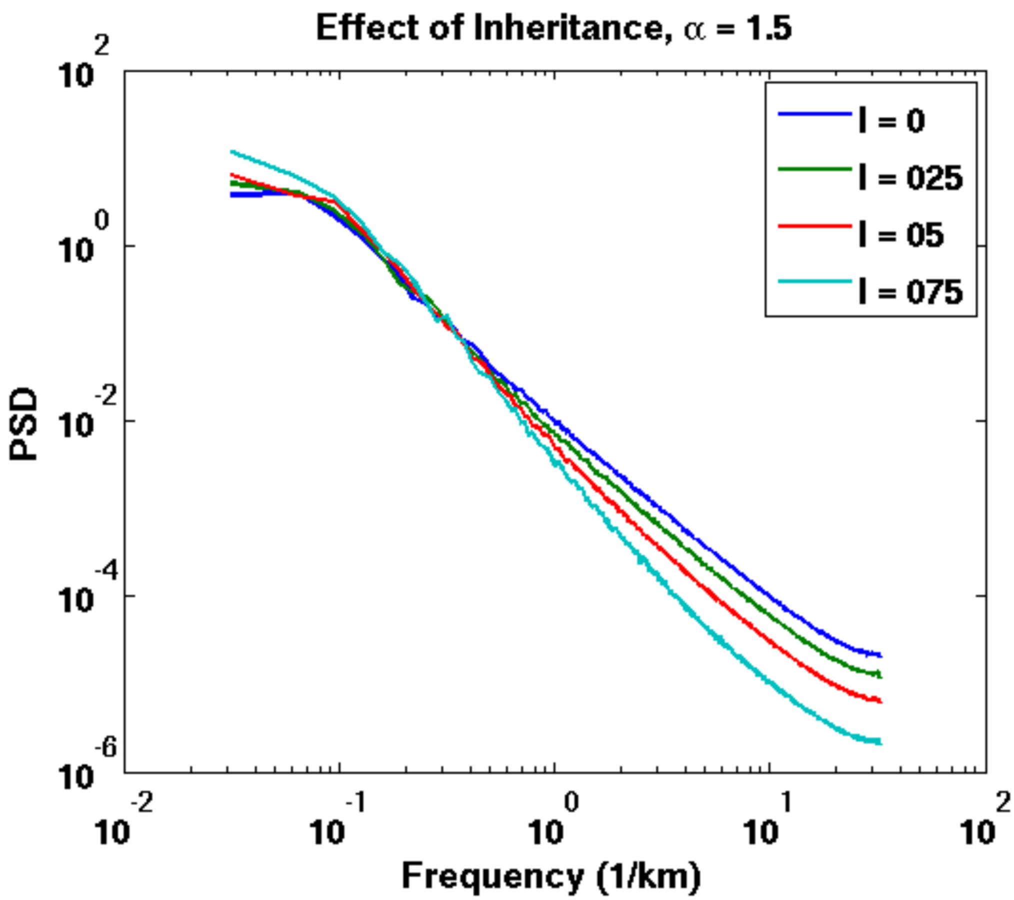

Figure 4.9: PSDs of cratered terrains with different values of *Howard* (2007)'s inheritance parameter, I. At high frequency, the slope is relatively unchanged, but at low frequency it steepens for smoother terrains generated using higher values of I.

distribution is shallow (low α), as shown in Equations 4.13 and 4.16. This occurs because the largest craters dominate the power, and the entire PSD comes to resemble the high-frequency tail of the single-size PSD for $D_{\max}$.

To investigate how the choice of resetting algorithm affects the behavior of the PSD slope, we employed several variations of both our simple resetting procedure and the inheritance formula of *Howard* (2007) described above. We observed that algorithms producing a smoother terrain during the resetting phase (i.e., continuous at the rim, but not necessarily having a continuous first derivative) resulted in PSD slopes exceeding the value of $\beta \sim 2$ at low frequency. Figure 4.9 contains an example in which model runs use a variant of Howard's inheritance algorithm that is identical inside the crater rim, but modified to be smoother outside to avoid unnecessary breaks in slope in the reset topography. The inheritance parameter, I, ranges here from 0 to 0.75, and the equilibrium PSDs for a size-frequency distribution with $\alpha = 1.5$ are plotted together, showing a clear steepening of the PSD at low frequency from $\beta \sim 2$ for $I = 0$ and $\beta \sim 3$ for $I = 0.75$. At high frequency, the slope is unchanged, indicating that the choice of resetting algorithm primarily affects long-wavelength topographic structures and is less important for small scales.

4.3 Size-Frequency Distributions

Much work has been done to determine the size-frequency distribution of craters in different areas of the Moon's surface (*Chapman and McKinnon*, 1986; *Hartmann and Gaskell*, 1997; *Neukum et al.*, 2001; *Ivanov et al.*, 2002), and to relate these observed crater size-frequency distributions to the population and flux of impactors that created them (*Hartmann and Gaskell*, 1997; *Richardson*, 2009). These studies show that lunar craters do not follow a single power law over the entire range of crater sizes. Rather, the size-frequency distribution is better approximated by a piecewise segmented power law or by a polynomial. The Hartmann production function (HPF) described in *Neukum et al.* (2001), formulated as the number of craters on typical mare surfaces, has three segments:

$$\begin{aligned}
\log N_{\mathrm{inc}} &= -2.616 - 3.82 \log D_{\mathrm{L}} && D_{\mathrm{L}} \leq 1.41\ \mathrm{km} \\
\log N_{\mathrm{inc}} &= -2.920 - 1.80 \log D_{\mathrm{L}} && 1.41\ \mathrm{km} < D_{\mathrm{L}} \leq 64\ \mathrm{km} \\
\log N_{\mathrm{inc}} &= -2.198 - 2.20 \log D_{\mathrm{L}} && D_{\mathrm{L}} > 64\ \mathrm{km},
\end{aligned} \tag{4.19}$$

where N_{inc} gives the number of craters in each $\sqrt{2}D$ diameter bin and D_{L} is the left boundary of each diameter bin. Small craters thus have a steeper size distribution than larger craters ($\alpha = 3.82$ *vs.* $\alpha = 1.8$). This difference is significant because cratered terrains evolve quite differently for α above and below 2 (for a 2D terrain), especially as they approach equilibrium, defined as the case where an incoming crater of size D will, on average, erase another crater of size D and the size-frequency distribution of craters ceases to evolve with time. The analysis developed thus far for the dependence of the PSD power law exponent on α is therefore useful in understanding the behavior of observed lunar size-frequency distributions as well. As described in Figure 4.6, $\alpha = L$ (the dimensionality of the model or data domain) is a special size-frequency distribution in which craters of all sizes occupy equal areas of the domain. For values of α less than L, large craters cover more of the area than small craters, and they erase smaller craters than themselves simply by covering them. In this case, the equilibrium size-frequency distribution is not constant in time. Over time, small craters initially build up a size-frequency distribution that follows the original α, but they are erased by larger craters that reset much of the domain. On average, the initial power law slope α is preserved, but the instantaneous size-frequency slope oscillates around this value.

For values of $\alpha > L$, the area is dominated by small craters. If craters are assumed to be erased by covering only (as in the previous case), then the smallest craters, of size D_{min}, will erase all other crater sizes before they will have had time to come into equilibrium with themselves. Thus, the observed size-frequency distribution will have the same slope as the production function, α. However, as shown in Figure 4.6 and Equation 4.14, diffusion is the dominant process of erosion for $\alpha > L$, and for $L < \alpha \leq L + 2$, each crater size is responsible for the erosion of features on its own scale. In this case, crater rims are not destroyed in one covering, and all crater sizes have the opportunity to reach equilibrium with respect to their own size class. As *Soderblom* (1970) demonstrated analytically, the equilibrium size-frequency distribution of craters in this case is independent of α, following a power law slope of L. Starting from a flat plane, therefore, the size-frequency distribution will initially retain the production function power law slope α as craters accumulate. The smallest craters will reach equilibrium first, and a kink appears in the size-frequency distribution, which has a slope of L at small crater sizes and α at large crater sizes. With time, this kink migrates to larger diameters until the entire size range is in equilibrium. The crater diameter at which the kink occurs is therefore an indication of the age of the cratered surface (*Melosh* (1989), Fig. 10.5). This case can be compared to the behavior of the PSD in the range of α between $L + 1$ an $L + 2$, where both the building and erosion processes at a given scale are dominated by craters of that scale, and the resulting PSD power law exponent is constant at $\beta = 3$.

For higher values of α ($> L+2$), the smallest craters dominate the diffusion of all other scales, and they erase all larger craters faster than they can come into equilibrium with themselves. The diffusion time, t_{diff} scales as D^2 (Eqn. 4.14), such that larger craters take longer to erase in proportion to their area. The equilibrium size-frequency distribution of observed craters in this range of α is therefore proportional to $D^{2-\alpha}$. Thus, the production function can be recovered even after equilibrium has been achieved at all scales. This result is significant in that it is traditionally assumed that the equilibrium size-frequency distribution follows D^{-L} for all values of $\alpha > L$, as in the previous case *Melosh* (1989); *Richardson* (2009). However, *Soderblom* (1970) notes that his analytical model breaks down at $\alpha = 4$ (for $L = 2$) once the smallest craters begin to dominate diffusion, consistent with the results presented here.

The small-crater branch of the HPF has a power law exponent of -3.82, falling in the range $L < \alpha \leq L + 2$. At any given time, a particular size of crater, D_{cov}, has had just enough time to cover the domain once, and D_{cov} first coincides with the smallest craters (of size D_{min} in the cratered terrain model, but effectively infinitesimal in the case of the Moon) and subsequently moves to larger diameters with time. Given the coefficient in Equation 4.19, D_{cov} can be calculated by comparing the segmented lunar size-frequency distribution to D^{-L}, which represents the maximum observable number of craters of that size. The number of craters per unit area on the Moon is given as $10^{-2.616}D^{-3.82}$ (Eqn. 4.19). Multiplying by the area of each crater ($\frac{\pi}{4}D^2$) and setting the result to 1 yields an estimate of the maximum crater size that has completely covered the surface:

$$10^{-2.616}D_{\text{cov}}^{-3.82}\frac{\pi}{4}D_{\text{cov}}^{2} = 1. \tag{4.20}$$

For small craters, $D_{\text{cov}} = 32$ m. All craters smaller than this have also covered the entire surface at least once, but larger craters have not. This simple calculation is roughly consistent with crater counts down to smaller diameters than those included in the HPF, which indicate a cumulative size-frequency distribution slope of -2 for craters less than 100 m in diameter (*Shoemaker et al.*, 1970; *Soderblom*, 1970; *Hartmann*, 1985; *Namiki and Honda*, 2003).

4.4 Model Comparisons with LOLA Data

The Lunar Orbiter Laser Altimeter (LOLA) is a multibeam laser altimeter carried on the Lunar Reconnaissance Orbiter (LRO) that has collected over 6.3 billion measurements of lunar surface height since 2009 (*Barker et al.*, 2014). Along-track measurements with a vertical precision of ∼10 cm and accuracy of ∼1 m are spaced approximately 57 m apart (*Smith et al.*, 2010a), and this high density provides an ideal opportunity to determine the power spectral density of lunar topography and compare the result to the PSDs generated using our cratered terrain model.

The data were processed to remove anomalous data points (due to instrumental effects), binned along track in overlapping windows, and interpolated to a constant spacing. Windows with many consecutive missing points were excluded from the analysis to avoid introducing artifacts in the PSD. After demeaning and detrending the profiles, the PSD was estimated within each window using the same multi-taper algorithm as previously in section 4.2.1, using 4 standard filters to accommodate the non-periodic nature of the profiles. The choice of window size is important in measuring the power spectral slope, and after considering a wide range window sizes, we found the rule described by *Shepard et al.* (2001) pertaining to Hurst exponent estimations to be applicable here as well. Measuring the PSD slope over a given range of spatial scales (inverse frequency) requires that the topographic profile length (window size) be no less than 10 times the maximum scale considered.

We use a least-squares linear fit to measure the log-log slope of the PSD in two frequency ranges: the first samples topographic scales ranging from the smallest scale accessible with the LOLA data (twice the shot spacing, or roughly 115 m) to 1 km, and the second captures scales ranging from 1 to 6 km. Figures 4.10 and 4.11 contain maps of the PSD slope in each of these frequency ranges. The small-scale PSD slope (Fig. 4.10) was calculated in 1-degree (∼30-km) windows, while the few-kilometer-scale PSD slope (Fig. 4.11) used 3-degree (∼90-km) windows. In both cases the windows were spaced 0.1 degrees (∼3 km) apart.

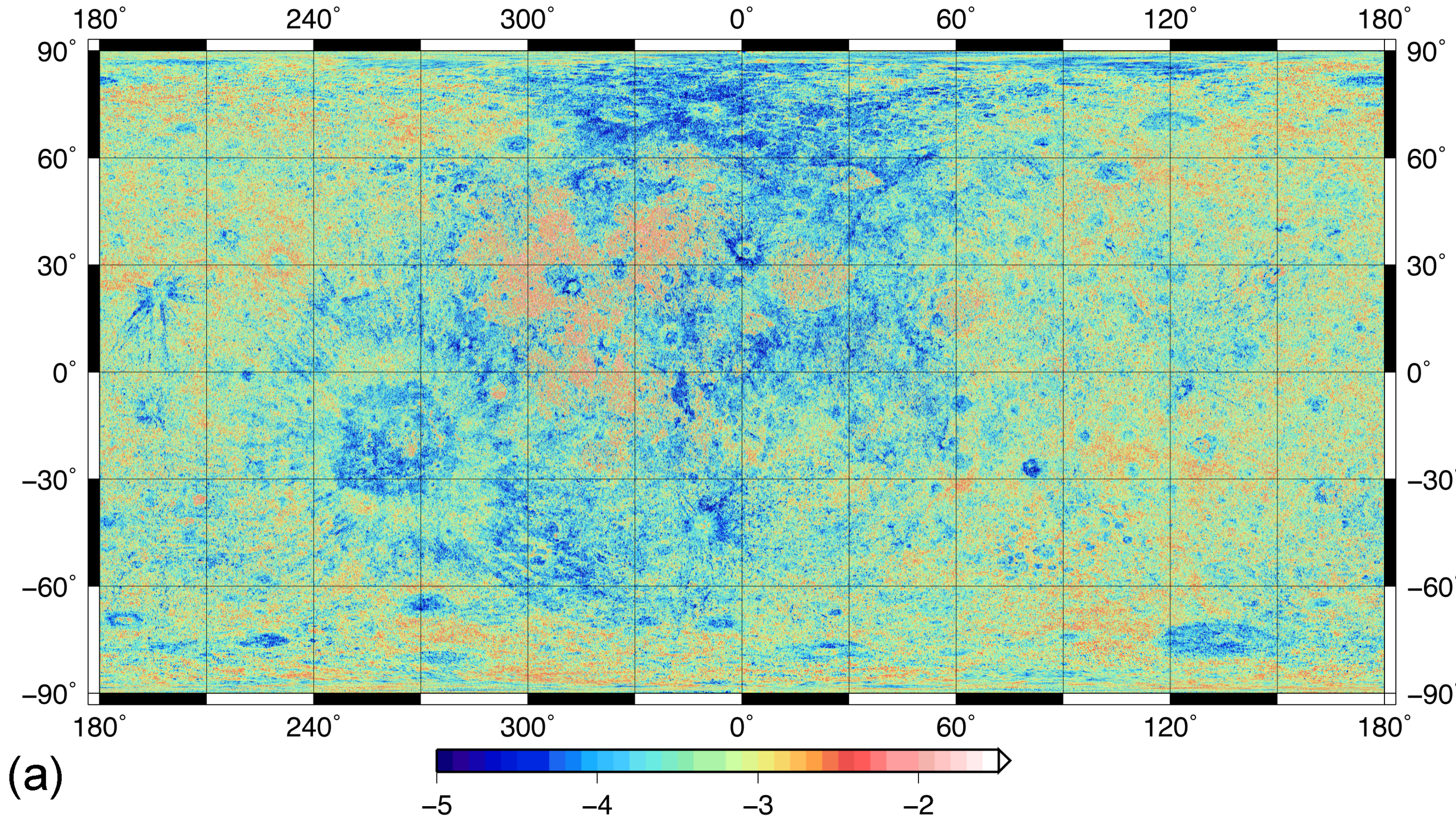

Figure 4.10: PSD slope (β) estimated for scales in the range of $\sim$ 115 m to 1 km in overlapping windows of 1° ($\sim$ 30 km), spaced 0.1° ($\sim$ 3 km) apart.

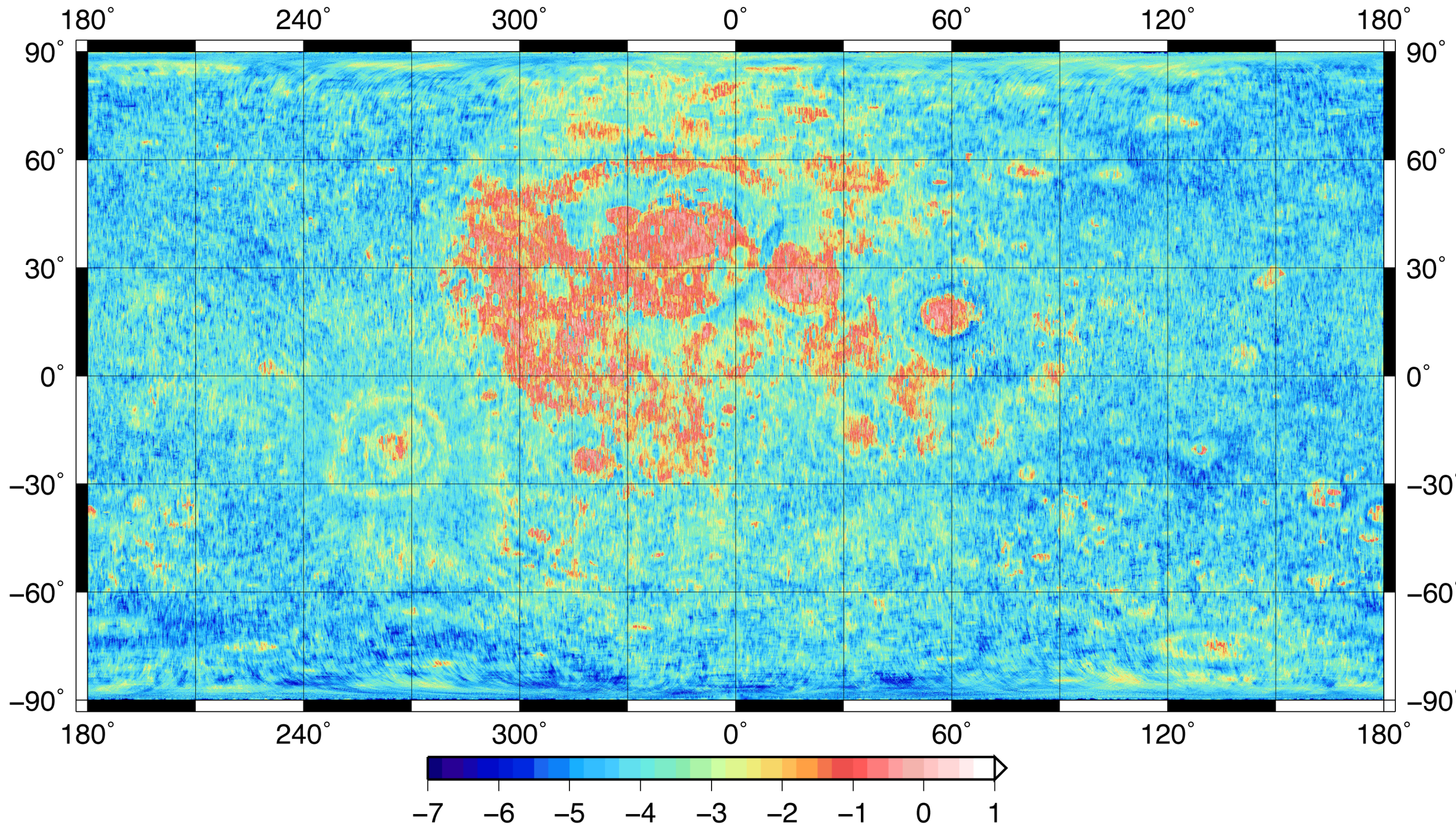

Figure 4.11: PSD slope (β) estimated for scales in the range of ~ 1 to 6 km in overlapping windows of $3°$ (~ 90 km), spaced $0.1°$ (~ 3 km) apart.

4.5 Discussion

At small scales (~ 115 m to 1 km, Fig. 4.10), $\beta \sim 3$ in the heavily cratered highlands, in reasonable agreement with the model for a value of $\alpha \sim 3.82$ (Eqn. 4.19) and when taking into account the effects of inheritance on resetting the terrain. The boundary between the maria and the highlands is indistinct, indicating that at these scales ($\sim$115 m to 1 km) the regions are comparably rough, a result that agrees with those of other recent studies of lunar surface roughness (*Rosenburg et al.*, 2011; *Kreslavsky et al.*, 2013). *Kreslavsky et al.* (2013) attribute this observation to the globally isotropic processes of regolith accumulation and modification, which produce and support roughness features on hectometer scales. Regions with significantly steeper PSD slopes ($\beta > 3$) occur in the floors of some large craters, where the topography is dominated by central peaks, rim terraces, and slump deposits on kilometer scales, a lengthscale that corresponds to the minimum frequency in the range sampled here. The most obvious example can be found in the floor of the crater Humboldt (27.2°S, 80.9°E), which is dominated by a complex rille network and range of central peaks (Fig. 4.12). Similarly, the ring structure of Orientale Basin has a generally steeper PSD slope than the surrounding ejecta blanket, most likely due to prominent kilometer-scale topographical features.

Crater ray systems are also easily discernible as regions of higher β (appearing blue in Fig. 4.10), suggesting that while they are not prominent in the raw elevation data, they do contain a unique topographical signature. In this case, it is likely that the rays have removed roughness at small scales relative to large ones (in this case, 115 m *vs.* 1 km), producing a power spectral density profile that is depressed at the high frequency end, and thus steeper than in the surrounding terrain. This steepening of the PSD may also be due in part to kilometer-scale chains of secondary craters which add power to the larger scales considered. *Rosenburg et al.* (2011) found a similar result in their differential slope analysis, showing that crater ray systems are more smooth at the shortest scales accessible with LOLA ($\sim$57 m) relative to kilometer scales than the rest of the highlands, while *Kreslavsky et al.* (2013) observed a similar effect using a related roughness measure, the curvature of topographic profiles. Prominent ray systems belong to Tycho (43.31°S, 11.36°W), Jackson (22.4°N,

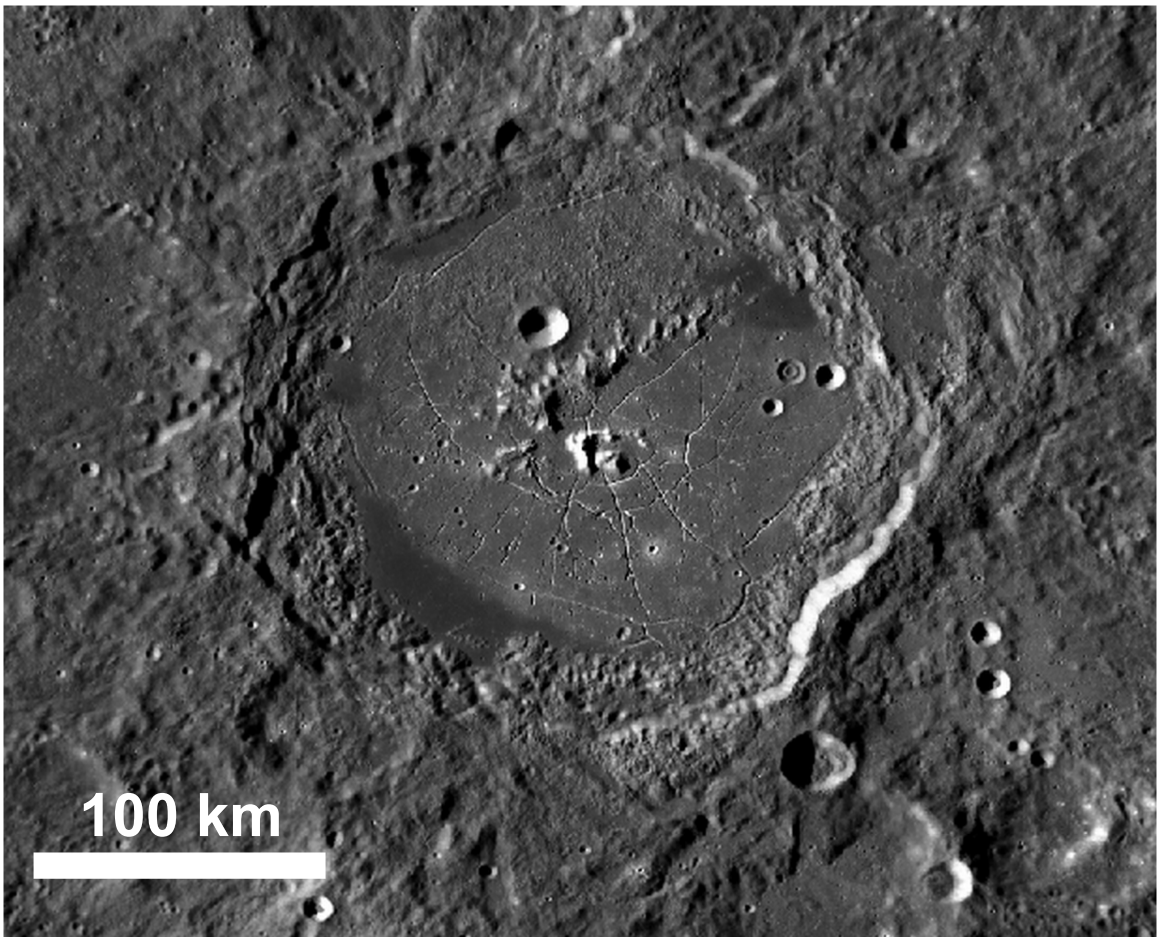

Figure 4.12: Lunar crater Humboldt, shown in the LROC Wide Angle Camera (WAC) mosaic (resolution of 100 m/pix), in an orthographic projection centered at 27°S, 81°E.

163.1°W), and Ohm(18.4°S, 113.5°W), the youngest craters of their size (*Kreslavsky et al.*, 2013; *Hiesinger et al.*, 2012; *van der Bogert et al.*, 2010), as well as Aristillus (33.9°N, 1.2°E), Vavilov (0.8°S, 137.9°W), and Aristarchus (33.9°N, 1.2°E). No clear progression in the value of β is evident with age as *Kreslavsky et al.* (2013) suggest, although the slope of the PSD is not directly comparable to their surface roughness measure, which (for these features) looks at the 115-m scale only, the lower limit of the PSD range shown here.

Several localized areas of relatively shallow PSD slope ($\beta \sim 2 - 2.5$) occur in the interiors of the large mare-filled basins and as halos around prominent impact craters in the lunar highlands. A smaller value of β indicates a relatively greater contribution to the PSD from smaller scales compared to larger ones. In these cases, several factors may be at play. In the maria, crater saturation has likely not taken place for craters larger than approximately $D \sim 100$ m (*Richardson*, 2009), and there may be places that have not been completely covered by craters since the emplacement of the mare basalts. The absence of crater overlap in this case, together with the limited time available since the surface was reset for larger craters to accumulate, may have resulted in a dearth of topographical features contributing to the low-frequency end of our frequency range and a consequent shallowing of the PSD slope. The regions of relatively low β surrounding prominent craters may be due not to an absence of power at large scales, but rather an addition of small scale features, especially rim terraces and blocky ejecta deposits. Haloes of this nature were also noted by *Kreslavsky et al.* (2013) at the 1-km scale, where ejecta transitions from proximally smooth to distally rough. Similar cases, where small-scale roughness is low near the crater rim (with values of $\beta \sim 4$) and becomes relatively high further away ($\beta \sim 2$), include the farside craters Fermi (19.3°S, 122.6°E) and Kovalevskaya (30.8°N, 129.6°W).

Figure 4.11 contains shows the PSD slope measured at somewhat larger scales, spanning the range from 1 to 6 km. Whereas the maria and highlands were not easily distinguishable in the small scale PSD shown in Figure 4.10, here they are quite distinct, with the maria displaying much lower PSD slopes ($\beta \sim 1$) than the highlands ($\beta \sim 3.5 - 4$). This difference reflects the absence of features at the few-kilometer scale in the maria, aside from prominent wrinkle ridges and decameter-scale craters, which appear as isolated spots of higher β.

This stark contrast between the maria and the highlands is characteristic of lunar roughness above and below approximately kilometer scales. *Rosenburg et al.* (2011) noted that the Hurst exponent—a measure ranging from 0 to 1 that describes the scaling of surface slopes with horizontal baseline—transitions in the highlands from approximately 1 (indicating nearly self-similar behavior) at small scales to a smaller value of approximately 0.8, with the transition occurring near 1 km. Similarly, *Kreslavsky et al.* (2013) found a clear difference in the character of lunar surface roughness at hectometer and kilometer scales. This behavior is consistent with a transition between roughness regimes controlled by competing surface processes acting at different scales, including the accumulation of regolith through impact gardening processes, the global erasure of roughness features by seismic shaking during large basin-forming impacts, and early tectonic and volcanic events that formed the prominent mare plains and wrinkle ridges (*Rosenburg et al.*, 2011; *Kreslavsky et al.*, 2013; *Richardson*, 2009).

4.6 Conclusions

We have developed a model capable of tracking the evolution of a cratered terrain from an initially flat plane through saturation equilibrium. Having benchmarked the model against an analytical solution in 1D, we conclude that the power spectral density of a surface created only by impacts can be predicted from the size-frequency distribution of craters emplaced. In comparing the results of the model to calculations of the PSD along LOLA transects, we find good agreement at small scales down to 115 m. Exceptions to the model occur in places where competing geomorphological processes, such as tectonics, dominate, or when crater saturation has not yet been achieved. The model predicts behaviors for the PSD slope β at a range of size-frequency distribution exponents (α), not all of which can be tested with the lunar topography. Impact cratering is a dominant agent of surface modification in our solar system, and it is hoped that the conclusions drawn here can be applied to many planetary surfaces, including those of Mercury, Mars and the outer planet satellites.

Chapter 5

Understanding Geometric Bias in Crater Counts

5.1 Introduction

The size-frequency distribution of craters on a planetary surface is a key measurement in quantifying certain properties of that surface, including its relative age as well as the size distribution of impactors responsible for creating it. In particular, the Moon has remained an important object of study in this respect both because its relative proximity allows for detailed examination of the surface by ground observers and spacecraft and because its heavily cratered surface provides a natural laboratory for examining a range of impact processes and radiometric dating of returned Apollo samples provide an absolute calibration for the timescale. Furthermore, understanding the crater distribution on the Moon provides crucial information as to the impactor flux on other planetary bodies, allowing for correlation of geological epochs across the solar system. As such, the distribution of craters on the lunar surface has been the topic of considerable attention by researchers throughout the twentieth century, especially in the decades following the return of the first images obtained by orbiting spacecraft, the preparation of geological maps of the Moon, and subsequent lunar missions returning image and topography data at ever higher resolution and precision (*Hartmann*, 1985; *Chapman and McKinnon*, 1986; *Melosh*, 1989; *Ivanov et al.*, 2002; *Neukum et al.*, 2001; *Richardson*, 2009).

Many measurements of the size-frequency of lunar craters have been made throughout the last few decades (*Neukum et al.*, 2001; *Ivanov et al.*, 2002), almost always by human researchers identifying crateriform structures by eye, and crater counting remains an important tool for planetary scientists. However, translating between the distribution of currently visible craters and the underlying distribution of craters that were actually emplaced may not be entirely straightforward. For example, *Robbins et al.* (2014) describes recent work to integrate results from the citizen science project CosmoQuest Moon Mappers (http://www.cosmoquest.org), which allows members of the public to contribute to crater counts on the lunar surface using high-resolution images from the Lunar Reconnaissance Orbiter Camera (LROC). Comparison of expert and non-expert crater counts shows that while the derived crater distributions overlap, variability among the features identified is large, even among experts using a variety of software tools and methods. No two people will identify the same set of circular features in an image, especially in dense regions where crater overlap is common (*Robbins et al.*, 2014). At the same time, automated crater identification is numerically challenging, particularly on real surfaces containing traces of multiple geologic processes, and cannot yet compete with human observations in terms of accuracy. Understanding the statistical variations among crater counters, as well as the systematic biases affecting them, is therefore essential in order to further quantify lunar size-frequency distributions useful for relative age dating of surfaces and constraints on the impactor population responsible for producing them.

One such systematic bias was first noted by *Mullins* (1976) in his analysis of the stochastic crater model proposed and subsequently elaborated by *Marcus* (1964), *Marcus* (1966c), *Marcus* (1966b), *Marcus* (1966a), *Marcus* (1966d), and *Marcus* (1967), in which an assumption of non-saturation conditions had to be made in order to successfully analyze the statistics of the crater distribution (*Mullins*, 1976). In particular, *Marcus* (1964) derives an estimate of crater density as a function of time for pristine craters, those whose rims are completely intact, while *Marcus* (1966c) attempted to treat craters for which any portion of the rim is visible, but effectively had to limit his analysis to regions of little to no overlap to solve the equations. As *Mullins* (1976) points out, the choice of criterion determining which features are "visible" in regions of significant overlap has a large effect on the resulting size-frequency distribution of craters because large craters tend to be overcounted compared to small ones. This geometric bias was explored further by *Woronow* (1978), who used a numerical model to track rim points through time, although his model was criticized by *Chapman and McKinnon* (1986) because it used only 8 rim points to define each crater and could accommodate a dynamic range in crater sizes of only 16. Subsequent work (*Woronow*, 1985a,b) addressed these concerns and confirmed the existence of the geometric bias.

The cratered terrain model developed in the previous chapter has a rim-tracking feature that allows it to account for the surviving rim fragments of each emplaced crater through time for a large number of rim points and range of crater sizes (Fig. 5.1). This chapter first explores this numerical approach, then compares the results to those of *Mullins* (1976), *Marcus* (1964), *Marcus* (1966c), and *Woronow* (1985b), and finally assesses the implications for current crater counting efforts on the Moon and other planetary bodies. Our approach improves upon the previous works described in several respects, most notably in that it tracks the 3-dimensional evolution of the topography simultaneously with the surviving rim segments of each crater emplaced, and applies considerably greater computing power to maximize both the dynamic range of craters used and the resolution of each crater's rim.

5.2 Criteria for "Visible" Craters

The human eye is adept at identifying craters, even when they overlap or are otherwise partially obscured. Nevertheless, there are some limits beyond which a degraded crater cannot be recognized as such by a human researcher. These limits are likely a combination of many factors, including the remaining rim fraction and the connectedness of rim arcs, and may differ depending on dataset properties such as illumination angle, resolution, and the availability of topographic information. There is no consensus opinion among researchers on the ideal criterion for defining the "visibility" of craters on a model-generated terrain. *Mullins* (1976) and *Woronow* (1985b) choose the remaining rim fraction as a proxy for crater survival, whereas *Richardson* (2009) tracks the area of each emplaced crater through time, factoring in destructive processes such as infilling by slope failure and regolith gardening in addition to crater overlap. Because the rim itself is essential both to identifying

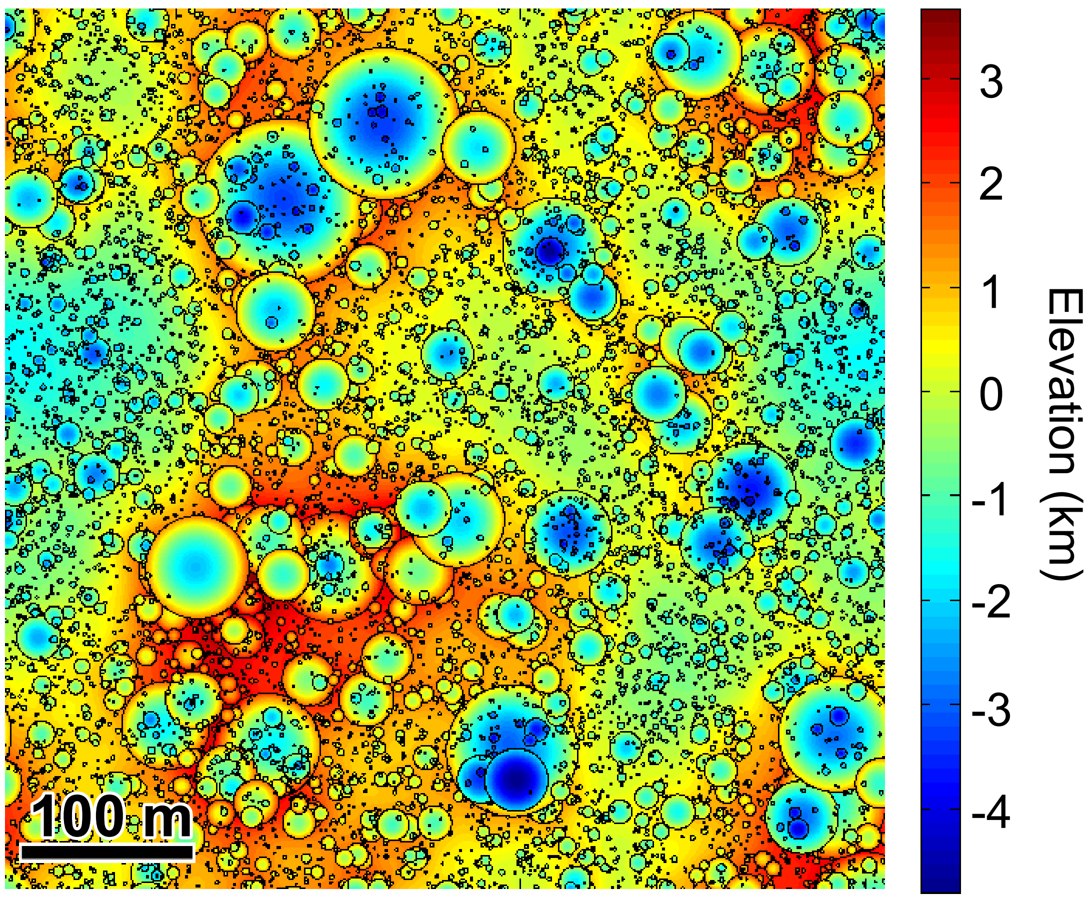

Figure 5.1: Sample topography (color scale) generated by the cratered terrain model described in the previous chapter with surviving rim fragments overlain (black).

craters—due to the sharp relief it provides in images and to the unique circular character it displays—and to measuring their diameters, we follow the former approach. This choice is supported by *Robbins et al.* (2014), in which several crater experts discussed using the sharp, circular transition from light to dark to identify craters. The fraction f_{vis}, ranging from 0 to 1, is defined as the minimum fraction of rim remaining such that a crater can be classified as "visible." Fresh craters are pristine, with $f_{\mathrm{vis}} = 1$, and over time this value decreases as subsequently-emplaced overlapping craters remove all or part of the rim. Craters with rim fractions less than f_{vis} are deemed "invisible" and are thus discounted in the resulting size-frequency distribution.

5.3 Cratered Terrain Model

5.3.1 Rim Tracking

The cratered terrain model introduced in the previous chapter emplaces craters on a flat plane with diameters selected according to a cumulative size-frequency distribution:

$$N_{\mathrm{cum}} \propto D^{-\alpha}, \tag{5.1}$$

'where N_{cum} is the number of craters greater than or equal to diameter D_A, and α is the size-frequency distribution exponent. While observed size-frequency distributions of lunar craters are more complicated than a single power law (*Neukum et al.*, 2001; *Ivanov et al.*, 2002), they can often be treated as piecewise power law segments in specific diameter ranges. Understanding the fundamental effects of overlap in this simplified case can therefore provide useful insights into more complex distribution functions as well.

Each incoming crater is assigned a diameter, a random location, and a set of rim points that are tracked throughout the remainder of the simulation. The number of rim points can be specified in two ways, either by fixing the spacing between rim points or fixing the number of points defined for each crater directly. The former method allots more rim points for larger craters than smaller ones, and the spacing is therefore determined by the circumference of the smallest crater included in the model, of diameter D_{min}. Directly fixing the number of rim points per crater allows for greater precision in rim fraction for the smallest craters, but adds a very large number of points to the total simulation, requiring additional computation time. The fixed rim point spacing method is therefore preferred, with the provision that the minimum number of points per crater be sufficient to resolve the surviving rim fragments of the smallest craters. No fewer than 30 rim points were used for any craters in these simulations.

As subsequent craters overlap and obliterate an existing crater, an algorithm determines which previously-existing rim points fall within the polygon defined by the rim of the new crater, and these are removed from the simulation. For each crater, the fraction of rim remaining unscathed is easily tracked as a function of time, where "time" is parameterized as the number of craters that have been emplaced. Figure 5.1 shows an example of topography generated by the cratered terrain model with the surviving rim fragments of the emplaced craters overlain as black ring segments. The stratigraphic relationships between craters emplaced at earlier and later times are clearly visible in the interrupted arcs and complete circles, respectively.

Once a value for the criterion f_{vis} is selected, a size-frequency distribution of "visible" craters can be computed at any given time during the model run. A low value of f_{vis} equates to a loose criterion for visibility—only a small portion of the rim need be present to identify the crater and include its diameter in the size-frequency distribution. A high value, on the other hand, denotes a strict criterion; most of the crater rim must be extant in order to identify it.

5.3.2 Erasure by Ejecta Emplacement

One criticism of *Woronow* (1978) concerned the lack of ejecta effects in his model (*Chapman and McKinnon*, 1986). Crater rims may be erased by superimposed ejecta as well as direct obliteration by overlap. To address this issue, *Woronow* (1985a) employed two ejecta schemes, one of which increased the effective diameter of each incoming crater when considering rim erasure, and the other of which calculated the thickness of an exponentially-decaying ejecta blanket in order to identify obscured rim points. He found that the two models produced results in good agreement when the

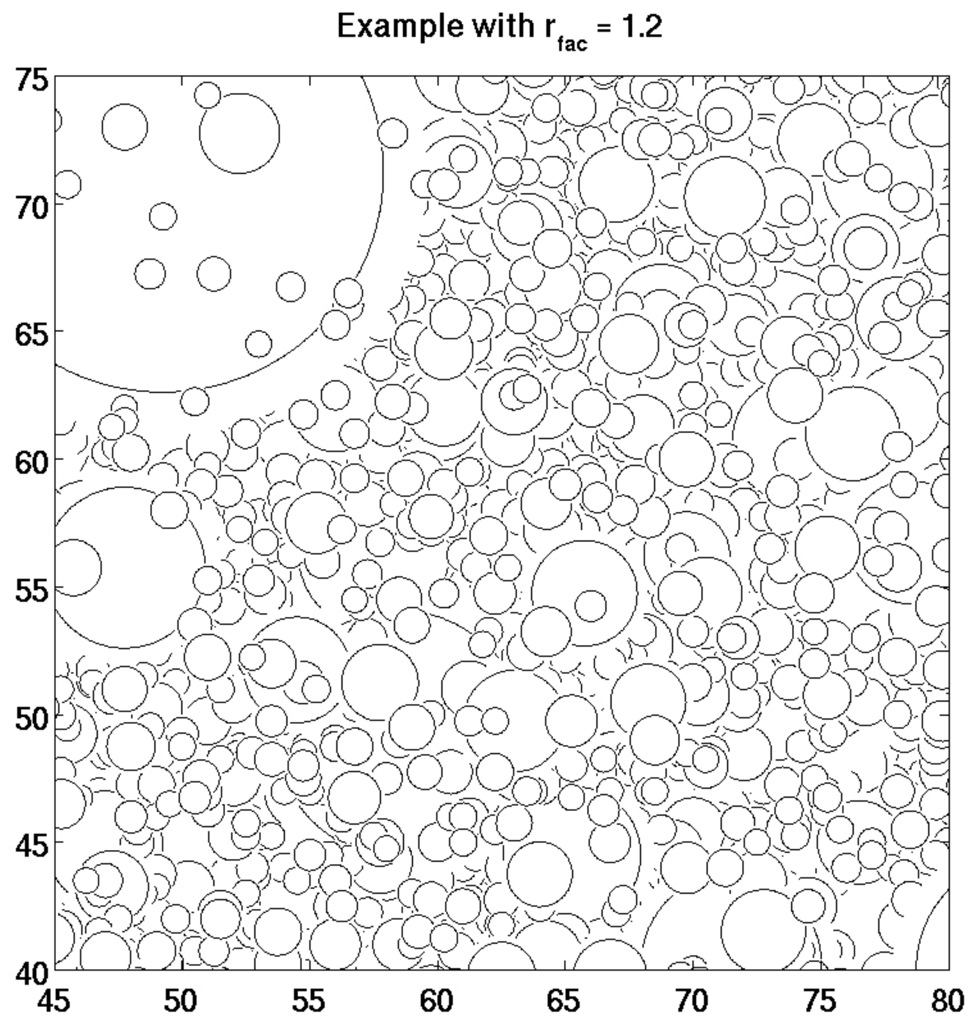

Figure 5.2: Portion of a model terrain showing overlapping rim fragments with $r_{\text{fac}} = 1.2$. Each incoming crater erases a circular area with a diameter 20% larger than the crater diameter.

diameter of an incoming crater of size D was increased by a factor of $1.1D$ for the purposes of rim erasure. The cratered terrain model presented here also allows for adjustments in this manner, using the multiplicative parameter r_{fac} to control the extent of erasure beyond the emplaced crater rim. A value of $r_{\mathrm{fac}} = 1$ reverts to the "cookie-cutting" case described thus far, while higher values indicate the extent of the ejecta blanket's capacity to obscure rim points of pre-existing craters. For example, a crater of size $D = 10$ km with $r_{\mathrm{fac}} = 1.2$ will remove rim points within 6 km of the crater center while adding its own rim points in a ring 10 km in diameter. Figure 5.2 shows a portion of a simulation using $r_{\mathrm{fac}} = 1.2$. An annulus with diameter 20% larger than the crater diameter extends around each new feature, clearly illustrating the difference between the area erased and the rim points added.

5.4 Model Results and Observations

5.4.1 Craters of One Size

Simulations were first performed with identical craters of diameter D_A to illustrate the effect of choosing different values of f_{vis}, before turning to the more complicated case including many crater sizes. This case is described theoretically by *Melosh* (1989), based in part upon sandbox experiments performed by *Gault* (1970) with a variety of projectiles and explosives. In the latter study, *Gault* (1970) defines the concept of geometric saturation, equivalent to the density of craters achieved in a hexagonal closest-packing arrangement with no overlap. This configuration results in a number density of

$$N_{\mathrm{s}} = 1.15D^{-2}. \tag{5.2}$$

Equivalently, 90.5% of the surface area is covered by craters in the closest-packing arrangement. As the surface accumulates randomly-placed craters, they will overlap each other, and the fraction of area ever covered by at least one crater will increase, surpassing 90.5% at a somewhat higher crater density than N_{s} due to overlap:

$$N_{90.5\%} \sim 2.6 N_{\mathrm{s}}. \tag{5.3}$$

At this point, which *Gault* (1970) terms the "saturation time," the number density of observable craters departs from the production function and the surface approaches equilibrium: any incoming crater of size D_A will, on average, erase an existing crater of that size. The number density of craters thus increases approximately linearly from zero until an equilibrium value is reached, and then remains constant with small fluctuations depending on the arrangement of overlapping craters at any given time.

Crater densities for different choices of f_{vis} are presented in Figure 5.3 for a model using only craters with diameter $D = 20$ km on a domain of size $X = 128$ km. The density at geometric saturation for this diameter is $N_{\mathrm{s}} = 0.0029$, and this value is marked in the figure. In general, crater density behaves as expected, increasing linearly at the beginning of the simulation and leveling to a constant approximately when 90.5% of the the domain is first completely covered by craters. For this simulation, the saturation time (in terms of number of craters emplaced) can be calculated as:

$$N_{90.5\%} X^2 \sim 2.6 \cdot 1.15 D^{-2} X^2 \sim 123 \text{ craters}. \tag{5.4}$$

After one saturation time, the number density of craters fluctuates around an equilibrium value, dropping abruptly when large craters clear a broad area and climbing again as smaller craters accumulate.

As is clear from Figure 5.3, the choice of f_{vis} has a significant influence on the equilibrium crater density. Using the lowest value shown, $f_{\mathrm{vis}} = 0.1$, results in a final density nearly 2.5 times that at geometric saturation. With such a loose criterion for "visibility," many more overlapping craters can be included than in a closest-packing configuration. On the other hand, using the strictest criterion, $f_{\mathrm{vis}} = 1$ (pristine craters), reduces the crater density by an order of magnitude. The equilibrium crater density remains below geometric saturation only for values of $f_{\mathrm{vis}} > 0.4$. These differences in crater density are easily seen in Figure 5.4, which highlights "visible" craters (shown in blue) on the

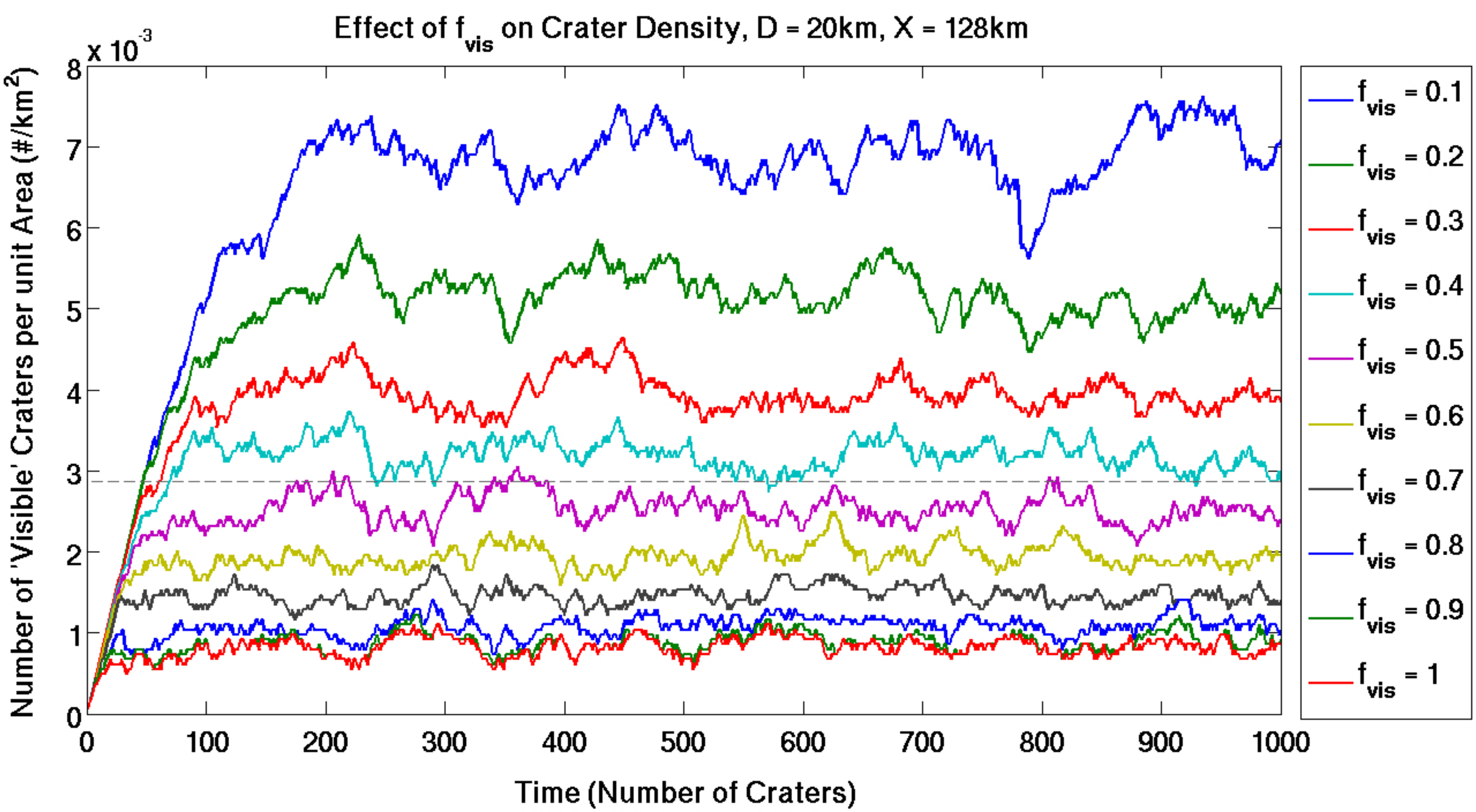

Figure 5.3: Crater density as a function of time (craters emplaced) for different choices of the criterion for "visible" craters, f_{vis}. The domain size is $X = 128$ km and all craters are of diameter $D = 20$ km.

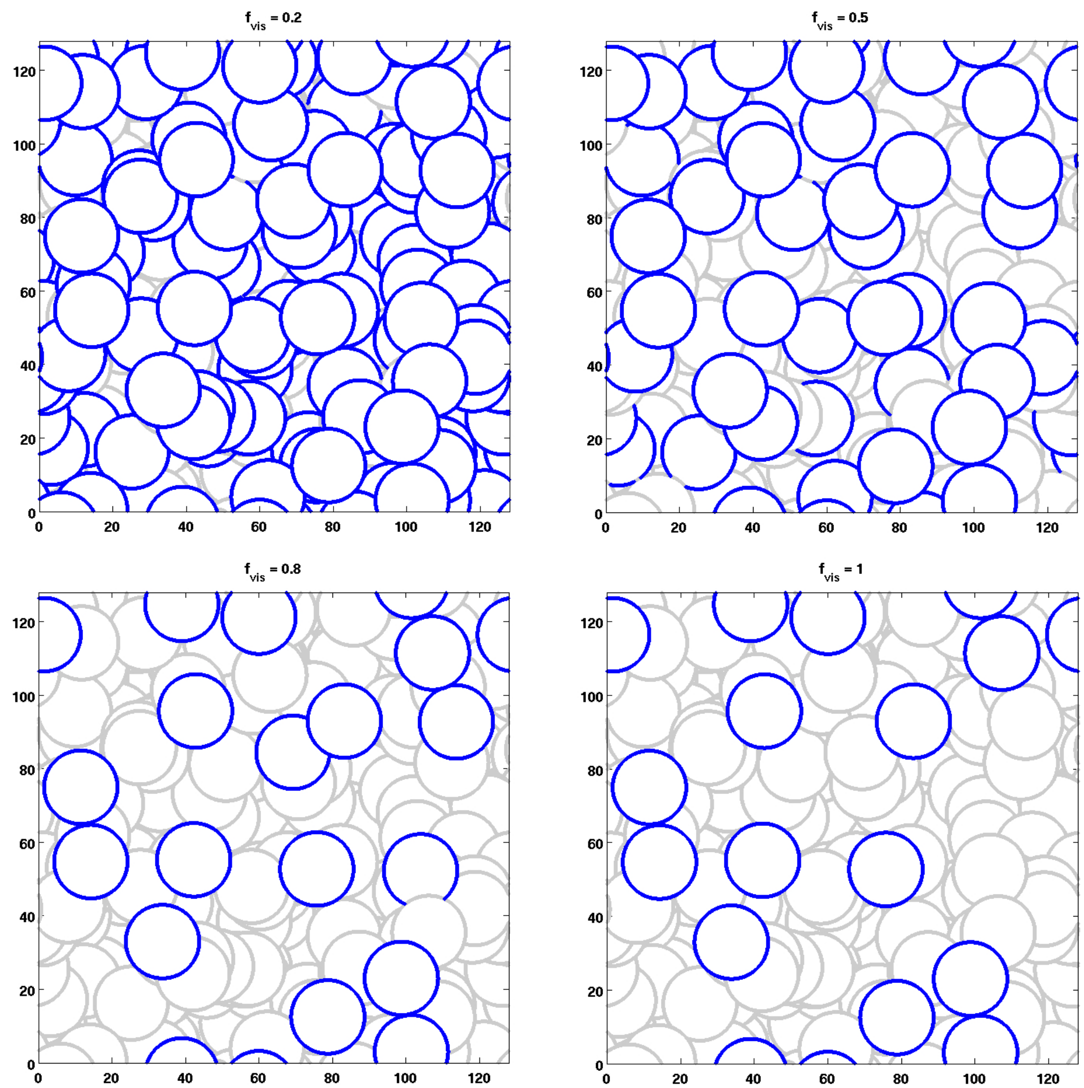

Figure 5.4: Surviving rim points for the single-size crater simulation (gray) highlighting "visible" craters for different values of f_{vis} (blue).

same domain for several different values of f_{vis} against a background of all surviving rim fragments (shown in gray).

The simulations shown in Figures 5.3 and 5.4 were run in "cookie-cutting" mode, with $r_{\text{fac}} = 1$. As expected, increasing r_{fac} reduces the crater density for all values of f_{vis}, as every new crater is able to erase a larger area than the footprint bounded by the rim. For $r_{\text{fac}} = 1.2$, crater density remains below geometric saturation for values of $f_{\text{vis}} > 0.2$, and the pristine-crater case ($f_{\text{vis}} = 1$) yields an equilibrium crater density of approximately 20% that at geometric saturation. That the lowest equilibrium densities modeled here are still much greater than the observed crater densities on planetary surfaces indicates that other erasure processes are also important in modifying crater distributions. For this reason, the term *equilibrium* is often used specifically to take into account the interaction of all geologic processes, while *saturation* is used to refer to the impact cratering process alone.

5.4.2 Multiple Crater Sizes: Geometric Bias

For a given production function of craters (characterized by size-frequency distribution exponent α according to Equation 5.1), varying the value of f_{vis} between 0 (the most relaxed criterion) and 1 (the strictest) results in significant variation in the slope of the measured size-frequency distribution, α'. Smaller values of f_{vis} result in a shallower size-frequency distribution (smaller α'), while large f_{vis} result in large α'. An example of this behavior for a production function with $\alpha = 1.5$ is shown in Figure 5.5. The black dashed line indicates the power law exponent of the production function (α), which only coincides with the observed size-frequency distribution slope (α') for values of f_{vis} between ~ 0.4 and 0.5.

This behavior can be understood by considering the range of rim fractions that survive at any given moment within one crater size bin. Given an existing crater A of size D_A, incoming craters with randomly chosen centers will either overlap with A or miss it entirely. Assuming that new crater B of size D_B overlaps with A by some amount, there are two possible outcomes: either the new crater obliterates a section of the old crater's rim, or it covers the old crater entirely (if $D_B > D_A$).

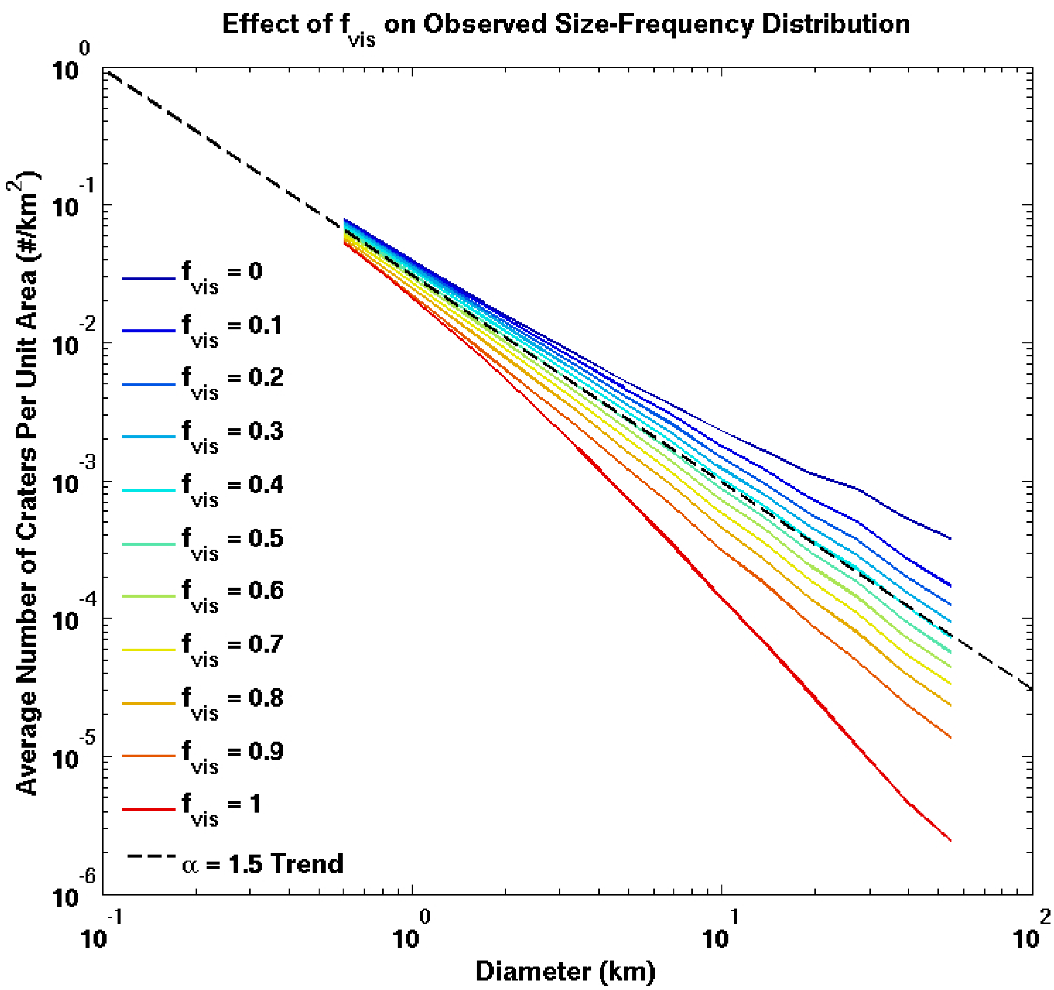

Figure 5.5: Observed size-frequency distribution as a function of f_{vis} for a simulation using $\alpha = 1.5$, $D_{\min} = 500$ m, $D_{\max} = 64$ km, and $X = 128$ km. The black dashed line indicates the slope of the production function ($\alpha = 1.5$), which coincides with the observed slope (α') only for $0.4 < f_{\text{vis}} < 0.5$.

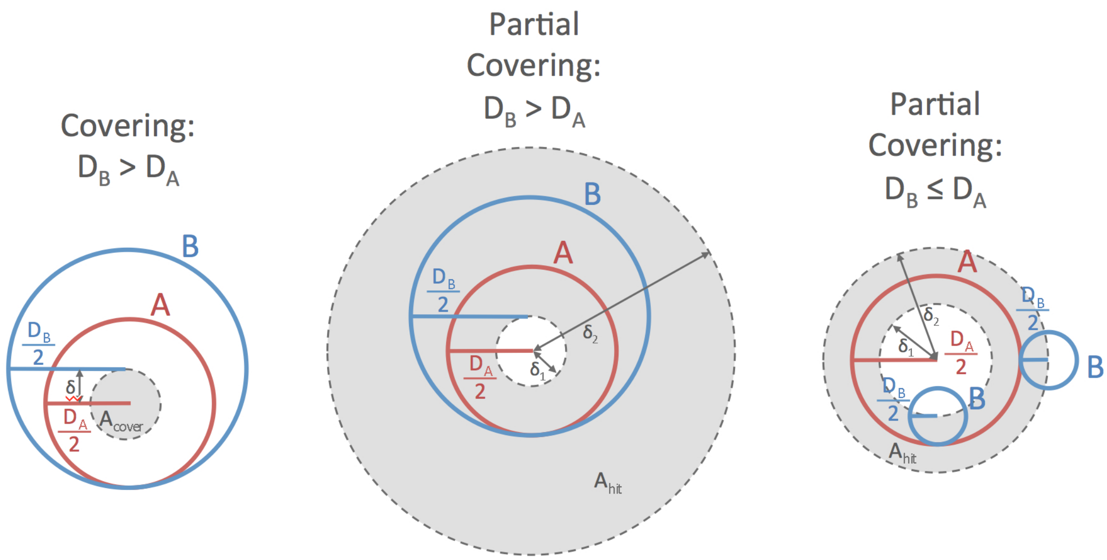

Figure 5.6: Assuming that new crater B overlaps by some amount with existing crater A, it will either cover it completely or erase only part of the rim, depending on where crater B falls in relation to A. This diagram shows the areas A_{cover} and A_{hit} within which the center of B must fall to entirely erase or partially cover A, respectively, for the two cases where the diameter of B (D_B) is larger or smaller than that of A (D_A).

The outcome is determined by where crater B falls in relation to crater A. There is a certain area, A_{cover}, within which crater B will always cover crater A. Another area exists, A_{hit}, within which crater B will cover part, but not all, of the rim of crater A. These areas are illustrated in Figure 5.6 and can be written as follows:

$$A_{\text{cover}} = \begin{cases} \pi \left(\frac{D_B}{2} - \frac{D_A}{2} \right)^2 & D_B > D_A \\ 0 & D_B \leq D_A \end{cases} \tag{5.5}$$

$$A_{\text{hit}} = \pi D_A D_B. \tag{5.6}$$

Thus, assuming that crater B overlaps crater A by some amount, the probability that it will cover the pre-existing crater completely is related to the ratio of these areas and the probability that crater B is of a given size D_B. For most crater sizes, A_{cover} is larger than A_{hit}; only craters with diameters near or less than D_A are more likely to partially cover crater A than erase it (Fig. 5.7). According to Eqn. 5.1, however, small craters are much more likely to occur than large craters, since

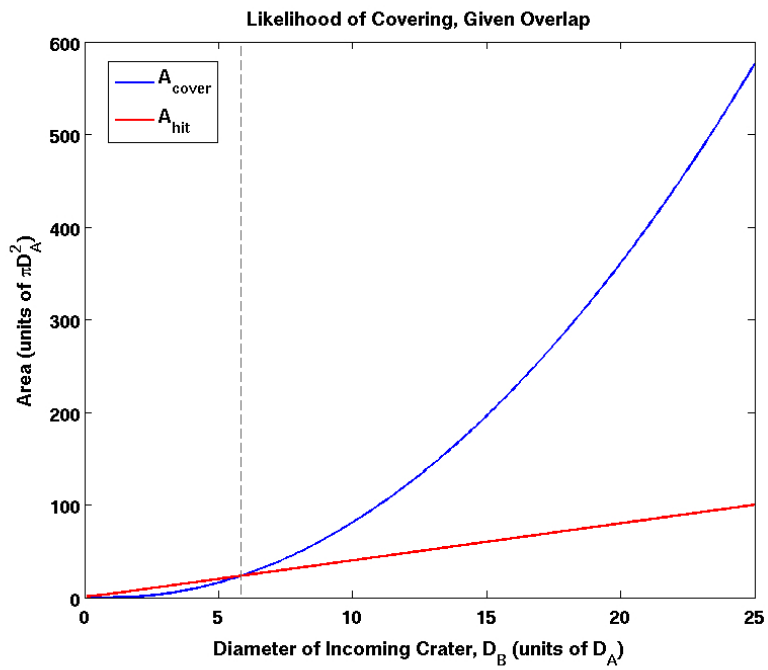

Figure 5.7: The areas A_{cover} and A_{hit} as a function of D_B, the size of the incoming crater B. Assuming that some overlap occurs, if D_B is smaller than $\sim 6D_A$, it is slightly more likely that a randomly-placed crater B will partially cover A than completely cover it (for $D_B < D_A$ complete covering is impossible). For larger D_B, it becomes increasingly more likely that B will entirely cover A.

α is always positive. Together, these constraints create variation in the distributions of surviving rim fractions across different crater sizes. Large craters are unlikely to be hit by craters larger than themselves because they are rare, and very likely to be hit by abundant small craters. Therefore, one would expect that at any given time, few large craters survive with a large fraction of their rims intact.

Small craters, on the other hand, are more likely to be hit by craters larger than themselves, and therefore much more likely to be covered completely than large craters. Thus, we would expect to find that most surviving small craters have large rim fractions remaining, because those that are hit at all are usually completely erased. Intermediate crater sizes should transition between the two end cases. Examination of the distribution of rim fractions within crater diameter bins bears out these expectations. Small craters that have not been completely erased are more likely to have large surviving rim fractions, while the opposite is true for large craters. Exceptions to this rule occur at the very largest rim fractions, where recently-emplaced craters of all sizes have not had much opportunity to be hit by subsequent craters, and at the very smallest rim fractions, where small rim fragments have avoided final erasure because they occupy a small fraction of the domain and are thus unlikely to be hit.

Using incremental values of f_{vis} and taking into account uncertainties in the linear fits, the relationship between α' and f_{vis} can be further examined for varying α, and the results of this analysis are shown in Figure 5.8. If the observed size-frequency distribution were to maintain the slope of the production function, then the curves would be flat for any value of f_{vis}. For most of the range of f_{vis}, however, α' increases linearly from approximately $\alpha' \sim \alpha - 0.25$ to $\alpha' \sim \alpha + 0.25$. This linear trend breaks down near $f_{\mathrm{vis}} = 0$, where the extremely loose visibility criterion favors large craters, and near $f_{\mathrm{vis}} = 1$, where the pristine-crater criterion favors small craters. This amplification of the geometric effects at the extremes of f_{vis} is readily apparent in Figure 5.5. As α increases, the slope of the linear trend decreases, and the effects near $f_{\mathrm{vis}} = 0$ and 1 become increasingly confined to the edges. Changing the value of r_{fac} has little effect on the α' curves, especially for values of $\alpha < 2$.

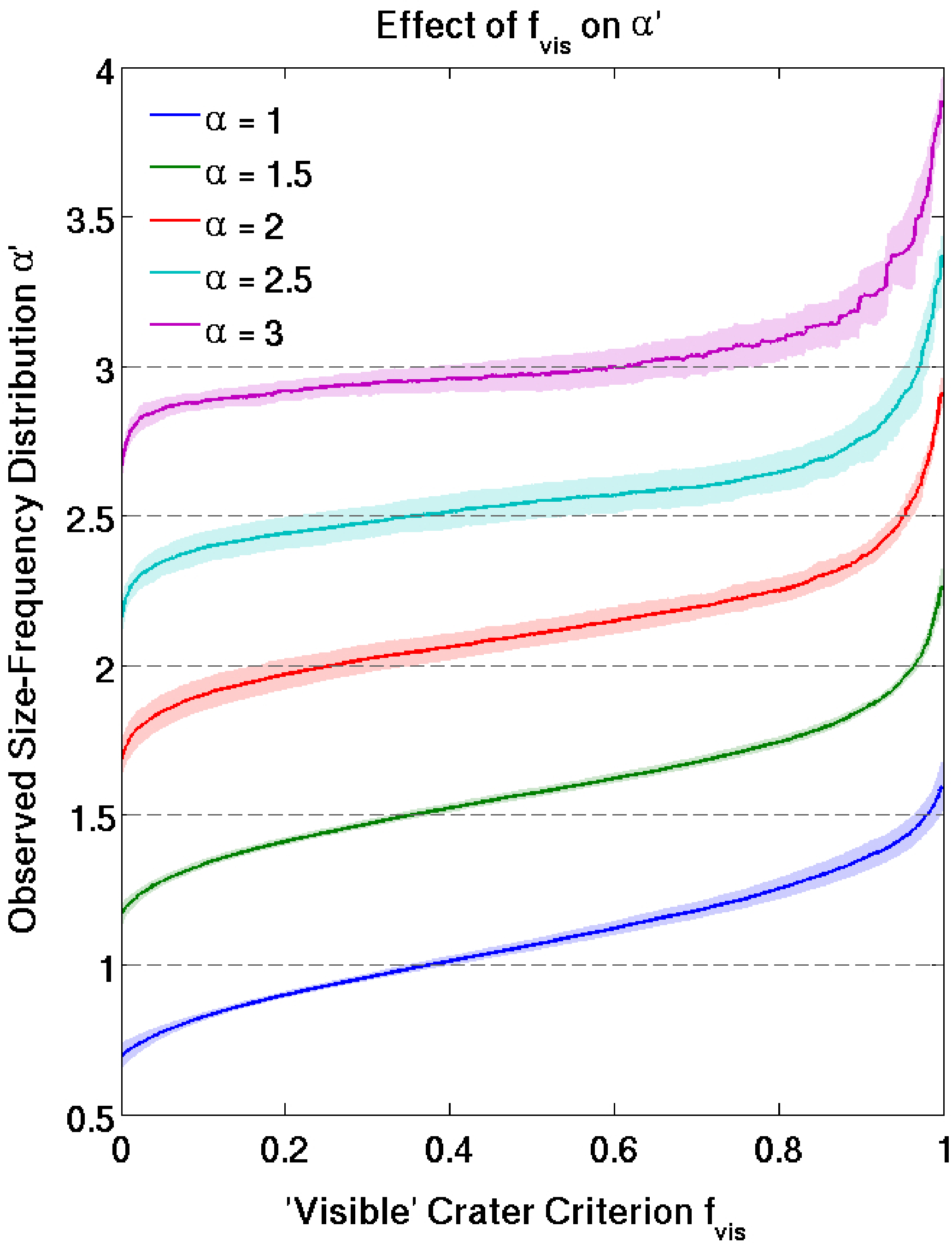

Figure 5.8: Slope of the observed size-frequency distribution (α') for different values of f_{vis}, the criterion for visibility, plotted for several production function slopes (α).

These results are consistent with those of *Woronow* (1985b), but we extend the range of f_{vis} considered and improve considerably the precision of the calculation applied to the problem. The geometric bias first noted by *Mullins* (1976) is clearly present, with large craters being overcounted at small f_{vis} and undercounted at large f_{vis}.

5.4.3 Potential Corrections

5.4.3.1 Pristine-Crater Criterion

One strategy often used by crater counters to estimate the production function is to classify features by their state of degradation and examine only the size-frequency distribution of the most pristine craters (*Chapman*, 1968; *Chapman et al.*, 1970; *Strom*, 1977). Because these craters represent the most recent features to be emplaced, it is inferred that they most closely reflect the production function. However, as Figure 5.8 shows, the pristine-crater criterion does not produce the best estimate of the underlying size-frequency distribution of emplaced craters because it tends to undercount large craters that are likely to have been partially (but not completely) covered by smaller ones. Using a value of $f_{\text{vis}} = 1$ thus results in an overestimate of α by as much as 0.5 to 1, a significant amount considering the detailed crater histories inferred from slight changes in the slope of the size-frequency distribution.

5.4.3.2 Weighting by Rim Fraction

A somewhat better method to correct for the geometric bias in crater counts was suggested by *Mullins* (1976) and *Mullins* (1978) and supported by *Woronow* (1985b). Rather than choosing the most pristine craters, which is equivalent to using $f_{\text{vis}} = 1$, *Mullins* (1976) uses a weighted histogram of "visible" craters, where the weights are given by the fraction of rim surviving for each crater. Weighting by rim fraction compensates for the overcounting of large craters at small f_{vis}. Figure 5.9 shows this correction applied to the α' curve for $\alpha = 1.5$.

While this method does adjust α' to match α at $f_{\text{vis}} = 0$, it does not correct the α' curve for higher values of f_{vis}, and for strict visibility criteria it actually exacerbates the bias toward smaller

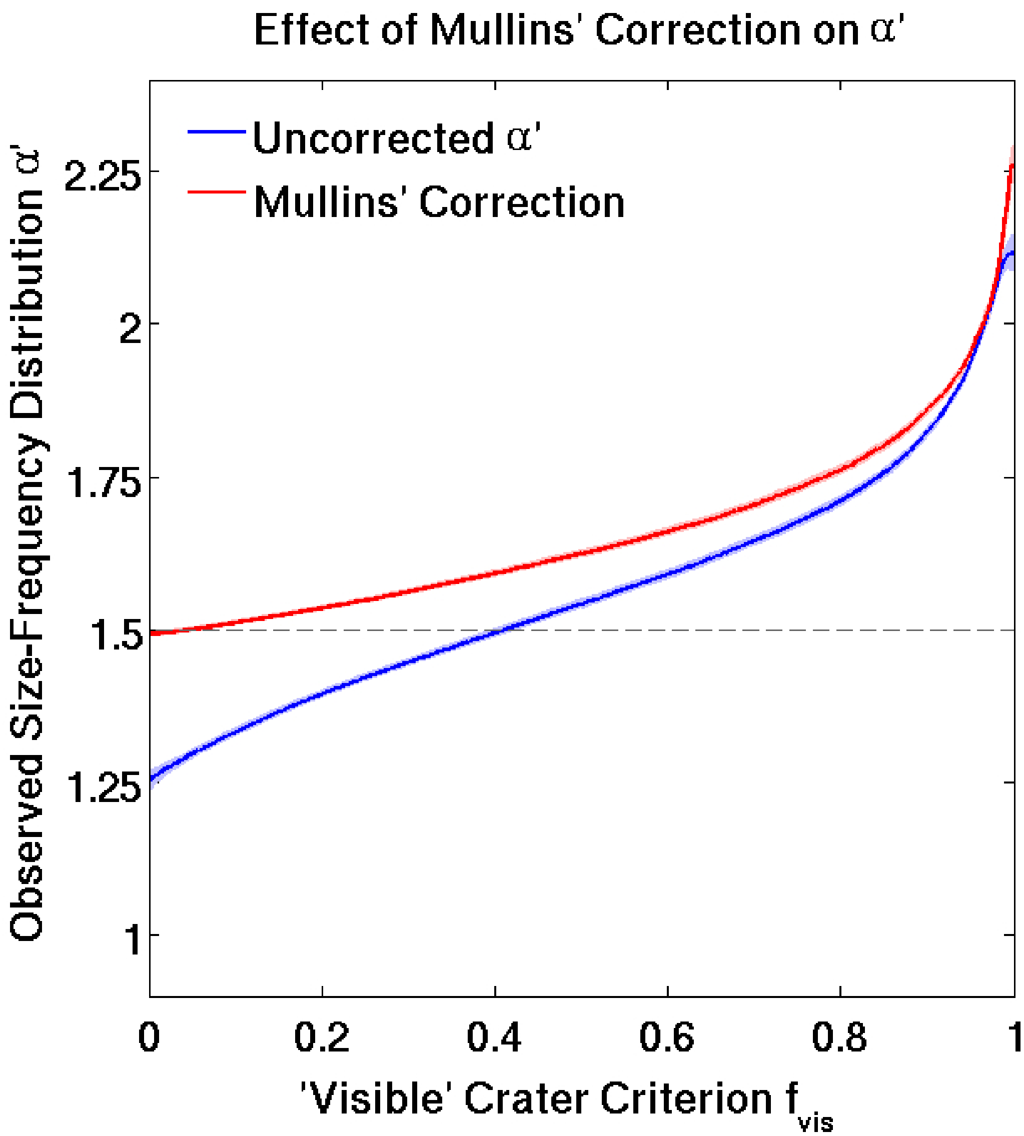

Figure 5.9: Example of the correction proposed by *Mullins* (1976), with $\alpha = 1.5$. Histograms of "visible" crater diameters are weighted by the fraction of rim remaining for each crater, compensating for the overcounting of large craters at the smallest values of f_{vis}.

craters. This correction also introduces logistical issues for human crater counters, for whom it is not trivial to measure the rim fraction of every crater counted, and who cannot be expected to identify craters down to such small remaining rim fractions.

5.4.3.3 Personal Visibility Criteria

Each of the curves in Figure 5.8 crosses its respective production function value of α at some intermediate value of f_{vis} between ~ 0.3 and 0.6, implying that these visibility criteria may more accurately reflect the underlying distribution of emplaced craters than others, without further correction. Human crater counters naturally recognize features according to individual and largely subconscious criteria, including (but not limited to) the rim fraction remaining for each crater. Further studies of crater identification methods and outcomes among crater counters, either on model-generated surfaces like those presented here or on actual lunar images like those used by *Robbins et al.* (2014) and CosmoQuest, may provide valuable insights into the fundamental variability of crater counts that can improve future efforts to quantify the Moon's impact history.

5.5 Discussion

The results presented here suggest that interpreting the distribution of craters counted on a planetary surface is not as straightforward as is often presented. Not only is there significant variability between crater counters in the identification of particular features (*Robbins et al.*, 2014), but a geometric bias exists that either under- or overcounts large craters, depending on the criterion used to define "visible" craters. This bias is not mitigated by choosing only the most pristine craters to include in size-frequency distributions. Rather, enforcing this strict criterion for visibility amounts to accepting a value of $f_{\text{vis}} = 1$, which actually exacerbates the problem. Using the rim-fraction weighting technique proposed by *Mullins* (1976) compensates for the overcounting of large craters at very low values of f_{vis}, but it assumes that crater counters can recognize features when almost all of their rims have disappeared and introduces the requirement that counters record remaining rim fractions for all features they log, further complicating a logistically-intensive and time-consuming process. A simple solution may be to develop a rule of thumb, where crater counters intentionally reject features with less than ~ 0.3 to 0.6 of their rims remaining, roughly corresponding to the range of values of f_{vis} where the α' curves cross their production function values, α, although this approach does not quantitatively resolve concerns about the comparability of crater counts made by different investigators.

Another possibility would be to investigate the nature of crater recognition itself among human crater counters. Cratered terrain models like the one presented here provide new opportunities to study synthetic terrains for which the exact crater distribution is known, thus allowing for direct quantification of the criteria used to identify features. Our preliminary investigations suggest that the comparison of craters identified on an artificially-illuminated model plane with the known underlying distribution of emplaced craters can provide an estimate of the range of f_{vis} implicitly assumed by each crater researcher. However, a comprehensive study is required to address details such as image resolution, minimum and maximum crater sizes, illumination angles, and correlation of emplaced craters with recognized features. The cratered terrain model's ability to track the 3-dimensional topography as well as surviving rim fragments also allows for the quantitative investigation of ejecta effects that can improve our understanding of how rim segments are erased over time.

There is another effect not yet taken into account by the rim-tracking model, which is related to the analysis presented in the previous chapter. The value of α determines the crater size most efficient at eroding features of any given scale (see Fig. 4.6). When α is less than 2 (for our 2-dimensional model), large craters dominate the erosion, and they erase all smaller craters simply by covering them. This is also the assumption of the rim-tracking feature: rim points are erased when they fall within $r_{\text{fac}}\frac{D}{2}$ of the center of a newly-emplaced crater. When $\alpha > 2$, however, diffusion (rather than covering) becomes the dominant form of erosion. Using Equation 4.14, the time it takes to diffuse a crater of size D, t_{diff}, can be estimated. For $\alpha > 4$, the smallest craters dominate diffusion of all other scales, and the diffusion time scales as D^2. Larger craters thus take longer to be erased, and are therefore detectable in the topography even after they have been covered once by smaller craters. Therefore, the 3-dimensional topography contains more information than the rim-tracking algorithm alone, and, because diffusion times are longer for larger craters, these features may be detectable and their diameters measured even without (or with few) pristine rim segments. As described in the previous chapter (Section 4.3), the equilibrium size-frequency distribution will follow $D^{2-\alpha}$. For α between 2 and 4, each crater size dominates its own diffusion, and the equilibrium size-frequency distribution is independent of α in this range, with a power law exponent of -2.

Erosion by diffusion rather than covering requires a redefinition of what it means for a rim point to be erased, and whether a geometric bias continues to exist in this case becomes a complicated question. All craters will be eroded by craters smaller than themselves (in most cases), and the asymmetry in degradation state between small and large craters observed in Section 5.4.2 is therefore is expected to be diminished. However, the extent to which crater counters can identify features without sharp rim crests as impact craters is a highly relevant question that remains largely unexamined. The two main processes of erosion—covering and diffusion—produce different expectations for the slope of the equilibrium size-frequency distribution for $\alpha > 2$. If rims only need to be covered to be erased, the observed size-frequency distribution will have the same power law slope as the production function (depending on the value chosen for f_{vis} and taking into account the geometric bias examined here). If rims need to be diffused to be erased, then the slope of the size-frequency distribution will be -2 regardless of the production function exponent (for $2 < \alpha \leq 4$). Lunar crater counts record a kink in the size-frequency distribution near $D = 100$ m, above which the power law exponent is -2 and below which it is steeper, suggesting that craters smaller than this size have reached equilibrium and those larger have not (*Soderblom*, 1970; *Richardson*, 2009). If this is the case, then the diffusive nature of erosion in this range of α is being detected by crater counters, and they must be identifying features with partially diffused rims. Studies of human crater counters using model-generated terrains may shed light on the complexity of criteria required to recognize degraded craters and measure their diameters.

The large dataset collected by the CosmoQuest Moon Mappers team and summarized by *Robbins et al.* (2014) provides another resource for the quantification of crater identification by many different crater counters. While this dataset lacks the model's ability to access the real underlying distribution of craters, it has the advantage of comparing crater counts on the same images among a large number of individuals, providing the opportunity to measure statistical variability among crater distributions. Some observations from *Robbins et al.* (2014) are already of interest to the geometric bias discussed above. For example, crater densities identified by investigators in a Narrow Angle Camera (NAC) image (M146959973L) on a portion of the maria clearly show the effects of crater degradation state on the ability to recognize features. Generally, there are more large degraded craters and more small pristine craters, in complete agreement with the analysis presented here. However, craters counted on highlands terrain in the Wide Angle Camera (WAC) image (M119455712M) show a quite different dependence on degradation state. Large craters that could be identified were more likely to be pristine than small craters, suggesting that large, degraded craters may be difficult to identify on rugged, reworked terrain. The study also mentions that investigators may be more attuned to features near the minimum and maximum crater sizes included in the image (which depend on the image resolution and domain size, respectively), causing them to identify relatively more features at the extremes than at intermediate sizes. This dataset thus represents a valuable means of examining the methods, assumptions, and biases inherent in the process of counting craters on the real lunar surface, and it provides a highly complimentary approach to counting craters on synthetic terrains where the underlying distribution is known.

5.6 Conclusions

What does f_{vis} represent in practice? For researchers counting craters on a planetary surface, there are inevitable limitations to what the eye can recognize as a crater in a field of overlapping craters, let alone on a surface with multiple geologic processes represented. The fraction of the rim remaining likely plays a role in these limitations, but there are many other factors to consider as well, from how spread out or connected the rim fragments are, to whether there is a size dependence involved. Perhaps counting craters on a topographic map results in a different f_{vis} than counting on an image, and certainly factors such as illumination angle and image resolution affect the visibility of partially obscured features. Some of these factors are already taken into account in crater counting—notably the falloff in small crater populations due to insufficient resolving power. However, the main result of this work—the extent to which we recognize craters may influence our measurements of crater size-frequency distributions—has so far remained largely unexplored. The computing power available to current cratered terrain models, together with the data collected by recent citizen science efforts to map the Moon, provides a new and unprecedented opportunity to address the effect of geometric bias on observed size-frequency distributions on the Moon and throughout the solar system.

Bibliography

Adams, A. L. (1874), I. on the dentition and osteology of the maltese fossil elephants, being a description of remains discovered by the author in malta, between the years 1860 and 1866., *The Transactions of the Zoological Society of London*, *9*(1), 1–124.

Aharonson, O., and N. Schorghofer (2006), Subsurface ice on Mars with rough topography, *J. Geophys. Res.*, *111*(E10), 11,007, doi:10.1029/2005JE002636.

Aharonson, O., M. T. Zuber, G. A. Neumann, and J. W. Head (1998), Mars: Northern hemisphere slopes and slope distributions, *Geophys. Res. Lett.*, *25*(24), 4413–4416.

Aharonson, O., M. T. Zuber, and D. H. Rothman (2001), Statistics of Mars' topography from the Mars Orbiter Laser Altimeter: Slopes, correlations, and physical models, *J. Geophys. Res.*, *106*, 23,723–23,736, doi:10.1029/2000JE001403.

Araki, H., S. Tazawa, H. Noda, Y. Ishihara, S. Goossens, S. Sasaki, N. Kawano, I. Kamiya, H. Otake, J. Oberst, et al. (2009), Lunar global shape and polar topography derived from Kaguya-LALT laser altimetry, *Science*, *323*(5916), 897–900.

Arnold, J. R. (1979), Ice in the lunar polar regions, *Journal of Geophysical Research: Solid Earth (1978–2012)*, *84*(B10), 5659–5668.

Baldwin, R. B. (1949), *The Face of the Moon*, University of Chicago Press, Chicago.

Baldwin, R. B. (1964), Lunar crater counts, *The Astronomical Journal*, *69*, 377.

Barker, M., E. Mazarico, G. Neumann, D. Smith, M. Zuber, et al. (2014), Merging digital elevation models from the lunar orbiter laser altimeter and kaguya terrain camera, in *Lunar and Planetary Institute Science Conference Abstracts*, vol. 45, p. 1635.

Bottke Jr, W. F., D. D. Durda, D. Nesvornỳ, R. Jedicke, A. Morbidelli, D. Vokrouhlickỳ, and H. F. Levison (2005), Linking the collisional history of the main asteroid belt to its dynamical excitation and depletion, *Icarus*, *179*(1), 63–94.

Brinkmann, R. T. (1966), Lunar crater distribution from the ranger 7 photographs, *Journal of Geophysical Research*, *71*(1), 340–342.

Butrica, A. J. (1996), *To See the Unseen: A History of Planetary Radar Astronomy*, National Aeronautics and Space Administration.

Campbell, D. B., B. A. Campbell, L. M. Carter, J.-L. Margot, and N. J. Stacy (2006), No evidence for thick deposits of ice at the lunar south pole, *Nature*, *443*(7113), 835–837.

Campbell, J. B. (2002), *Introduction to remote sensing*, CRC Press.

Chapman, C. R. (1968), Interpretation of the diameter-frequency relation for lunar craters photographed by rangers vii, viii, and ix, *Icarus*, *8*(1), 1–22.

Chapman, C. R., and W. B. McKinnon (1986), Cratering of planetary satellites, in *IAU Colloq. 77: Some Background about Satellites*, vol. 1, pp. 492–580.

Chapman, C. R., J. A. Mosher, and G. Simmons (1970), Lunar cratering and erosion from orbiter 5 photographs, *Journal of Geophysical Research*, *75*(8), 1445–1466.

Daniels, F. B. (1963), Radar Determination of the Root Mean Square Slope of the Lunar Surface, *J. Geophys. Res.*, *68*, 449–453, doi:10.1029/JZ068i002p00449.

Dietz, R. S. (1946), The meteoritic impact origin of the moon's surface features, *The Journal of Geology*, pp. 359–375.

Doel, R. E. (1996), *Solar System Astronomy in America, Communities, Patronage, and Interdisciplinary Science, 1920-1960*, Cambridge University Press.

Farr, T. G. (1992), Microtopographic evolution of lava flows at Cima volcanic field, Mojave Desert, California, *J. Geophys. Res.*, *97*(B11), 15,171–15,179.

Fauth, P. (1909), *The Moon in Modern Astronomy: Summary of Twenty Years Selenographic Work, and a Study of Recent Problems*, D. van Nostrand Company.

Galilei, G. (1989), *Sidereus Nuncius, or The Sidereal Messenger*, University of Chicago Press.

Garrick-Bethell, I., and M. T. Zuber (2009), Elliptical structure of the lunar South Pole-Aitken basin, *Icarus*, *204*, 399–408, doi:10.1016/j.icarus.2009.05.032.

Garvin, J., J. Bufton, J. Blair, D. Harding, S. Luthcke, J. Frawley, and D. Rowlands (1998), Observations of the earth's topography from the shuttle laser altimeter (sla): laser-pulse echo-recovery measurements of terrestrial surfaces, *Physics and Chemistry of the Earth*, *23*(9), 1053–1068.

Garvin, J. B., and J. J. Frawley (1998), Geometric properties of martian impact craters: Preliminary results from the mars orbiter laser altimeter, *Geophysical Research Letters*, *25*(24), 4405–4408.

Gault, D. E. (1970), Saturation and equilibrium conditions for impact cratering on the lunar surface: Criteria and implications, *Radio Science*, *5*(2), 273–291.

Gifford, A. C. (1924), *The mountains of the Moon*, Hector Observatory.

Gilbert, G. K. (1893), *The Moon's face: A study of the origin of its features*, Philosophical Society of Washington.

Hartmann, W. K. (1970), Lunar cratering chronology, *Icarus*, *13*(2), 299–301.

Hartmann, W. K. (1984), Does crater saturation equilibrium occur in the solar system?, *Icarus*, *60*(1), 56–74.

Hartmann, W. K. (1985), Impact experiments: 1. ejecta velocity distributions and related results from regolith targets, *Icarus*, *63*(1), 69–98.

Hartmann, W. K., and R. W. Gaskell (1997), Planetary cratering 2: Studies of saturation equilibrium, *Meteoritics & Planetary Science*, *32*(1), 109–121.

Heiken, G., D. Vaniman, and B. M. French (1991), *Lunar sourcebook: A user's guide to the Moon*, CUP Archive.

Hiesinger, H., J. W. Head, U. Wolf, R. Jaumann, and G. Neukum (2010), Ages and stratigraphy of lunar mare basalts in Mare Frigoris and other nearside maria based on crater size-frequency distribution measurements, *Journal of Geophysical Research (Planets)*, *115*(E14), 3003, doi:10.1029/2009JE003380.

Hiesinger, H., R. Jaumann, G. Neukum, and J. W. Head (2012), Ages of mare basalts on the lunar nearside, *Journal of Geophysical Research: Planets (1991–2012)*, *105*(E12), 29,239–29,275.

Howard, A. D. (2007), Simulating the development of martian highland landscapes through the interaction of impact cratering, fluvial erosion, and variable hydrologic forcing, *Geomorphology*, *91*(3), 332–363.

Hoyt, W. G. (1987), *Coon Mountain controversies: Meteor Crater and the development of impact theory*, University of Arizona Press.

Ivanov, B., G. Neukum, W. Bottke, and W. Hartmann (2002), The comparison of size-frequency distributions of impact craters and asteroids and the planetary cratering rate, *Asteroids III*, *1*, 89–101.

Ives, H. E. (1919), Some large-scale experiments imitating the craters of the moon, *The Astrophysical Journal*, *50*, 245.

Jaffe, L. D. (1967), Lunar Surface Exploration by Surveyor Spacecraft: Introduction, *J. Geophys. Res.*, *72*, 773, doi:10.1029/JZ072i002p00773.

Kaula, W., G. Schubert, R. Lingenfelter, W. Sjogren, and W. Wollenhaupt (1974), Apollo laser altimetry and inferences as to lunar structure, in *Lunar and Planetary Science Conference Proceedings*, vol. 5, pp. 3049–3058.

Kreslavsky, M. A., and J. W. Head (2000), Kilometer-scale roughness of Mars: Results from MOLA data analysis, *J. Geophys. Res.*, *105*, 26,695–26,712, doi:10.1029/2000JE001259.

Kreslavsky, M. A., J. W. Head, G. A. Neumann, M. A. Rosenburg, O. Aharonson, D. E. Smith, and M. T. Zuber (2013), Lunar topographic roughness maps from Lunar Orbiter Laser Altimeter (LOLA) data: Scale dependence and correlation with geologic features and units, *Icarus*, *226*(1), 52–66.

Li, C., X. Ren, J. Liu, X. Zou, L. Mu, J. Wang, R. Shu, Y. Zou, H. Zhang, C. Lü, et al. (2010), Laser altimetry data of change-1 and the global lunar dem model, *Science China Earth Sciences*, *53*(11), 1582–1593.

Lindberg, D. C. (1992), *The beginnings of western science: The European scientific tradition in philosophical, religious, and institutional context, 600 BC to AD 1450*, University of Chicago Press Chicago.

Lucchitta, B. K., and A. Center (1978), *Geologic map of the north side of the Moon*, US Geological Survey Reston.

MacDonald, T. (1931), The number and area of lunar objects, *Journal of the British Astronomical Association*, *41*, 288–290.

Main, I. G., T. Leonard, O. Papasouliotis, C. G. Hatton, and P. G. Meredith (1999), One slope or two? Detecting statistically significant breaks of slope in geophysical data, with application to fracture scaling relationships, *Geophys. Res. Lett.*, *26*, 2801–2804, doi:10.1029/1999GL005372.

Marcus, A. (1964), A stochastic model of the formation and survival of lunar craters: I. distribution of diameter of clean craters, *Icarus*, *3*(5), 460–472.

Marcus, A. (1966a), A stochastic model of the formation and survival of lunar craters: Iv. on the nonrandomness of crater centers, *Icarus*, *5*(1), 190–200.

Marcus, A. H. (1966b), A stochastic model of the formation and survival of lunar craters: Iii. filling and disappearance of craters, *Icarus*, *5*(1), 178–189.

Marcus, A. H. (1966c), A stochastic model of the formation and survival of lunar craters: Ii. approximate distribution of diameter of all observable craters, *Icarus*, *5*(1), 165–177.

Marcus, A. H. (1966d), A stochastic model of the formation and survival of lunar craters: V. approximate diameter distribution of primary and secondary craters, *Icarus*, *5*(1), 590–605.

Marcus, A. H. (1967), Further interpretations of crater depth statistics and lunar history, *Icarus*, *7*(1), 407–409.

McEwen, A. S., and M. S. Robinson (1997), Mapping of the moon by Clementine, *Advances in Space Research*, *19*, 1523–+, doi:10.1016/S0273-1177(97)00365-7.

Melosh, H. J. (1989), Impact cratering: A geologic process, *Research supported by NASA. New York, Oxford University Press (Oxford Monographs on Geology and Geophysics, No. 11)*, *1*.

Mest, S. C. (2011), The geology of schrödinger basin: Insights from post-lunar orbiter data, *Recent Advances and Current Research Issues in Lunar Stratigraphy*, *477*, 95.

Moore, H. J., and G. L. Tyler (1973), Comparison Between Photogrammetric and Bistatic-Radar Slope-Frequency Distributions, in *Apollo 17: Preliminary Science Report*, *NASA Special Publication*, vol. 330, pp. 33–17.

Morris, A. R., F. S. Anderson, P. J. Mouginis-Mark, A. F. C. Haldemann, B. A. Brooks, and J. Foster (2008), Roughness of Hawaiian volcanic terrains, *Journal of Geophysical Research (Planets)*, *113*(E12), 12,007–27,012, doi:10.1029/2008JE003079.

Mullins, W. (1976), An estimator of the underlying size distribution of overlapping impact-craters, *Icarus*, *29*(1), 113–123.

Mullins, W. (1978), Use of equivalency in estimating the historical size distribution of impact craters, *Icarus*, *33*(3), 624–629.

Namiki, N., and C. Honda (2003), Testing hypotheses for the origin of steep slope of lunar size-frequency distribution for small craters, *Earth Planets and Space*, *55*(1), 39–52.

Nasmyth, J., and J. Carpenter (1874), *The moon: Considered as a planet, a world, and a satellite*, J. Murray (London).

Neukum, G., and B. Ivanov (1994), Crater size distributions and impact probabilities on earth from lunar, terrestrial-planet, and asteroid cratering data, *Hazards due to Comets and Asteroids*, *1*, 359.

Neukum, G., B. König, and J. Arkani-Hamed (1975), A study of lunar impact crater size-distributions, *The Moon*, *12*(2), 201–229.

Neukum, G., B. A. Ivanov, and W. K. Hartmann (2001), Cratering records in the inner solar system in relation to the lunar reference system, *Space Science Reviews*, *96*(1-4), 55–86.

Neumann, G. A. (2001), Some aspects of processing extraterrestrial lidar data: Clementine, near, mola, *International Archives of Photogrammetry and Remote Sensing*, *34*(3), W4.

Neumann, G. A., and D. W. Forsyth (1995), High resolution statistical estimation of seafloor morphology: Oblique and orthogonal fabric on the flanks of the Mid-Atlantic Ridge, 34° 35.5° S, *Marine Geophysical Researches*, *17*, 221–250, doi:10.1007/BF01203464.

Nimmo, F., B. Bills, and P. Thomas (2011), Geophysical implications of the long-wavelength topography of the saturnian satellites, *Journal of Geophysical Research: Planets (1991–2012)*, *116*(E11).

Nozette, S., C. Lichtenberg, P. Spudis, R. Bonner, W. Ort, E. Malaret, M. Robinson, and E. Shoemaker (1996), The clementine bistatic radar experiment, *Science*, *274*(5292), 1495–1498.

Nozette, S., P. D. Spudis, M. S. Robinson, D. Bussey, C. Lichtenberg, and R. Bonner (2001), Integration of lunar polar remote-sensing data sets: Evidence for ice at the lunar south pole, *Journal of Geophysical Research: Planets (1991–2012)*, *106*(E10), 23,253–23,266.

Oberbeck, V. R. (1975), The role of ballistic erosion and sedimentation in lunar stratigraphy, *Reviews of Geophysics and Space Physics*, *13*, 337–362.

Öpik, E. J. (1960), The lunar surface as an impact counter, *Monthly Notices of the Royal Astronomical Society*, *120*, 404.

Orosei, R., R. Bianchi, A. Coradini, S. Espinasse, C. Federico, A. Ferriccioni, and A. I. Gavrishin (2003), Self-affine behavior of Martian topography at kilometer scale from Mars Orbiter Laser Altimeter data, *Journal of Geophysical Research (Planets)*, *108*, 8023, doi:10.1029/2002JE001883.

Ostro, S. J. (1993), Planetary radar astronomy, *Reviews of Modern Physics*, *65*(4), 1235.

Passey, Q. R., and E. M. Shoemaker (1982), Craters and basins on ganymede and callisto-morphological indicators of crustal evolution, in *Satellites of Jupiter*, vol. 1, pp. 379–434.

Pieters, C. M., J. B. Adams, M. O. Smith, P. J. Mouginis-Mark, and S. H. Zisk (1985), The nature of crater rays - The Copernicus example, *J. Geophys. Res.*, *90*, 12,393, doi:10.1029/JB090iB14p12393.

Pike, R. (1977), Apparent depth/apparent diameter relation for lunar craters, in *Lunar and Planetary Science Conference Proceedings*, vol. 8, pp. 3427–3436.

Pike, R. J. (1974), Depth/diameter relations of fresh lunar craters: Revision from spacecraft data, *Geophysical Research Letters*, *1*(7), 291–294.

Pike, R. J. (1988), Geomorphology of impact craters on mercury, *Mercury, University of Arizona Press*, *1*, 165–273.

Ping, J., Q. Huang, J. Yan, J. Cao, G. Tang, and R. Shu (2009), Lunar topographic model CLTM-s01 from Chang'E-1 laser altimeter, *Science in China: Physics, Mechanics and Astronomy*, *52*, 1105–1114, doi:10.1007/s11433-009-0144-8.

Richardson, J. E. (2009), Cratering saturation and equilibrium: A new model looks at an old problem, *Icarus*, *204*(2), 697–715.

Richardson, J. E., H. J. Melosh, N. A. Artemeiva, and E. Pierazzo (2005), Impact cratering theory and modeling for the deep impact mission: From mission planning to data analysis, in *Deep Impact Mission: Looking Beneath the Surface of a Cometary Nucleus*, pp. 241–267, Springer.

Robbins, S. J., I. Antonenko, M. R. Kirchoff, C. R. Chapman, C. I. Fassett, R. R. Herrick, K. Singer, M. Zanetti, C. Lehan, D. Huang, et al. (2014), The variability of crater identification among expert and community crater analysts, *Icarus*, *234*, 109–131.

Rosenburg, M., O. Aharonson, J. Head, M. Kreslavsky, E. Mazarico, G. Neumann, D. Smith, M. Torrence, and M. Zuber (2011), Global surface slopes and roughness of the moon from the lunar orbiter laser altimeter, *Journal of Geophysical Research: Planets (1991–2012)*, *116*(E2).

Schroeder, M., and K. Wiesenfeld (1991), Fractals, Chaos, Power Laws: Minutes from an Infinite Paradise, *Physics Today*, *44*, 91, doi:10.1063/1.2810323.

Scott, D. H., and J. F. McCauley (1977), *Geologic map of the west side of the Moon*, US Geological Survey Reston.

Shaler, N. S., and W. M. Davis (1881), *Illustrations of the Earth's Surface: Glaciers*, JR Osgood & Company.

Sharpton, V. L., and J. W. Head (1985), Analysis of regional slope characteristics on Venus and earth, *J. Geophys. Res.*, *90*, 3733–3740, doi:10.1029/JB090iB05p03733.

Shepard, M. K., B. A. Campbell, M. H. Bulmer, T. G. Farr, L. R. Gaddis, and J. J. Plaut (2001), The roughness of natural terrain: A planetary and remote sensing perspective, *J. Geophys. Res.*, *106*, 32,777–32,796, doi:10.1029/2000JE001429.

Shoemaker, E., M. Hait, G. Swann, D. Schleicher, D. Dahlem, G. Schaber, and R. Sutton (1970), Lunar regolith at tranquillity base, *Science*, *167*(3918), 452–455.

Shoemaker, E. M. (1963), Impact mechanics at meteor crater, arizona, *The Moon Meteorites and Comets*, *1*, 301.

Shoemaker, E. M. (1977), Penetration mechanics of high velocity meteorites, illustrated by Meteor Crater, Arizona, *Meteorite Craters, Benchmark Papers in Geology*, *1*, 170.

Shoemaker, E. M., and R. J. Hackman (1962), Stratigraphic basis for a lunar time scale, in *The Moon*, vol. 14, pp. 289–300.

Shoemaker, E. M., R. J. Hackman, and R. E. Eggleton (1961), *Interplanetary correlation of geologic time*, US Department of the Interior, Geological Survey.

Simpson, R. A., and G. L. Tyler (1999), Reanalysis of clementine bistatic radar data from the lunar south pole, *Journal of Geophysical Research: Planets (1991–2012)*, *104*(E2), 3845–3862.

Smith, D. E., M. T. Zuber, G. A. Neumann, and F. G. Lemoine (1997), Topography of the moon from the clementine lidar, *J. Geophys. Res.*, *102*(E1), 1591–1611.

Smith, D. E., M. T. Zuber, H. V. Frey, J. B. Garvin, J. W. Head, D. O. Muhleman, G. H. Pettengill, R. J. Phillips, S. C. Solomon, H. J. Zwally, W. B. Banerdt, T. C. Duxbury, M. P. Golombek, F. G. Lemoine, G. A. Neumann, D. D. Rowlands, O. Aharonson, P. G. Ford, A. B. Ivanov, C. L. Johnson, P. J. McGovern, J. B. Abshire, R. S. Afzal, and X. Sun (2001), Mars Orbiter Laser Altimeter: Experiment summary after the first year of global mapping of Mars, *J. Geophys. Res.*, *106*, 23,689–23,722, doi:10.1029/2000JE001364.

Smith, D. E., M. T. Zuber, G. B. Jackson, J. F. Cavanaugh, G. A. Neumann, H. Riris, X. Sun, R. S. Zellar, C. Coltharp, J. Connelly, R. B. Katz, I. Kleyner, P. Liiva, A. Matuszeski, E. M. Mazarico, J. F. McGarry, A. Novo-Gradac, M. N. Ott, C. Peters, L. A. Ramos-Izquierdo, L. Ramsey, D. D. Rowlands, S. Schmidt, V. S. Scott, G. B. Shaw, J. C. Smith, J. Swinski, M. H. Torrence, G. Unger, A. W. Yu, and T. W. Zagwodzki (2010a), The Lunar Orbiter Laser Altimeter Investigation on the Lunar Reconnaissance Orbiter Mission, *Space Science Reviews*, *150*, 209–241, doi:10.1007/s11214-009-9512-y.

Smith, D. E., M. T. Zuber, G. A. Neumann, F. G. Lemoine, E. Mazarico, M. H. Torrence, J. F. McGarry, D. D. Rowlands, J. W. Head, T. H. Duxbury, O. Aharonson, P. G. Lucey, M. S. Robinson, O. S. Barnouin, J. F. Cavanaugh, X. Sun, P. Liiva, D.-d. Mao, J. C. Smith, and A. E. Bartels (2010b), Initial observations from the Lunar Orbiter Laser Altimeter (LOLA), *Geophys. Res. Lett.*, *37*, L18204, doi:10.1029/2010GL043751.

Smith, D. E., M. T. Zuber, R. J. Phillips, S. C. Solomon, S. A. Hauck, F. G. Lemoine, E. Mazarico,

G. A. Neumann, S. J. Peale, J.-L. Margot, et al. (2012), Gravity field and internal structure of mercury from messenger, *Science*, *336*(6078), 214–217.

Smith, D. K., and T. H. Jordan (1988), Seamount statistics in the Pacific Ocean, *J. Geophys. Res.*, *93*, 2899–2918, doi:10.1029/JB093iB04p02899.

Soderblom, L. A. (1970), A model for small-impact erosion applied to the lunar surface, *Journal of Geophysical Research*, *75*(14), 2655–2661.

Solomon, S. C., and J. W. Head (1980), Lunar mascon basins - Lava filling, tectonics, and evolution of the lithosphere, *Reviews of Geophysics and Space Physics*, *18*, 107–141.

Stacy, N., D. Campbell, and P. Ford (1997), Arecibo radar mapping of the lunar poles: A search for ice deposits, *Science*, *276*(5318), 1527–1530.

Stöffler, D., and G. Ryder (2001), Stratigraphy and isotope ages of lunar geologic units: Chronological standard for the inner solar system, in *Chronology and evolution of Mars*, pp. 9–54, Springer.

Strom, R. G. (1977), Origin and relative age of lunar and mercurian intercrater plains, *Physics of the Earth and Planetary Interiors*, *15*(2), 156–172.

Stuart-Alexander, D. E., and A. Center (1978), *Geologic map of the central far side of the Moon*, US Geological Survey Reston.

Talpe, M. J. (2012), Characterization of crater morphometry on the moon and mercury from altimetry observations, Ph.D. thesis, Massachusetts Institute of Technology.

Turcotte, D. L. (1997), *Fractals and chaos in geology and geophysics*, Cambridge University Press.

van der Bogert, C. H., H. Hiesinger, A. S. McEwen, C. Dundas, V. Bray, M. S. Robinson, J. B. Plescia, D. Reiss, K. Klemm, and Lroc Team (2010), Discrepancies Between Crater Size-Frequency Distributions on Ejecta and Impact Melt Pools at Lunar Craters: An Effect of Differing Target Properties?, in *Lunar and Planetary Science Conference*, *Lunar and Planetary Science Conference*, vol. 41, p. 2165.

Watson, K., B. C. Murray, and H. Brown (1961), The behavior of volatiles on the lunar surface, *Journal of Geophysical Research*, *66*(9), 3033–3045.

Wegener, A., and A. C. Şengör (1975), The origin of lunar craters, *The Moon*, *14*(2), 211–236.

Whitaker, E. A. (2003), *Mapping and naming the moon: a history of lunar cartography and nomenclature*, Cambridge University Press.

Wilhelms, D. E. (1993), *To a Rocky Moon: A geologist's history of lunar exploration*, University of Arizona Press.

Wilhelms, D. E., J. F. McCauley, and A. Chart (1971), *Geologic map of the near side of the Moon*, US Geological Survey Reston.

Wilhelms, D. E., F. El-Baz, F. El-Baz, E. Geologist, F. El-Baz, and E. Géologue (1977), *Geologic map of the east side of the Moon*, US Geological Survey Reston.

Wilhelms, D. E., K. A. Howard, H. G. Wilshire, and A. Center (1979), *Geologic map of the south side of the Moon*, Department of the Interior, US Geological Survey.

Wilhelms, D. E., J. F. McCauley, and N. J. Trask (1987), *The geologic history of the Moon*, US Government Printing Office Washington DC.

Woronow, A. (1978), A general cratering-history model and its implications for the lunar highlands, *Icarus*, *34*(1), 76–88.

Woronow, A. (1985a), A monte carlo study of parameters affecting computer simulations of crater saturation density, *Journal of Geophysical Research: Solid Earth (1978–2012)*, *90*(S02), C817–C824.

Woronow, A. (1985b), Recovering crater production functions from densely cratered surfaces, *Journal of Geophysical Research: Solid Earth (1978–2012)*, *90*(S02), C825–C827.

Yokota, Y., J. Haruyama, M. Ohtake, T. Matsunaga, C. Honda, T. Morota, M. Abe, M. Torii, Y. Ogawa, H. Demura, N. Hirata, and Lism Working Group (2008), Mapping of Lunar Topographic Roughness by Digital Terrain Model, in *Lunar and Planetary Institute Science Conference Abstracts*, *Lunar and Planetary Institute Science Conference Abstracts*, vol. 39, p. 1921.

Young, J. (1940), A statistical investigation of diameter and distribution of lunar craters, *J. Brit. Astron. Assoc*, *50*(9), 309–326.

Zahnle, K., P. Schenk, H. Levison, and L. Dones (2003), Cratering rates in the outer solar system, *Icarus*, *163*(2), 263–289.

Zuber, M. T., D. E. Smith, F. G. Lemoine, and G. A. Neumann (1994), The shape and internal structure of the moon from the clementine mission, *Science*, *266*(5192), 1839–1843.

Zuber, M. T., D. E. Smith, A. F. Cheng, J. B. Garvin, O. Aharonson, T. D. Cole, P. J. Dunn, Y. Guo, F. G. Lemoine, G. A. Neumann, et al. (2000), The shape of 433 eros from the near-shoemaker laser rangefinder, *Science*, *289*(5487), 2097–2101.

Zuber, M. T., D. E. Smith, R. S. Zellar, G. A. Neumann, X. Sun, R. B. Katz, I. Kleyner, A. Matuszeski, J. F. McGarry, M. N. Ott, L. A. Ramos-Izquierdo, D. D. Rowlands, M. H. Torrence, and T. W. Zagwodzki (2010), The Lunar Reconnaissance Orbiter Laser Ranging Investigation, *Space Science Reviews*, *150*, 63–80, doi:10.1007/s11214-009-9511-z.

Zuber, M. T., J. W. Head, D. E. Smith, G. A. Neumann, E. Mazarico, M. H. Torrence, O. Aharonson, A. R. Tye, C. I. Fassett, M. A. Rosenburg, et al. (2012a), Constraints on the volatile distribution within shackleton crater at the lunar south pole, *Nature*, *486*(7403), 378–381.

Zuber, M. T., D. E. Smith, R. J. Phillips, S. C. Solomon, G. A. Neumann, S. A. Hauck, S. J. Peale, O. S. Barnouin, J. W. Head, C. L. Johnson, et al. (2012b), Topography of the northern hemisphere of mercury from messenger laser altimetry, *Science*, *336*(6078), 217–220.